DEFORMATION OF FLUID-SATURATED POROUS ROCK

A DISSERTATION
SUBMITTED TO THE FACULTY OF
UNIVERSITY OF MINNESOTA
BY

ROMAN YURYEVICH MAKHNENKO

IN PARTIAL FULFILLMENT OF THE REQUIREMENTS
FOR THE DEGREE OF
DOCTOR OF PHILOSOPHY

Advisor: **Joseph F. Labuz**

AUGUST 2013

Acknowledgements

Any PhD thesis is the result of efforts of not only the person who is entitled as the author, but a number of other people. I would like to acknowledge them.

For the formal part, the financial support for my research was provided by DOE Grant DE-FE0002020 funded through the American Recovery and Reinvestment Act. Itasca Consulting and University of Minnesota also contributed to my survival in the USA.

Professor Joseph Labuz was very kind to take a poor Russian guy as his PhD student, support and mentor him for four years. I appreciate the amount of time and energy he spent explaining things, proving that I was wrong or fixing my writing. Our loud conversations happening everywhere from the middle of the CE front office to the plane flying above the Atlantics will be long remembered not only by me, but people who could hear them even from different floors and buildings. Kim Labuz is acknowledged for letting her husband spending a lot of time in the office and being always nice and hospitable to me.

Prof. Emmanuel Detournay was my Master advisor and kept educating and schooling me during my PhD years. I hope that it have helped me to become a better student and person. Prof. Andrew Drescher was my committee chair, delivered a nice class and was always ready to discuss my research. I will do my best to inherit the critical way of thinking from him. Professors Hudleston and Saar from Earth Sciences department served as my committee members and provided nice feedback about my research.

Dr. Andrew Bunger inspired me in doing rock testing and is a good “role model” for me in terms of his work discipline. Professors Guzina, Stolarski, Barnes, Arndt, and Tadmor taught classes which nurtured my interest in civil engineering.

Prof. Sonya Mogilevskaya invited me to MN and Lisa Gordeli helped a lot with all my questions and stuff. Her husband Ivan became my best “American” friend, tea drinking, hiking and hockey buddy of mine.

I was very lucky to work in the Rock Mechanics lab and be surrounded by people affiliated with it. Jim Meyer can consider this thesis as his own, because his impact on the experimental part of my work cannot be overestimated. Starting working in the lab as the undergrad, we were in need to leave him for another one and a half year, such that he could help me, even though he thought that he was pursuing his Master studies. Chu-Shu Kao was always willing to explain the unknown things, sometimes even spending too much time helping others. Being my roommate for more than three years and never showing that he is stressed or overwhelmed, Qing Lin had inspired me on starting my

Rock lab career. Lately in the program, Justice Harvieux became my lab assistant. He also drew most of the nice figures in this thesis. Chunwei Ge proceeded AE data, Jon Manning interpreted DIC results, and Derrick Blanksma finally made our water pump working properly. Ali Tarokh was keeping me a company during my last PhD year. Paul Bergson and Gil Hue were (almost) always around to assist with the experimental equipment. Steve Wilk never really helped with experiments but was a big part of the scientific atmosphere in the lab, as well as Megan Nutzmann, who additionally have scanned a lot of old papers cited in this thesis.

Civil Engineering graduate students, who also greatly contributed to the atmosphere, even though often our conversations were happening at the Sally's are Jim and Rachel Hableton, Alex D., Huina, Bulent, Roberto, Luc and Cata, Egor and Zhenya, Eyoab, Roma, Dima, Igor, Jeff, Paolo, Davide, Alina, Alex H. and Jullien, Katie, Cedric, Simon, and Antoine.

Special thanks goes to former soccer (and now social) club Voyageurs. Peter, Raul, Pietro, Kamran, Professors Fernando Porte-Agel and Nikolaos Geroliminis, Sasha, Karen, Christian, Patrick, and Brian were a part of the big events happening on UMN soccer fields. People of Dynamo Eden Prairie also had cheered me up from time to time.

University of Minnesota is thanked for building the Rec Center right cross–the-road from the CE building, for the hockey Gophers, and the opportunity to attend from time to time Ukrainian culture events at the Northtrop. Minnesota Wild brought me some good emotions during 2007/2008 season and Minnesota Vikings made me happy in 2009.

All this years I felt strong support from my home country. My father dedicated too much of his time and emotions thinking about my little problems. His moral support at some critical moments was crucial for my survival as a conscious person. He is also specially thanked for crossing the ocean to be with me on the D-day. My mother, brother, grandma and Ukrainian relatives were and are happy about all my achievements. My best friends Kuznetsva, Der, and Sedoy did not want me leaving them for America and were always glad to see me and discuss everything.

The Bulat family is thanked for the warm welcome and the feelings of home in American Midwest, and mostly for their second daughter. Maria, I was very lucky to meet you at the beginning of my PhD studies. Your dedication to my life is priceless: leaving your job, the country, which became native to you, and your big family for our small one means everything to me. Thank you for all warmth, late night dinners, relaxing weekends and trips, ability to listen my whining, and for the best thing happened to us – Sofia Miele.

Dedication

In memory of my great grandparents, grandfathers, and my brother who are always watching me from the above.

Abstract

In-situ rock is often fully saturated or at least has a high fluid content. The presence of pore fluid can affect both the elastic response and the inelastic deformation process. However, testing of fluid-saturated rock is not typically performed, even though rock-fluid interaction is critical in many applications, such as oil and natural gas exploration and recovery procedures.

Experimental techniques aimed at the measurements of the parameters that govern the deformation of fluid-filled porous rock were developed. Berea sandstone was tested under the limiting conditions of drained, undrained, and unjacketed response. Saturation methods were applied to the rock at pore pressures of 3 – 4 MPa. Hydrostatic loading and compression experiments, both conventional triaxial and plane strain loading, were performed on the sandstone to investigate isotropic and transversely isotropic poroelastic behavior. Measured parameters were used to calibrate a constitutive model that predicts undrained inelastic deformation from the drained response. The experimental data shows good agreement with the model: the effect of dilatant hardening in undrained triaxial and plane strain compression tests under constant mean stress was predicted and observed.

Suggested experimental methods can be, and have been already, implemented for testing rock from the field. Moreover, the developed techniques are applicable for the prediction of deformation and induced seismicity in fluid-filled rock utilized for CO_2 sequestration.

Table of Contents

List of Tables

List of Figures

Chapter 1

Introduction

1.1 Motivation

The presence of pore fluid plays an important role in a wide variety of geoengineering and geophysics problems. These include earthquake precursory processes (Rice and Rudnicki 1979; Roeloffs 1996), hydraulic fracturing (Haimson and Fairhurst 1969; Rice and Cleary 1976; Detournay and Cheng 1993), water level changes in wells and tide effects on compressible aquifers (van der Kamp and Gale 1983; Wang 2000), to name a few. Oil and gas exploration relies on knowledge of the compresibilities and related seismic velocities of rock to differentiate between pore fluids (Han and Batzle 2004). Also, understanding the chemo-thermomechanical interactions between the gas, the groundwater, and the bedrock is critical to evaluate the safety of potential CO_2 storage sites.

Two limiting time scales are usually considered for the deformation of fluid-filled materials. If the time scale of deformation is rapid in comparison to that for diffusion so that the fluid mass in a material element remains constant, then the response is termed "undrained." The long-time or "drained" response is the one for which the local pore fluid pressure is constant. An elastic fluid-saturated solid responds more stiffly to deformations that are rapid compared to the time scale of diffusion, than for deformations that are slow compared to the diffusion time (Brace and Martin 1968; Rice 1975).

The inelastic deformation of geological materials is typically inhibited by an increase of mean stress (compression positive). Thus, an increase in pore fluid pressure decreases the "effective" mean stress and promotes inelastic deformation; conversely, a decrease in pore fluid pressure tends to inhibit inelastic deformation (Rice 1975). Coupling of deformation with pore fluid diffusion also introduces time dependence into the response of an otherwise rate-independent solid.

Depending on the stress state, the constitutive response of rock typically involves dilation (volume increase) as deformation becomes inelastic. When the rock is fluid-saturated and the time scale does not allow drainage, suction is induced in the pore fluid, and by the effective stress principle, the rock is dilatantly hardened over the resistance that it would exhibit to a corresponding increment of drained deformation (Rice 1975). The phenomenon was first noticed for granular materials by Reynolds (1886), and it has been studied by Frank (1965) in relation to seismic sources in the fluid-saturated Earth's crust. However, some experimental work (Aldrich 1969) does not support this observation.

The characterization of inelastically deforming rock under well-controlled drainage conditions is required in order to understand the coupling between rock deformation and pore fluid diffusion just before failure, and for the interpretation of premonitory events in the Earth's crust prior to faulting (Nur 1972; Scholz *et al.* 1973; Rice and Cleary 1976). For example, the problem of stress concentration near a passing rupture front along the fault in a fluid-saturated rock is assumed to be effectively undrained on a short timescale. Then, if the material is plastically dilating, the undrained deformation was found to be notably more resistant to shear localization than predicted by neglect of pore pressure changes (Viesca *et al.* 2008). These considerations are particularly important when analyzing the stability of long-term underground storage facilities, such as the permanent disposal of CO_2 or nuclear waste.

Laboratory measurements that provide estimates of poroelastic parameters and consider the rate dependent effects of coupling of deformation with pore fluid diffusion are needed to describe the aforementioned effects.

1.2 Aim and Scope

The aim of this study is to experimentally investigate poroelastic and inelastic deformation of a porous, fluid-saturated rock under different limiting regimes. The emphasis is placed on accurate stress and displacement measurements to provide the precise calculation of the parameters that govern material's response. The following are the specific objectives:

- Modify the University of Minnesota plane-strain apparatus in order to conduct plane strain and conventional triaxial compression tests with water-saturated rock specimens and to measure the pore pressure within the rock.
- Calibrate all transducers within the apparatus at the various loading states and determine the compliances of the system.
- Develop a technique for specimen saturation.
- Conduct hydrostatic, plane strain, and triaxial compression tests under air-dry, drained, undrained, and unjacketed conditions.
- Evaluate the poroelastic behavior of the rock.
- Measure parameters associated with the constitutive model to describe the inelastic deformation of fluid-saturated rock; compare the model and experimentally observed responses.

1.3 Organization

This thesis is divided into five chapters. Theoretical background is given in Chapter 2. Experimental techniques are described in Chapter 3. The results of testing dry and fluid-saturated rock under different limiting regimes are reported and discussed in Chapter 4. Final remarks and future works are presented in Chapter 5. Calibration of the plane strain apparatus and acoustic emission data are included in the Appendices.

Chapter 2

Theoretical background

2.1 Theory of porous media

The modern theory of porous media is based on the important principles of mechanics that were developed in XVIII and XIX centuries. During the XVIII century, the theory of ideal fluids was founded and the concept of volume fractions was first stated. In the XIX century, linear elasticity was derived, fundamental laws of continuum mechanics and thermodynamics were discovered, Darcy's law for the flow through porous bodies was published, plasticity concepts were first discussed, and mixture theory was developed. The first half of the XX century saw the beginning of the modern era, when attempts to clarify the mechanical interaction of liquids, gases, and rigid porous solids were achieved and deformable saturated porous solids were first considered (de Boer 2000).

Terzaghi in 1923 proposed a model of one-dimensional consolidation that accounted for the influence of pore fluid pressure on the soil deformation and was based on a variety of experimental data. Later, Terzaghi (1936) introduced the concept of the "effective" stress: the effect of the pore fluid on some aspect of the mechanical behavior can be incorporated by replacing the normal stress by the effective normal stress, the difference between the normal stress and pore fluid pressure. Discussions of the concept were already made by Reynolds (1883) and Boussinesq (1885), and it was experimentally investigated by Fillunger (1915). However, Terzaghi is recognized for introducing the concept to the engineering world (Skempton 1960). His empirical expression turns out to be a very good description for soil, and nearly correct for highly porous and cracked rock, but it is not true as a general rule for all porous media.

Biot (1935, 1941) followed the scientific work of Terzaghi and developed the first rational theory for the mechanical behavior of porous materials. Biot considered soil, which was assumed to be isotropic, linearly elastic, and having incompressible water flowing through its porous skeleton. He developed the general equations for the

prediction of settlements and stresses for three-dimensional problems by extending the theory of elasticity for a two-phase system through the introduction of an additional quantity: a new strain variable called the variation in water content, which was coupled with the increment of water pressure. Under the assumption of small strains, linear relationships between the strains and increment of fluid content to stresses and pore pressure were written and four poroelastic moduli (rather than two standard elasticity moduli) were introduced.

Gassmann (1951, 2007), assuming macroscopic homogeneity and isotropy, derived a relation between the elastic properties of a porous medium with fluid-filled interconnected pores and the elastic properties of the same medium with empty pores. His equation became the important tool in the petroleum industry in the interpretation of seismic data on sedimentary materials, and differentiation between the pore fluids they contain.

Biot and Willis (1957), being aware of the results of Gassmann, reviewed Biot's (1941) work, described methods of measurements for the elastic coefficients, and discussed their physical interpretation in various alternate forms. Additionally, they extended the work of Biot (1955) on the interpretation of anisotropic poroelastic parameters and the ways to measure them.

Biot (1956) also utilized his theory to describe elastic wave propagation in saturated porous bodies and, finally (Biot 1973), developed a theory of finite deformations of porous media, stating that the mechanics of porous media was then brought to the same level as the classical theory of finite deformations in elasticity.

Further developments in the basic equations of porous media theory have referred to the works of Biot. Geertsma (1957) summarized Biot's and Gassmann's theories and reformulated them in terms of compressibilities, which, as he claimed, were much easier to be measured experimentally. This approach was then used by Zimmermann (1986, 1991) to suggest the parameters convenient for description of deformable reservoirs. Geertsma (1966) was also the one who introduced the term *poroelasticity* with the reference to "Biot's work on the theory of the elasticity and viscoelasticity of fluid-

saturated porous solids." He emphasized the similarity between mathematical descriptions of the macroscopic poroelasticity and thermoelasticity theories.

Moreover, the 1950s were the time of the first known experimental works on deformable fluid-filled rock. Hall (1953) showed the importance of measuring the effective rock compressibility in calculating the hydrocarbon volume of an undersaturated reservoir. Hughes and Cook (1953) performed laboratory measurements of pore compressibility of sandstones for the purpose of making corrections for available pore space at reservoir depths. Fatt (1958, 1959) presented data needed to calculate the full set of Biot-Willis coefficients for a porous fluid-saturated sandstone.

Later in the XX century, poroelasticity theory was introduced in hydrogeology and geophysical applications. Verruijt (1969) derived the most general (linear) description of aquifer behavior obtained from Biot's theory. Haimson and Fairhurst (1969) considered poroelastic effects in describing the techniques for *in-situ* stress determination.

Development of experimental techniques, which allowed for separate control of the confining and pore pressures, provided further detailed description of the poroelastic parameters. Nur and Byerlee (1971), based on their tests on a sandstone, concluded that the expression for the effective stress should be modified by multiplying the pore pressure by the so-called Biot coefficient. Bishop (1976) extended Skempton's (1954) work on undrained pore pressure coefficient for rock and suggested improvements to experimental measurements.

Brown and Korringa (1975) generalized Gassmann's equation for the case of non-homogeneous material. Their work was used by Rice and Cleary (1976), who greatly facilitated the analyses of problems involving interaction between fluid and rock. With no special assumptions regarding the fluid and solid compressibilities, the coupled stress and fluid-flow fields were formulated as an extension of the Biot (1941) theory. The Biot moduli were written in terms of parameters related to the two limiting time scales, long and short term, of fluid-saturated material behavior. This formulation considerably simplified the interpretation of asymptotic poroelastic phenomena.

Palciauskas and Domenico (1982) described nonisothermal response of potential repository rock to heating. They used Rice and Cleary's (1976) notation to characterize the four isothermal elastic parameters and introduced some nonisothermal parameters related to fluid, solid, and pore volume expansivity.

Detournay and Cheng (1993) presented a seminal review of poroelasticity theory, as well as the analytical and numerical methods for solving some of its fundamental problems. The various approaches proposed in the literature were unified and related. Finally, Wang (2000) published a book on "Theory of linear poroelasticity with applications to geomechanics and hydrogeology," where the emphasis was given to physical interpretation of poroelastic variables, governing equations, and problem solutions.

The formulation of the basic concepts of poroelasticity and the development in laboratory equipment in the last third of the XX century enabled experimental measurements of the parameters needed for the solutions of geomechanics, hydrogeology, and reservoir engineering problems. A few of them are Mesri *et al.* (1976), Yew and Jogi (1978), Green and Wang (1986), Boutéca *et al.* (1991), Hart and Wang (1995, 2010), Fabre and Gustkiewicz (1997), Lockner and Stanchits (2002), and Sulem and Ouffroukh (2006).

It is worth mentioning that alternative approaches for describing fluid-filled porous media have also been developed using the formalism of mixture theories, but in practice they do not offer any advantage over the Biot theory (Katsube and Carroll 1987) and will not be considered in this work.

2.2 Isotropic poroelasticity

The notation and mechanical description of an isotropic poroelastic material from Detournay and Cheng (1973) are used in this section. The following agreement is preserved in the expressions presented: ∂ is a partial derivative, d represents an infinitesimal increment and is used in parameter definitions, and increments of quantities that are measured experimentally are designated by Δ. Also, summation by repeating indexes is assumed.

The Biot model of fluid-filled porous material is constructed on the conceptual model of

a coherent solid skeleton and a freely moving pore fluid. A material element that occupies volume V in a chosen reference state may be considered (Figure 2.1). On the macroscopic scale of the porous body under consideration, this volume element is viewed as an infinitesimal element subjected to a locally homogeneous infinitesimal elastic deformation. If the part of V taken by the interconnected pore space is denoted by V_ϕ, the pore volume, then ϕ_o

$$\phi_o = V_\phi / V \tag{2.1}$$

represents the porosity of the material element. V_s then is the part of V that is taken by the solid skeleton and non-connected pores (if present):

$$V_s = V - V_\phi \tag{2.2}$$

The material element will be called a representative volume element (RVE) if it consists of a sufficient volume of grains and void space such that a volume average of porosity approaches a stable limit. Each stress and strain variable is defined by its average value over the RVE. The stress state can be represented by the three-dimensional stress tensor σ_{ij} and written in terms of principal stresses σ_1, σ_2, σ_3 (Figure 2.1). The mean stress P is

$$P = \frac{\sigma_1 + \sigma_2 + \sigma_3}{3} = \frac{\sigma_{ii}}{3} \tag{2.3}$$

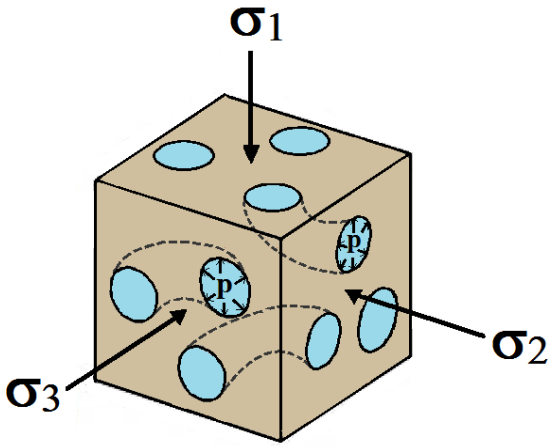

Figure 2.1: Representative volume element of porous rock with principal stresses and pore pressure.

The pore pressure p in the element is a scalar and is defined as the pressure in a hypothetical reservoir that is in equilibrium with this element, such that no fluid exchange takes place between the reservoir and the material element.

Two strain quantities can be introduced: the small strain tensor ε_{ij} and the variation of fluid content ζ. The latter is defined as the variation of fluid volume per unit volume of porous material due to diffusive fluid mass transport:

$$\frac{\partial \zeta}{\partial t} = \frac{\partial q_i}{\partial x_i} \tag{2.4}$$

where t represents time and q_i is the specific discharge vector, which describes the motion of the fluid relative to the solid in the x_i direction (see section 4.1.3). The variation in the fluid content can also be defined through the fluid mass content approach of Rice and Cleary (1976):

$$\zeta = -dm_f / \rho_f \tag{2.5}$$

where ρ_f is the density of the fluid in the element and dm_f is the change of its mass over the volume of the element.

The first invariant of ε_{ij}, its trace ε, is called volume strain:

$$\varepsilon = \varepsilon_{kk} \tag{2.6}$$

The sign convention is that positive normal stress implies compression, meaning that ε_{kk} is positive in compaction and positive ζ corresponds to a loss of fluid by a porous solid.

The stress and the pore pressure are the conjugate quantities of the strain and the variation of the fluid content, respectively. The work increment dW associated with the strain increment $d\varepsilon_{ij}$ and $d\zeta$, in the presence of the stress σ_{ij} and pore pressure p, is

$$dW = \sigma_{ij} d\varepsilon_{ij} + p d\zeta = \varepsilon_{ij} d\sigma_{ij} + \zeta dp \tag{2.7}$$

The latter equality is written by assuming reversibility (no energy dissipated during a closed loading cycle) of the deformation process. This assumption was used by Biot (1941), along with linearity between the stress (σ_{ij}, p) and the strain (ε_{ij}, ζ), to write the

constitutive relations by extending the known elastic expressions. Biot's constitutive constants, which characterize the coupling between the solid and fluid stress and strain, cannot be directly measured in lab experiments, so they are not presented here. Instead, the response of fluid-saturated porous material is described in terms of two limiting behaviors, drained and undrained, the definitions of which follow.

Drained behavior

The drained condition corresponds to the case of constant pore pressure: $\Delta p = 0$. This condition can be achieved by connecting a specimen to a reservoir where fluid pressure p is preserved constant (Figure 2.2). For simplification, the constitutive equations related to the drained material behavior will be written only for the case of zero pore pressure $p = 0$.

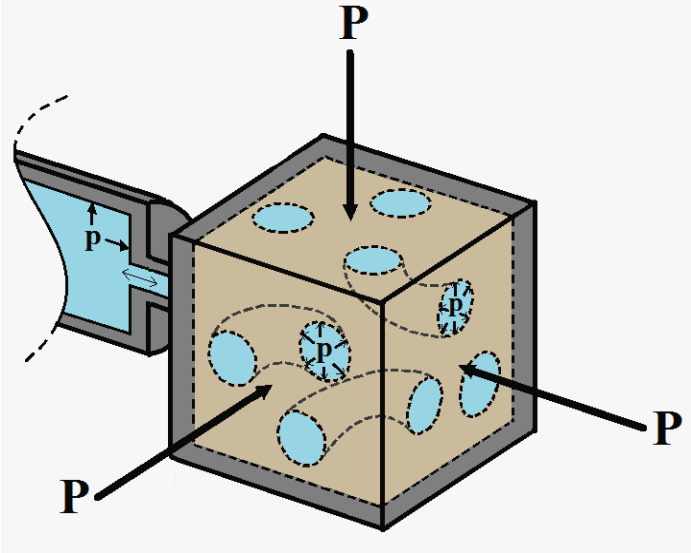

Figure 2.2: Schematic representation of a drained compression test.

Drained bulk modulus K can be written in terms of changes of the external mean stress P with specimen volume strain ε:

$$K = \left.\frac{dP}{d\varepsilon}\right|_{dp=0} \tag{2.8}$$

If the case of zero pore pressure is assumed, then from the linearity of the stress-strain relationships, the volume strain can be written as

$$\varepsilon = \frac{P}{K} \tag{2.9}$$

and ζ is proportional to ε:

$$\zeta = \alpha\varepsilon \tag{2.10}$$

where constant α is the coefficient, which is the ratio of the fluid volume gained or lost in a material element due to loading, to the volume change of that element, when the pore pressure is preserved constant. Since the change of fluid volume in the element cannot be greater than the total volume change, and both of them should have the same sign:

$$0 \le \alpha \le 1 \tag{2.11}$$

Note that α is exactly one if all of the volume strain is due to pore volume change equal to the change of fluid volume. It means that the solid phase can be considered incompressible, which is the case for soft soil, but not for rock, where the amount of pore volume change is comparable to the increment in the amount of solid phase.

Undrained behavior

The undrained response characterizes the condition where the fluid is trapped in the porous solid such that $\zeta = 0$. The undrained test can be represented by the specimen, subjected to the mean stress P, with a casing or jacket around it, which does not allow fluid escaping or entering the specimen but does allow the measurement of pore pressure (Figure 2.3).

Undrained bulk modulus can then be defined as

$$K_u = \left.\frac{dP}{d\varepsilon}\right|_{\zeta=0} \tag{2.12}$$

Because ζ is assumed to be a linear function of P and p, the following relationship holds for the undrained case ($\zeta = 0$):

$$p = BP \tag{2.13}$$

where B is the Skempton (1954) pore pressure coefficient.

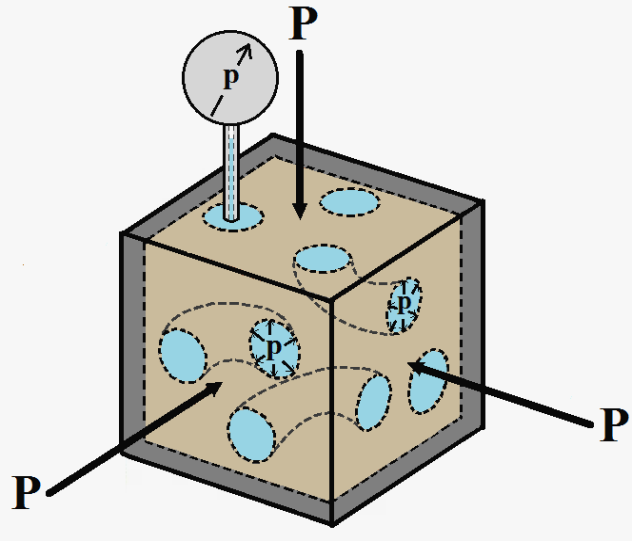

Figure 2.3: Schematic representation of an undrained compression test.

The volumetric response under undrained condition can be written as

$$\varepsilon = \frac{P}{K_u} \tag{2.14}$$

The bulk modulus of the pore fluid K_f can also be defined under undrained conditions:

$$K_f = V_f \left. \frac{dp}{dV_f} \right|_{\zeta=0} \tag{2.15}$$

where V_f is the volume of the fluid.

Generally, the drained and undrained conditions are the limiting cases of slow and fast loading, respectively. Little fluid exits or enters the RVE if the loading is rapid, hence $\zeta = 0$ under the undrained condition. When the fluid flow has enough time to equilibrate with the external boundary, the fluid pressure is constant in RVE, $dp = 0$, which is the characteristic of the drained response.

For the drained condition, the increase in load is taken by the rock skeleton only. So the specimen deforms more than if the test would be performed under the undrained condition, where the pore fluid takes part of the loading and also compresses. Hence,

$$0 < K \leq K_u \tag{2.16}$$

Constitutive equations

The constitutive equations of an isotropic poroelastic material can be separated into deviatoric response:

$$e_{ij} = \frac{1}{2G} s_{ij} \tag{2.17}$$

where G is the material's shear modulus and s_{ij} and e_{ij} denote deviatoric stress and strain:

$$s_{ij} = \sigma_{ij} - P\delta_{ij} \tag{2.18}$$

$$e_{ij} = \varepsilon_{ij} - \frac{\varepsilon}{3}\delta_{ij} \tag{2.19}$$

where δ_{ij} is the Kronecker delta, and volumetric response, which can be written based on the linearity of stress-strain relationships and equations (2.9), (2.10), and (2.14):

$$\varepsilon = \frac{1}{K}\left(P - \alpha p\right) \tag{2.20}$$

$$\zeta = \frac{\alpha}{K}\left(P - \frac{p}{B}\right) \tag{2.21}$$

Considering drained ($p = 0$) and undrained conditions for equations (2.20) and (2.21), the following expression can be obtained for the Skempton coefficient B:

$$B = \frac{K_u - K}{\alpha K_u} \tag{2.22}$$

The volumetric relations can inversely be written as

$$P = K_u\varepsilon - M\alpha\zeta \tag{2.23}$$

$$p = M\left(\alpha\varepsilon - \zeta\right) \tag{2.24}$$

where M is sometimes called the Biot modulus:

$$M = \frac{K_u - K}{\alpha^2} \tag{2.25}$$

M is also the inverse of a storage coefficient (Biot and Willis 1957; Green and Wang 1986), widely used in reservoir geomechanics and defined as the increase of fluid content due to an increase in pore pressure while preserving the volume strain constant:

$$\frac{1}{M} = \left.\frac{\partial \zeta}{\partial p}\right|_{d\varepsilon=0} \tag{2.26}$$

The presented constitutive model describes the response of the material as a whole, without taking into account the individual contributions of its solid and fluid constituents. These contributions are considered if a micromechanical approach is used. For the needs of this research, the easiest way to introduce this approach is through the so-called unjacketed condition.

Unjacketed behavior

The unjacketed test was proposed by Biot and Willis (1957) and is characterized by equal increments in mean stress and pore pressure: $dP = dp$. It can be seen as a test where the specimen with no jacket or membrane is loaded by a fluid. This fluid is allowed to penetrate inside the specimen and thus equilibrate the mean stress with the pore pressure (Figure 2.4). The test can also be carried out on a jacketed specimen by imposing equal increments of pore pressure and mean stress, without the requirement of the equality of the absolute values of those.

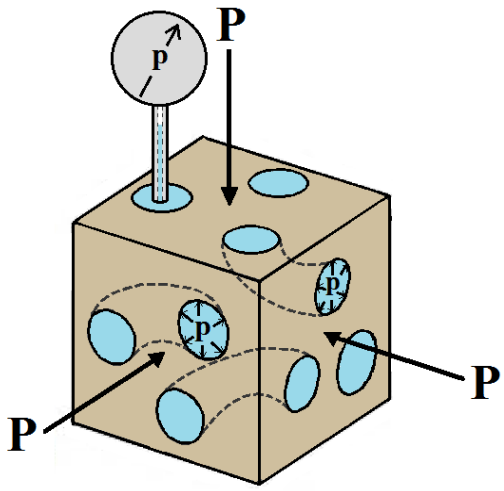

Figure 2.4: Schematic representation of unjacketed compression test.

Rice and Cleary (1976) introduced two new material constants: unjacketed bulk modulus K_s' and unjacketed pore volume bulk modulus K_s" as

$$K_s' = \left.\frac{dP}{d\varepsilon}\right|_{dP=dp} \tag{2.27}$$

$$K_s'' = V_\phi \left.\frac{dP}{dV_\phi}\right|_{dP=dp} \tag{2.28}$$

Generally, the coefficients K_s' and K_s" are different: K_s' is related to the total volume change in unjacketed loading, while K_s" is associated with the change only in the pore volume V_ϕ. However, under certain conditions, they can be both identified with the bulk modulus K_s of the solid constituent:

$$K_s = V_s \left.\frac{dP}{dV_s}\right|_{dP=dp} \tag{2.29}$$

Assuming that the rock has fully connected pore space, all points of the solid phase may be taken as elastically isotropic with the same local bulk modulus K_s, and both fluid and solid are chemically inert for the time scale of the tests, it can be shown that (Rice and Cleary 1976):

$$K_s = K_s' = K_s'' \tag{2.30}$$

However, this assumption may not be valid for sedimentary rocks where intergranular cement and pore lining have different elastic properties (Green and Wang 1986; Hart and Wang 2010). The significant difference between K_s' and K_s" can also be a consequence of the existence of non-connected pore space (Detournay and Cheng 1993).

Now, if the constitutive response (2.20) is considered under the unjacketed condition ($P = p$), it can be shown that α, sometimes referred to as the Biot coefficient (Nur and Byerlee 1971; Wang 2000), is

$$\alpha = 1 - \frac{K}{K_s'} \tag{2.31}$$

and from (2.11)

$$0 < K \le K_s' \tag{2.32}$$

Also, a more precise bound for K was established by Hashin and Shtrikman (1961) for a material that was considered to be both microscopically and macroscopically isotropic:

$$\frac{K}{K_s} \le 1 - \frac{3\phi_o}{2 + \phi_o} \tag{2.33}$$

Relationships between the parameters

The relationship between drained and undrained bulk moduli is called generalized Gassmann's equation (Brown and Korringa 1975) and can be written as

$$K_u = K + \frac{\alpha^2 K}{(1-\alpha)\alpha + \phi_o K\left(\frac{1}{K_f} - \frac{1}{K_s''}\right)} \tag{2.34}$$

It can be independently derived from Biot's equations or from the general expression for Skempton coefficient B (see section 3.5).

Shear modulus G, which governs linear deviatoric response, is usually calculated from the dry (or drained) uniaxial compression test. Equations (2.22), (2.31), and (2.34) provide the relationships between the introduced parameters K, K_u, B, α, K_s', K_s'', ϕ, and K_f, which govern volumetric poroelastic response. Hence, the measurements of at least five of these parameters (*e.g.* K, K_u, B, ϕ, and K_f) are required to calculate the full set. However, usually the porosity of rock is known or can be measured in a simple test (see section 4.1.3), so only the measurements of four out of the seven parameters left are needed.

If both drained and undrained bulk moduli and Skempton coefficient are available from test data, then equations (2.22), (2.31), and (2.34) have four unknowns. If it can be assumed that $K_s = K_s' = K_s''$, then α, K_s, and K_f can be calculated. Also, if the assumption is made on the value of K_f, based on the knowledge of the fluid properties and saturation (see section 3.5), and no restrictions are imposed on K_s' and K_s'', then the solution of the system of poroelastic relationships provides the values of α, K_s', and K_s'' (Makhnenko and

Labuz 2012). For rock, where drained testing for some reason may not be possible (*e.g.* low-permeable shale) and only K_u and B are available from the undrained test, certain assumptions on K_f and $K_s = K_s' = K_s''$ must be made to calculate the rest of poroelastic parameters (Makhnenko *et al.* 2011).

In this work, the measurements of all parameters, except for the unjacketed pore bulk modulus K_s'', are performed using different testing methods described in Chapter 3.

Alternative constitutive equations

The emphasis on the volumetric response in the previous sections reflected the choice of bulk moduli K and K_u as a part of fundamental set of material constants. Alternatively, drained and undrained Poisson's ratios, ν and ν_u, can be chosen for the presentation of the linear theory. They are related to K, K_u, and G according to

$$\nu = \frac{3K - 2G}{2(3K + G)} \tag{2.35}$$

$$\nu_u = \frac{3K_u - 2G}{2(3K_u + G)} \tag{2.36}$$

From inequality (2.16), it follows

$$\nu \le \nu_u \le 0.5 \tag{2.37}$$

where $\nu_u = 0.5$ and $\alpha = 1$ hold for the case of incompressible constituents, which is characterized by the strongest poroelastic effect (this is the case for soft soil). In case of $\nu_u \cong \nu$, the effect of undrained loading disappears.

The Skempton pore pressure coefficient B and the Biot modulus M can also be expressed in terms of ν and ν_u:

$$B = \frac{3(\nu_u - \nu)}{\alpha(1 - 2\nu)(1 + \nu_u)} \tag{2.38}$$

$$M = \frac{2G(\nu_u - \nu)}{\alpha^2(1 - 2\nu_u)(1 - 2\nu)} \tag{2.39}$$

Storage coefficient S is related to M according to

$$S = \frac{(1-\nu_u)(1-2\nu)}{M(1-\nu)(1-2\nu_u)} \tag{2.40}$$

S represents the storage coefficient defined under the particular conditions of uniaxial strain and constant normal stress in the direction of the strain (Green and Wang 1986). In case of $\nu_u \cong \nu$, $S = 1/M$.

The constitutive equations (2.20), (2.21), (2.23), and (2.24) are now rewritten in terms of G, α, ν, and ν_u. The strain-stress relation (2.20) takes the form

$$2G\varepsilon_{ij} = \sigma_{ij} - \frac{\nu}{1+\nu}\sigma_{kk}\delta_{ij} - \frac{\alpha(1-2\nu)}{1+\nu}p\delta_{ij} \tag{2.41}$$

and it can be written as

$$\sigma_{ij} - \alpha p\delta_{ij} = 2G\varepsilon_{ij} + \frac{2G\nu}{1-2\nu}\varepsilon\delta_{ij} \tag{2.42}$$

These relations are similar to those for a drained elastic solid with (σ_{ij} - $\alpha p\delta_{ij}$) being an effective stress, so α is sometimes called the effective stress coefficient (Nur and Byerlee 1971). For the case of $p = 0$, equations (2.41) and (2.42) reduce to the drained (or dry) constitutive equations.

If ζ is taken as the coupling term, then the constitutive expressions become

$$2G\left(\varepsilon_{ij} - \frac{B}{3}\zeta\delta_{ij}\right) = \sigma_{ij} - \frac{\nu_u}{1+\nu_u}\sigma_{kk}\delta_{ij} \tag{2.43}$$

$$\sigma_{ij} = 2G\varepsilon_{ij} + \frac{2G\nu_u}{1-2\nu_u}\varepsilon\delta_{ij} - \alpha M\zeta\delta_{ij} \tag{2.44}$$

Equations (2.41) – (2.44) clearly show the elastic character of the poroelastic material in its two limiting behaviors, drained ($p = 0$) and undrained ($\zeta = 0$).

Also, a modification of equation (2.21)

$$2G\zeta = \frac{\alpha(1-2\nu)}{1+\nu}\left(\sigma_{kk} - \frac{3}{B}p\right) \tag{2.45}$$

and equation (2.24) present two different forms of the response equation for the pore fluid.

Skempton *A* coefficient

Another coefficient describing deviatoric poroelastic response of fluid-filled material can be introduced. In Biot's theory, changes in deviatoric stress do not induce pressure changes. However, Skempton (1954) allowed for the possibility that deviatoric stresses also induce pore pressure changes for undrained conditions and some experiments prove that (Wang 1997). Skempton expressed the relationship for the induced pore pressure for conventional triaxial compression conditions ($\Delta\sigma_2 = \Delta\sigma_3$ and $|\Delta\sigma_1| > |\Delta\sigma_3|$) as

$$\Delta p = B\left(\Delta\sigma_3 + A\left(\Delta\sigma_1 - \Delta\sigma_3\right)\right) = B\left(\frac{1}{3}\left(\Delta\sigma_1 + 2\Delta\sigma_3\right) + \frac{3A-1}{3}\left(\Delta\sigma_1 - \Delta\sigma_3\right)\right) \tag{2.46}$$

where A is another Skempton coefficient measured experimentally.

Henkel (1960) generalized (2.46) to a three-dimensional state of stress:

$$\Delta p = B\left(\frac{1}{3}\left(\Delta\sigma_1 + \Delta\sigma_2 + \Delta\sigma_3\right) + \frac{3A-1}{\sqrt{2}}\tau_{oct}\right) \tag{2.47}$$

where the octahedral shear stress τ_{oct} is defined by (Jaeger and Cook 1976)

$$\tau_{oct} = \frac{1}{3}\left(\left(\sigma_1 - \sigma_3\right)^2 + \left(\sigma_1 - \sigma_2\right)^2 + \left(\sigma_2 - \sigma_3\right)^2\right)^{1/2} \tag{2.48}$$

A value of $A < 1/3$ means that the undrained pore pressure decreases if only shear stress is applied, and if $A > 1/3$, the induced pore pressure increases comparing to the case of only mean stress applied.

The methods to experimentally measure the alternative parameters ν, ν_u, and A governing isotropic poroelastic deformation of fluid-saturated rock are described in Chapter 3.

2.3 Anisotropic poroelasticity

For fundamental reasons required to produce a phemenological theory, Biot necessarily assumed that the medium has constant porosity and is homogeneous, linear, and isotropic. These fundamental requirements are often violated for earth materials. Bedding, mineral fabric, and aligned microcracks are common causes of intrinsic anisotropy in rock. Analytical solutions (Abousleiman *et al.* 1996) showed that modeling anisotropic material as an equivalent isotropic one can lead to unexpected and erroneous results, so these properties should be considered in discussions of anisotropic poroelastic response.

The extension of the isotropic theory to an anisotropic one for elastic fluid-saturated porous media was achieved by Biot in 1955 based on the formality of generalized Hooke's law. Various anisotropic poromechanical properties were described by Biot and Willis (1957). However, the experimental procedures suggested for their determination are extremely difficult to achieve. Thompson and Willis (1991) followed the interpretation of Rice and Cleary (1976) and reformatted the anisotropic poroelastic constitutive relations in terms of drained and undrained parameters. The practical model for their measurement was suggested by Cheng (1997) and is reviewed.

Using "engineering notation," stresses and strains are expressed as column vectors:

$$\underline{\sigma} = \lfloor \sigma_{xx} \quad \sigma_{yy} \quad \sigma_{zz} \quad \tau_{xy} \quad \tau_{xz} \quad \tau_{yz} \rfloor^{\mathrm{T}} \tag{2.49}$$

$$\underline{\varepsilon} = \lfloor \varepsilon_{xx} \quad \varepsilon_{yy} \quad \varepsilon_{zz} \quad \gamma_{xy} \quad \gamma_{xz} \quad \gamma_{yz} \rfloor^{\mathrm{T}} \tag{2.50}$$

The constitutive equations of linear poroelasticity relate small changes in strain and fluid pressure to incremental stress variation about some ambient stress state and can be expressed as

$$\underline{\sigma} = \underline{\underline{M}}\,\underline{\varepsilon} + \underline{\alpha} p \tag{2.51}$$

$$p = M\left(\underline{\alpha}^{\mathrm{T}}\,\underline{\varepsilon} - \zeta\right) \tag{2.52}$$

where $\underline{\underline{M}}$ is the drained stiffness matrix (equivalent to Hooke's law elastic moduli) and $\underline{\alpha}$ represents the generalized Biot effective stress coefficients (Biot and Willis 1957). The inverse form of (2.51) and (2.52) gives the constitutive equations in terms of the compliance matrix $\underline{\underline{C}}$:

$$\underline{\varepsilon} = \underline{\underline{C}}\,\underline{\sigma} - \frac{C}{3}\underline{B}p \tag{2.53}$$

$$\zeta = C\left(\frac{1}{3}\underline{B}^{\mathrm{T}}\underline{\sigma} - p\right) \tag{2.54}$$

where $\underline{B}$ represents the generalized Skempton coefficients and C is a special three-dimensional storage coefficient.

The number of material coefficients defining the most general form of anisotropy is 28 (Biot 1955). The identification of all of these parameters requires a number of involved tests, where all applied stresses and corresponding strains should be precisely measured under different loading conditions. However, a more simple case can be considered since geomaterials are often transversely isotropic, meaning that there exists a rotational symmetry about the axis perpendicular to the bedding plane. In this case, the number of constitutive coefficients needed to fully characterize the response in equations (2.51) – (2.52) is reduced to eight. Cheng (1997) provides formulas for expressing drained stiffness tensor coefficients in terms of drained Young's moduli in the transverse plane of symmetry $E = E_x = E_y$ and parallel to the sample axis $E' = E_z$, and two Poisson's ratios ν and ν' (Figure 2.5). The drained Poisson's ratio ν represents the expansion in the plane of isotropy due to a compression stress applied in the same plane. Similarly, ν' corresponds to the transverse expansion in the plane of isotropy due to a compression stress normal to it.

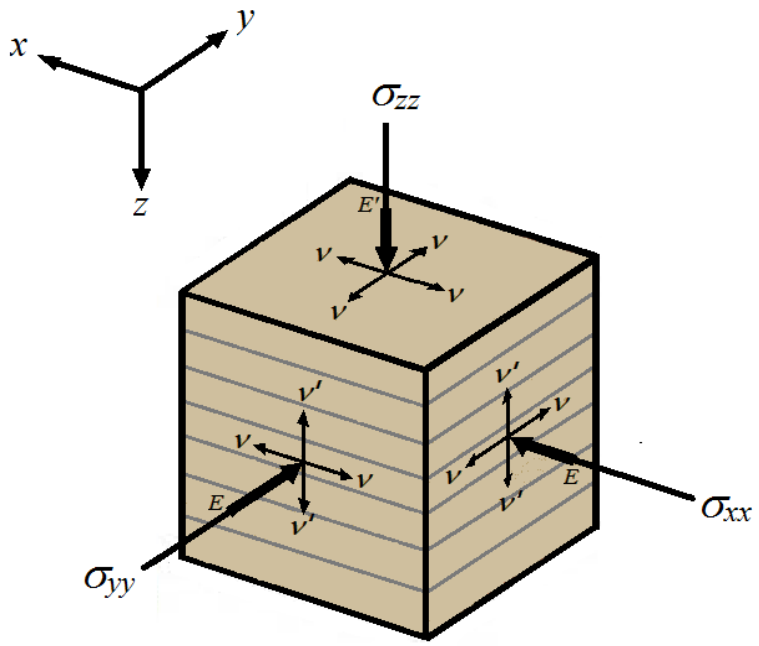

Figure 2.5: Transversely isotropic parameters.

For a transversely isotropic system, $\underline{\underline{M}}$ is composed of

$$\underline{\underline{M}} = \begin{pmatrix} M_{11} & M_{12} & M_{13} & 0 & 0 & 0 \\ M_{12} & M_{11} & M_{13} & 0 & 0 & 0 \\ M_{13} & M_{13} & M_{33} & 0 & 0 & 0 \\ 0 & 0 & 0 & G & 0 & 0 \\ 0 & 0 & 0 & 0 & G' & 0 \\ 0 & 0 & 0 & 0 & 0 & G' \end{pmatrix} \tag{2.55}$$

where individual terms are expressed as

$$M_{11} = \frac{E^2\left(E' - Ev'^2\right)}{\Lambda} \tag{2.56}$$

$$M_{12} = \frac{E^2\left(E'v + Ev'^2\right)}{\Lambda} \tag{2.57}$$

$$M_{13} = \frac{E^2E'\left(v' + vv'\right)}{\Lambda} \tag{2.58}$$

$$M_{33} = \frac{E'^2 E\left(1-\nu^2\right)}{\Lambda} \tag{2.59}$$

$$G = \left(M_{11} - M_{12}\right)/2 \tag{2.60}$$

with $\Lambda = E\left(1+\nu\right)\left(E'-E'\nu - 2E\nu'^2\right)$.

The compliance matrix can be written explicitly as

$$\underline{\underline{C}} = \begin{pmatrix} 1/E & -\nu/E & -\nu'/E' & 0 & 0 & 0 \\ -\nu/E & 1/E & -\nu'/E' & 0 & 0 & 0 \\ -\nu'/E' & -\nu'/E' & 1/E' & 0 & 0 & 0 \\ 0 & 0 & 0 & 1/G & 0 & 0 \\ 0 & 0 & 0 & 0 & 1/G' & 0 \\ 0 & 0 & 0 & 0 & 0 & 1/G' \end{pmatrix} \tag{2.61}$$

Other coefficients become

$$\underline{\alpha} = \lfloor \alpha \quad \alpha \quad \alpha' \quad 0 \quad 0 \quad 0 \rfloor^{\mathrm{T}} \tag{2.62}$$

$$\underline{B} = \lfloor B \quad B \quad B' \quad 0 \quad 0 \quad 0 \rfloor^{\mathrm{T}} \tag{2.63}$$

with

$$\alpha = 1 - \frac{M_{11} + M_{12} + M_{13}}{3K_s'} \tag{2.64}$$

$$\alpha' = 1 - \frac{M_{33} + 2M_{13}}{3K_s'} \tag{2.65}$$

$$B = \frac{3\left(C_{11} + C_{12} + C_{13}\right) - 1/K_s'}{C} \tag{2.66}$$

$$B' = \frac{3\left(C_{33} + 2C_{13}\right) - 1/K_s'}{C} \tag{2.67}$$

The storage coefficient C is given by

$$C = \left(C^* - 1/K_s'\right) + \phi_o\left(1/K_f - 1/K_s''\right) \tag{2.68}$$

where

$$C^* = 2C_{11} + 2C_{12} + 4C_{13} + C_{33} \tag{2.69}$$

Biot modulus M under transversely isotropic conditions takes the following form:

$$M = \frac{K_s'}{(1 - K^*/K_s') - \phi_o(1 - K_s''/K_f)} \tag{2.70}$$

where K^* can be calculated as

$$K^* = (2M_{11} + 2M_{12} + 4M_{13} + M_{33})/9 \tag{2.71}$$

The variation of fluid content ζ (equation 2.52) can also be written as

$$\zeta = -\frac{p}{M} + \alpha\varepsilon_{xx} + \alpha\varepsilon_{yy} + \alpha'\varepsilon_{zz} \tag{2.72}$$

As can be seen from equations (2.51) and (2.72), eight material properties are required to define a poroelastic transversely isotropic material, such as those mentioned: E, E', ν, ν', G', α, α', and M. However, they need not necessarily be measured directly. They can be determined from other parameters, which are more convenient to measure in the laboratory, for example, under undrained conditions. A set of relations between the drained and undrained material properties is (Cheng 1997):

$$M_{11} = M_{11}^u - \alpha^2 M \tag{2.73}$$

$$M_{12} = M_{12}^u - \alpha^2 M \tag{2.74}$$

$$M_{13} = M_{13}^u - \alpha\alpha' M \tag{2.75}$$

$$M_{33} = M_{33}^u - \alpha'^2 M \tag{2.76}$$

$$\alpha = \frac{1}{3M}\left[B\left(M_{11}^u + M_{12}^u\right) + B'M_{13}^u\right] \tag{2.77}$$

$$\alpha' = \frac{1}{3M}\left(2BM_{13}^u + B'M_{33}^u\right) \tag{2.78}$$

The superscript u indicates the undrained state and M_{ij}^u are the elements of the undrained elastic matrix that can be expressed in terms of undrained Young's moduli and Poisson's

ratios by equations (2.56) – (2.59). The relation between the variations of pore pressure and stresses in the undrained state is defined through the Skempton coefficients:

$$p^u = \frac{1}{3}\left(B\sigma^u_{xx} + B\sigma^u_{yy} + B'\sigma^u_{zz}\right) \tag{2.79}$$

Moreover, based on the positive definiteness of the strain energy function, the following inequalities between transversely isotropic poroelastic parameters must hold (Loret *et al.* 2001):

$$1 + \frac{\left(\nu'^u - \nu'\right)^2}{(1-\nu)E'/2E - \nu'^2} < \frac{E'^u}{E'} \tag{2.80}$$

$$E < E^u < \frac{2E}{1+\nu} \tag{2.81}$$

2.4 Inelastic response

The inelastic response under drained and undrained condition can be described by the Vardoulakis (1996) model, which has been shown to closely predict the behavior of water-saturated sand. Sulem and Ouffroukh (2006) suggested a model describing inelastic response of a rock based on the increase of Poisson's ratio under undrained conditions; its calibration requires knowledge of the drained rock behavior under a wide range of confining pressure.

The constitutive model chosen for describing the inelastic response of fluid-infiltrated rock was formulated by Rice (1975) for the one-dimensional deformation state of confined shearing. It illustrates the hardening effect of dilatancy-induced pore pressure reductions. The model was reformulated by Rudnicki (1985) in terms of poroelastic parameters (Rice and Cleary 1976) for rock subjected to pore pressure p, shear stress τ, and mean (hydrostatic) stress P, and is reviewed here.

For a stress increment $d\tau, d(P-p)$ that involves continued inelastic deformation, the increments of shear strain $d\gamma$ and volume strain $d\varepsilon$ are

$$d\gamma = d\tau/G + d\gamma^p \tag{2.82}$$

$$d\varepsilon = -dP/K + d\varepsilon^p \tag{2.83}$$

where $d\gamma^p$ and $d\varepsilon^p$ are the increments of inelastic shear and volume strain, respectively. An increase in hydrostatic compression inhibits inelastic deformation in brittle rock. Thus, the inelastic increment of shear strain takes the form

$$d\gamma^p = (d\tau - \mu dP)/H \tag{2.84}$$

where H is an inelastic hardening modulus (Figure 2.6a) and μ is a friction parameter, which can be measured as the local slope of the yield surface, separating elastic and inelastic states, in the plane of τ and P-p (Figure 2.6b).

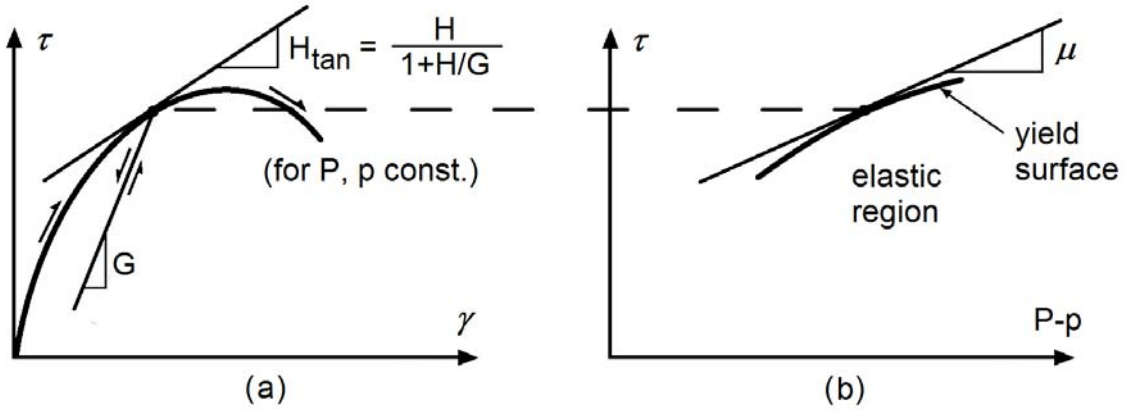

Figure 2.6: Stress-strain data for saturated rock (modified from Rice 1975). (a) Shear stress-strain relation under drained conditions, P and p being constant. (b) Effect of effective compressive stress on shear stress required for inelastic deformation.

For the case of drained response ($dp = 0$) and constant hydrostatic stress ($dP = 0$), $d\tau$ can be written as

$$d\tau = \frac{H}{1 + H/G} d\gamma \tag{2.85}$$

The inelastic volume strain arises from processes that accompany inelastic shear and its increment is assumed to be given by β, the dilatancy factor ($\beta < 0$ for compaction):

$$d\varepsilon^p = -\beta \cdot d\gamma^p \tag{2.86}$$

The sign convention here is again compression positive, meaning that when the specimen dilates its plastic volume strain is negative.

To include the effects of pore fluid pressure, the hydrostatic stress is replaced by the effective stress. For elastic deformation, the effective stress is written in Biot's form: $P - \alpha p$ (see equation 2.42). For inelastic deformation arising from opening and sliding of microcracks with small contact areas, Rice (1977) has shown that the appropriate form of the effective stress is $P - p$. This deduction is consistent with experimental observations on inelastic properties of brittle rock (Brace and Martin 1968). Thus, the increments of shear and volume strain are

$$d\gamma = d\tau/G + \left(d\tau - \mu\left(dP - dp\right)\right)/H \tag{2.87}$$

$$d\varepsilon = \left(dP - \alpha dp\right)/K + \beta\left(d\tau - \mu\left(dP - dp\right)\right)/H \tag{2.88}$$

Fluid mass content per unit volume m for elastic deformation can be expressed as $\rho \cdot \phi$, where ρ is the fluid density and ϕ is the apparent fluid volume fraction (Biot 1973). The expression obtained for ϕ by Detournay and Cheng (1993) is

$$\phi = \phi_o - \left(\alpha - \phi_o\right)\left(P - p\right)/K - \phi_o\left(1/K_s' - 1/K_s''\right)p \tag{2.89}$$

where ϕ_o is its reference value in the unstressed state, *i.e.* ϕ_o is the initial porosity of the rock.

The increment $d\phi = \phi - \phi_o$ is separated into an elastic portion, which is calculated as in the Biot theory, and inelastic increase in porosity $d\phi^p$, which was shown to be the plastic dilatancy: $d\phi^p = -\, d\varepsilon^p$ (Rice 1977; Viesca *et al.* 2008). Then, the increment of fluid mass content per unit volume can be written as

$$dm_f/\rho = \phi dp\left(1/K_f - 1/K_s''\right) - \alpha\left(dP - dp\right)/K - d\varepsilon^p \tag{2.90}$$

For undrained response, the change in fluid mass content per unit volume is zero. Setting $dm_f = 0$ in (2.90) and solving for dp yields (dP is taken as zero for convenience)

$$dp = \frac{-\beta K_{eff}}{H + \mu\beta K_{eff}} d\tau \tag{2.91}$$

where K_{eff} can be written as follows:

$$1/K_{eff} = \phi\left(1/K_f - 1/K_s''\right) + \alpha/K \tag{2.92}$$

Therefore, for dilatant inelastic deformation ($\beta > 0$), the pore fluid pressure tends to decrease. When (2.91) is substituted into (2.87) with $dP = 0$, the result is

$$d\tau = \frac{\left(H + \mu\beta K_{eff}\right)}{1 + \left(H + \mu\beta K_{eff}\right)/G} d\gamma \tag{2.93}$$

Because the hardening modulus has been augmented by the term $\mu\beta K_{eff}$, the response is stiffer and the rock is said to be "dilatantly hardened" (Figure 2.7). This term was introduced by Brace and Martin (1968) for the effect they observed in axisymmetric compression tests on brittle rock.

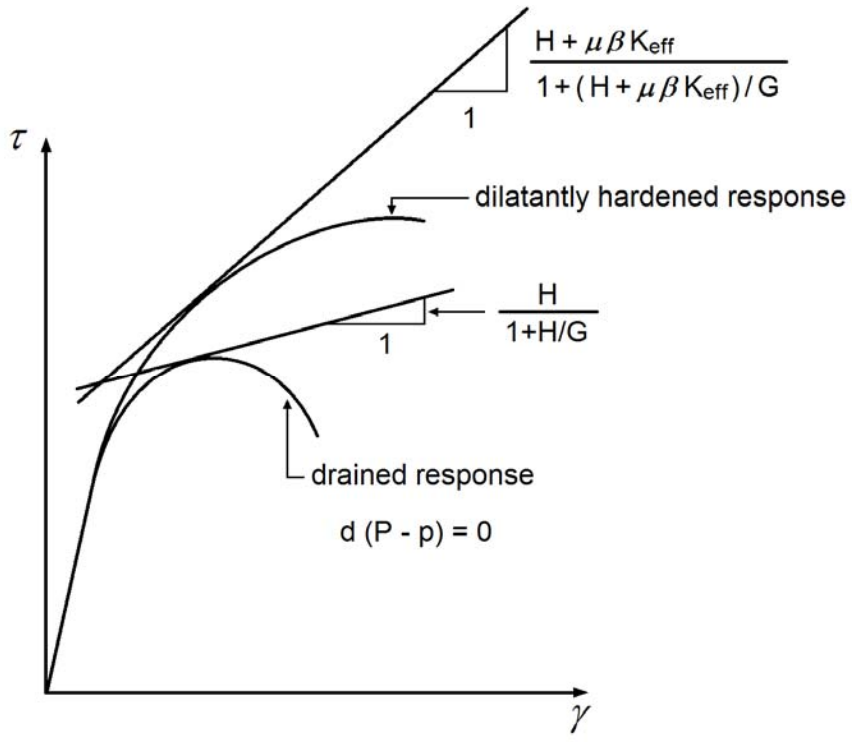

Figure 2.7: Dilatant hardening due to undrained conditions (modified from Rudnicki 1985).

Parameters μ, β, K_{eff}, and G could be stress dependent. For the sake of representing the hardening effect correctly, their development with the effective mean stress under which the testing is performed needs to be evaluated.

There are only a few experiments documenting dilatant hardening behavior. Brace and Martin (1968) investigated drained behavior of saturated rock under conventional triaxial compression. In experiments at loading rates greater than a critical value ($> 10^{-4}$ s^{-1} for Pottsville sandstone and $> 10^{-7}$ s^{-1} for Westerly granite), the rock was as much as 50% stronger than at constant pore pressure. It was explained by the fact that pore pressure did not have enough time to equilibrate in the dilating rock specimens; hence the effective confinement increased, which augmented the peak shear stress. Lei et *al.* (2011) observed that conducting conventional triaxial tests on Berea sandstone with the same initial confinement and pore pressure under drained and undrained conditions, the peak axial stress in the latter was 30% greater. However, the constitutive response of the rock under different drainage conditions was not described.

Chapter 3

Experimental techniques

3.1 Preliminaries

Drained, undrained, and unjacketed material parameters can be obtained by using a compression test with pore pressure involved. A jacket or membrane allows flow of the pore fluid out of or into the specimen during loading and, hence, constant pore pressure (drained test); the membrane prevents flow and allows pore pressure build-up (undrained test), or the equilibration of increments of pore and confining pressures (unjacketed test). Also, a dry test, when air in the pores is the only pore fluid, can be considered as the drained test (Green and Wang 1986; Rudnicki 1985), where the influence of the pore fluid on the rock constituents is neglected.

Apparatus for hydrostatic, plane strain, and conventional triaxial compression were utilized for the determination of the parameters governing the constitutive response of fluid-saturated porous rock. The description of these experimental techniques is given in sections 3.2 – 3.4.

In order that laboratory tests properly duplicate field conditions, it is desirable that lab specimens be fully saturated. When not fully saturated specimens are tested, the degree of saturation can be changing during the test and it brings another parameter into the problem. Conversely, if the condition of full saturation is achieved, bulk modulus of the pore fluid can be taken as that of the liquid used in the test. However, even a highly-permeable rock is a difficult material to completely saturate, as air bubbles get trapped and do not allow a liquid at low pressure to take their place. A method of gradual back pressure increase, suggested to achieve full saturation of laboratory specimens, is described in section 3.5.

Failure of rock involves the growth of microcracks from stress concentrators such as voids, inclusions, and dissimilar grain contacts. The irreversible damage results in inelastic strain and generates elastic waves known as acoustic emission (AE). The

transient waves propagate through the medium with very small amplitudes and high frequencies (100 – 2000 kHz), and the AE signals carry information about the source location and medium of propagation. For a wide variety of brittle rocks and over a wide range of confining pressures, dilatant deformation was found to be accompanied by small-scale fracturing (Scholz 1968). By monitoring AE in dry and fluid-saturated rock specimens, the growth of damage, the onset of failure, and fracture propagation can be identified. The AE technique is described in section 3.6.

The summary of the testing methods for determination of isotropic and transversely isotropic poroelastic parameters, as well as for the characterization of inelastic response of fluid-saturated rock, is given in section 3.7.

3.2 Hydrostatic compression

One of the simplest tests for measurements of the bulk material properties is hydrostatic compression. Specimens instrumented with sets of strain rosettes can be put inside a pressure chamber and subjected to hydrostatic (or mean) stress P (Figure 3.1).

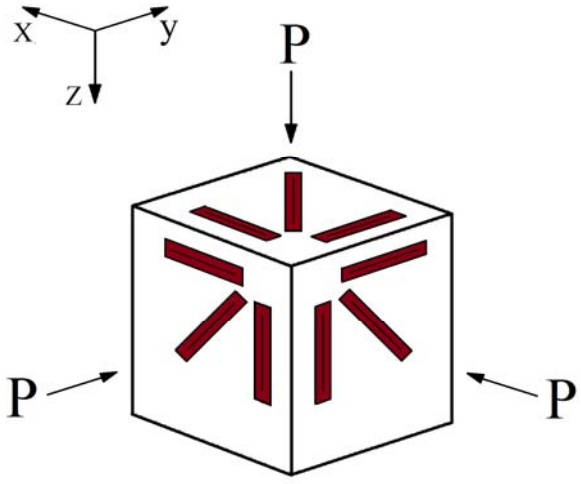

Figure 3.1: Sketch of the specimen for hydrostatic compression.

The three-dimensional strain tensor ε_{ij} can be expressed in terms of its components in the x, y, z coordinate system:

$$\varepsilon_{ij} = \begin{pmatrix} \varepsilon_{xx} & \varepsilon_{xy} & \varepsilon_{xz} \\ \varepsilon_{xy} & \varepsilon_{yy} & \varepsilon_{yz} \\ \varepsilon_{xz} & \varepsilon_{yz} & \varepsilon_{zz} \end{pmatrix} \tag{3.1}$$

Volume strain ε can be calculated as the trace of the strain tensor (the first invariant), and hence the measurement of the strains in any three perpendicular directions x, y, z are enough for the determination of ε:

$$\varepsilon = \varepsilon_{xx} + \varepsilon_{yy} + \varepsilon_{zz} \tag{3.2}$$

Experiments

Jacketed and unjacketed hydrostatic compression tests were performed on prismatic rock specimens instrumented with three sets of strain rosettes (Figure 3.2). Dry sandstone specimens covered with polyurethane were placed inside a pressure chamber and loaded to 60 MPa hydrostatic pressure. Measured jacketed bulk modulus K is

$$K = \left.\frac{\Delta P}{\Delta \varepsilon}\right|_{jacketed} \tag{3.3}$$

It can be considered as the drained bulk modulus of the material, because in the dry test pore pressure in the material does not change ($p = 0$).

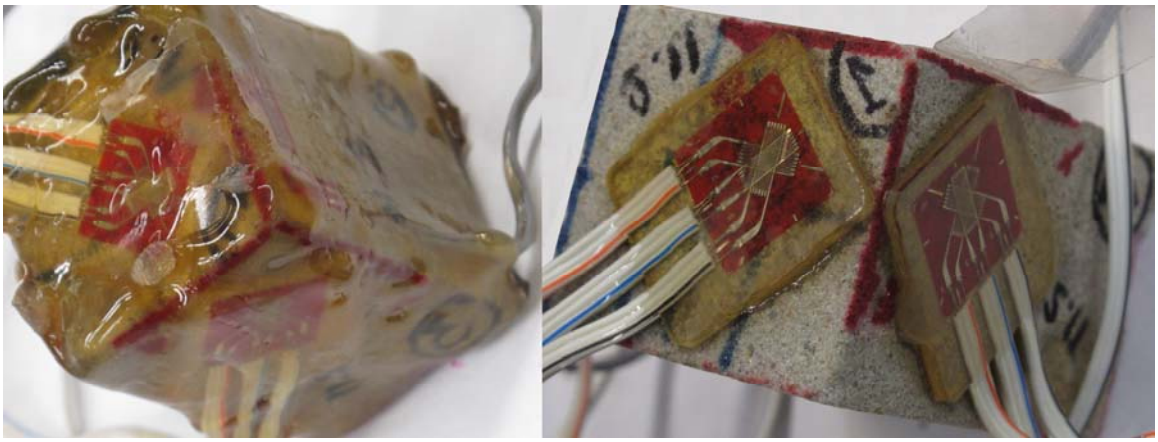

Figure 3.2: Specimen tested under jacketed (on the left) and unjacketed (on the right) compression.

After that, the jacket was removed and the confining fluid was allowed to penetrate into the rock. Hydraulic oil was used as the confining fluid, because it has no electrical effect on strain gage connections and no chemical effect on the tested rock in the short term. The unjacketed bulk modulus is calculated from

$$K_s' = \left.\frac{\Delta P}{\Delta \varepsilon}\right|_{unjacketed} \tag{3.4}$$

Additionally, principal values and directions of the strain tensor can be calculated from hydrostatic compression test using three strain rosettes designated in Figure 3.3.

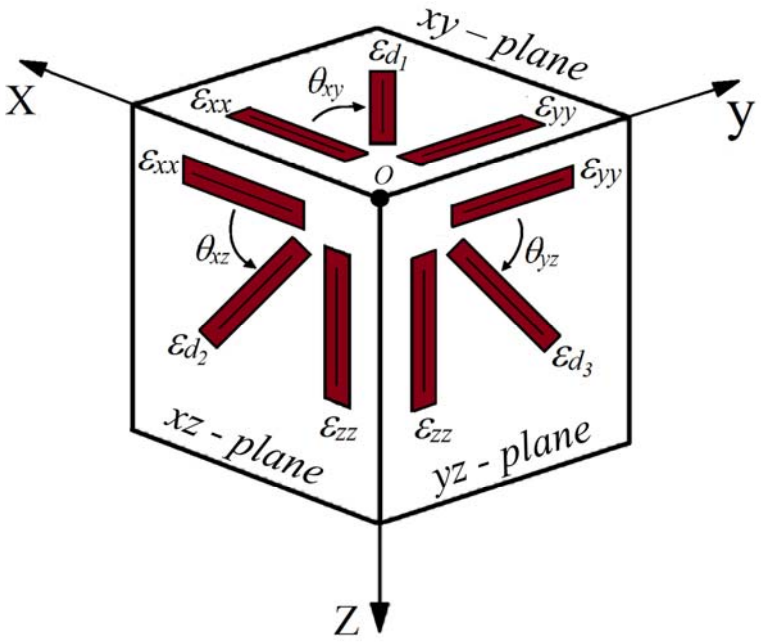

Figure 3.3: Orientation of strain gages for determination of principal strain directions and values in hydrostatic compression.

In terms of the elements of the strain tensor ε_{ij}, the strain measured with a diagonal gage d_i can be written as

$$\varepsilon_{d_i} = \ell_{d_i}^2 \varepsilon_{xx} + m_{d_i}^2 \varepsilon_{yy} + n_{d_i}^2 \varepsilon_{zz} + 2\ell_{d_i} m_{d_i} \varepsilon_{xy} + 2m_{d_i} n_{d_i} \varepsilon_{yz} + 2n_{d_i} \ell_{d_i} \varepsilon_{xz} \tag{3.5}$$

where the directional cosines are defined as

$$\ell_{d_i} = \cos(d_i, x), \quad m_{d_i} = \cos(d_i, y), \quad n_{d_i} = \cos(d_i, z) \tag{3.6}$$

For the configuration used in the testing, $\theta_{xy} = \theta_{xz} = \theta_{yz} = 45°$ and equations (3.6) for the strain gage d_1 in x-y plane become

$$\ell_{d_1} = \cos(\theta_{xy}) = \sqrt{2}/2, \quad m_{d_1} = \cos(90° - \theta_{xy}) = \sqrt{2}/2, \quad n_{d_1} = \cos(90°) = 0 \tag{3.7}$$

Hence

$$\varepsilon_{d_1} = \varepsilon_{xx}/2 + \varepsilon_{yy}/2 + \varepsilon_{xy} \tag{3.8}$$

and ε_{xy} can be calculated as

$$\varepsilon_{xy} = \varepsilon_{d_1} - (\varepsilon_{xx} + \varepsilon_{yy})/2 \tag{3.9}$$

Similarly,

$$\varepsilon_{xz} = \varepsilon_{d_2} - (\varepsilon_{xx} + \varepsilon_{zz})/2 \tag{3.10}$$

$$\varepsilon_{yz} = \varepsilon_{d_3} - (\varepsilon_{yy} + \varepsilon_{zz})/2 \tag{3.11}$$

So, all elements of the strain tensor (3.1) can be determined in the hydrostatic compression test. By calculating the eigenvalues and eigenvectors of ε_{ij}, the principal strains and their directions can be found. If the tested material is isotropic, then $\varepsilon_{xx} = \varepsilon_{yy} = \varepsilon_{zz}$; $\varepsilon_{xy} = \varepsilon_{yz} = \varepsilon_{xz} = 0$ and all principal strains are equal. However, for an anisotropic material, this condition is not preserved.

For the configuration shown in Figure 3.3, volume strain can be calculated as

$$\varepsilon = \varepsilon_{xx} + \varepsilon_{yy} + \varepsilon_{zz} = \varepsilon_{d_1} + \varepsilon_{d_2} + \varepsilon_{d_3} \tag{3.12}$$

From the equations (3.9) – (3.11), the following condition must be preserved:

$$\varepsilon_{xy} + \varepsilon_{yz} + \varepsilon_{xz} = 0 \tag{3.13}$$

3.3 Plane strain compression

3.3.1 Plane-strain apparatus

An apparatus for determining the constitutive response of soft rock, named the University of Minnesota Plane-Strain Apparatus, was designed and built based on a passive stiff-frame concept (Labuz *et al.* 1996). The biaxial device (U.S. Patent 5,063,785) is unique because it allows the failure plane to develop and propagate in an unrestricted manner. By placing the upper platen on a low friction linear bearing, the prismatic specimen, subjected to confining pressure and compressed axially, has the freedom to translate in the lateral direction if the deformation has localized. In addition, the apparatus was modified to allow pore pressure to be applied and monitored during an experiment.

The design of the plane-strain apparatus is illustrated in Figure 3.4; a brief explanation of the various parts of the device follows. A prismatic specimen (1) of height h = 86 mm, thickness t = 44 mm, and width w = 100 mm, is placed on a lower loading platen and confined laterally by a biaxial frame (3) in the form of a thick-walled cylinder. A pair of equally angled wedges allowing a tolerance of 0.5 mm in specimen width is used for fitting the specimen within the biaxial frame (Figure 3.5). The lower loading platen is connected through a load cell (4) to the base unit of the apparatus. The biaxial frame sits on the base unit guided by three pins, which ensures precise alignment. Another loading plate rests on top of the specimen; it is fixed with bolts to a linear bearing (2) sliding over a trackway. The apparatus is placed inside a large pressure cell to induce confining (lateral) stress. The cell is filled with hydraulic oil and the confining pressure is applied with a microprocessor-based hydraulic pump that maintains cell pressure at a constant value, within a tolerance of 0.1 MPa. Low friction teflon O-rings are used for sealing the loading piston and the upper cap, as well as the other connecting members of the pressure cell. Up to eight AE sensors (6) can be used to monitor the microseismic activity in the specimen. In addition, the apparatus was modified to allow pore pressure to be applied and monitored both upstream and downstream (7) by two pressure transducers.

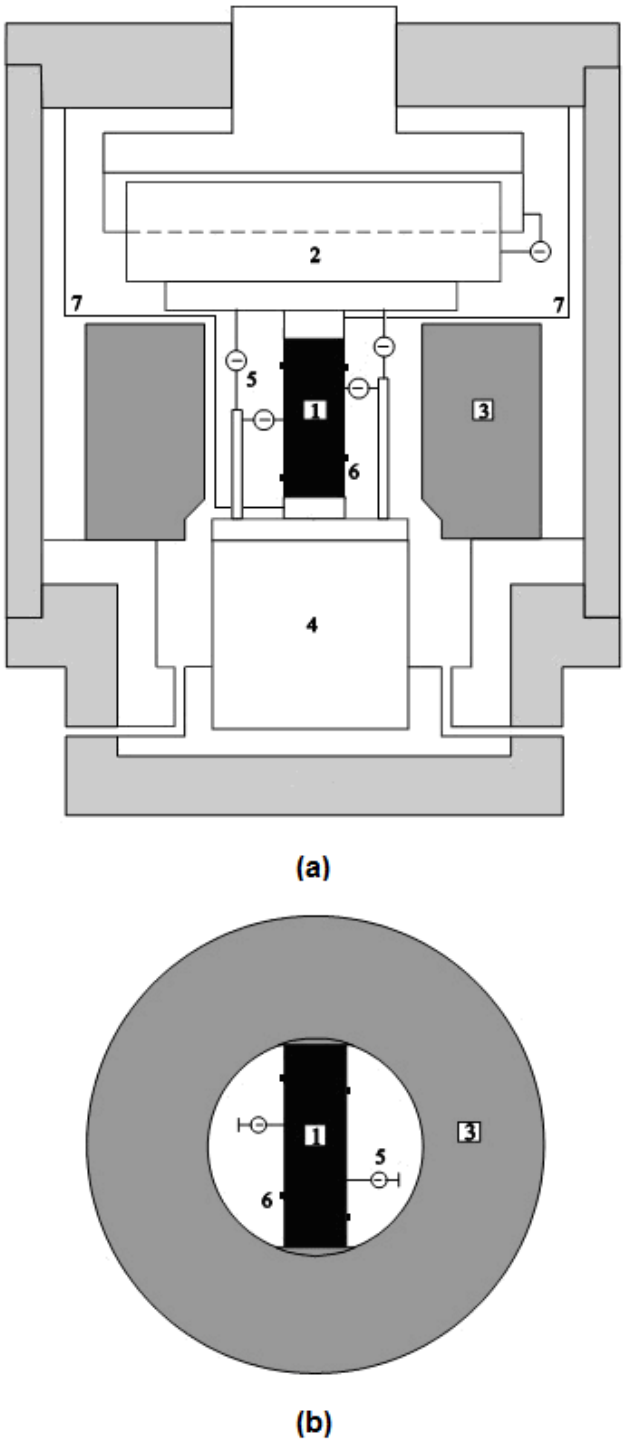

Figure 3.4: Sketch of the plane-strain apparatus: (1) specimen; (2) linear bearing; (3) biaxial frame; (4) load cell; (5) LVDTs; (6) AE sensors; (7) pore pressure tubes. (a) Elevation view. (b) Plan view.

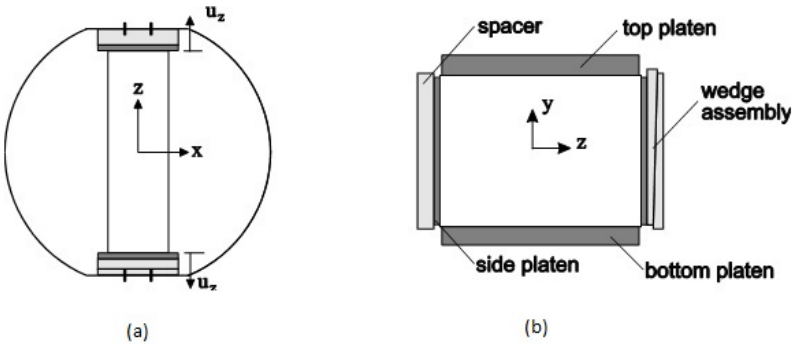

Figure 3.5: Specimen and wedge-spacer assembly. a. Plan view. b. Elevation view.

The axial force is measured below and above the specimen. A 1 MN load cell, with a sensitivity of 50 kN/mV, is mounted permanently to the cross head of the load frame and measures the axial force above the specimen. A confining pressure-compensated load cell (4), with a sensitivity of 5 kN/mV, is placed below the specimen, between the lower loading platen and the base unit.

Five RDP-Electrosense type D5/100/90, pressure resistant LVDTs (5) with a linear range of 2.5 mm and a sensitivity of 0.25 mm/mV measure the displacements of the specimen and the linear bearing. Two LVDTs are attached to the lower load cell and rest against the upper loading platen for measuring axial displacement. A pair of LVDTs are placed horizontally on opposite sides of the specimen exposed to confining pressure at 5 mm above and below the specimen's mid-height for measuring lateral displacement. The four LVDTs are mounted in place through LVDT holders attached with two aluminum posts to the lower load cell (Figure 3.6). One LVDT is attached to the linear bearing to record its horizontal (lateral) displacement.

For each specimen, all of the faces were ground so that opposite sides were parallel and adjacent sides were perpendicular within ±0.01 mm in 100 mm. The specimen (Figure 3.6) is assembled with porous stones between the upper and lower steel platens to provide uniform flow of the pore liquid; the porous stones are in contact with the 100 x 44 mm faces of the specimen. Two steel plates, 3 mm thick, contact the 44 x 86 mm faces, which are covered with stearic acid to reduce the friction between the platens and the specimen (Labuz and Bridell 1993). Two large (10-mm diameter) and eight small (4-mm diameter)

circular brass buttons, 1-mm thick, are glued to the specimen to provide a firm contact for the probes of the lateral LVDTs and AE sensors. The specimen, porous stones, and platens are held together with a custom jig and a thin layer of polyurethane is applied to the 100 x 86 mm faces to prevent confining fluid from penetrating the rock.

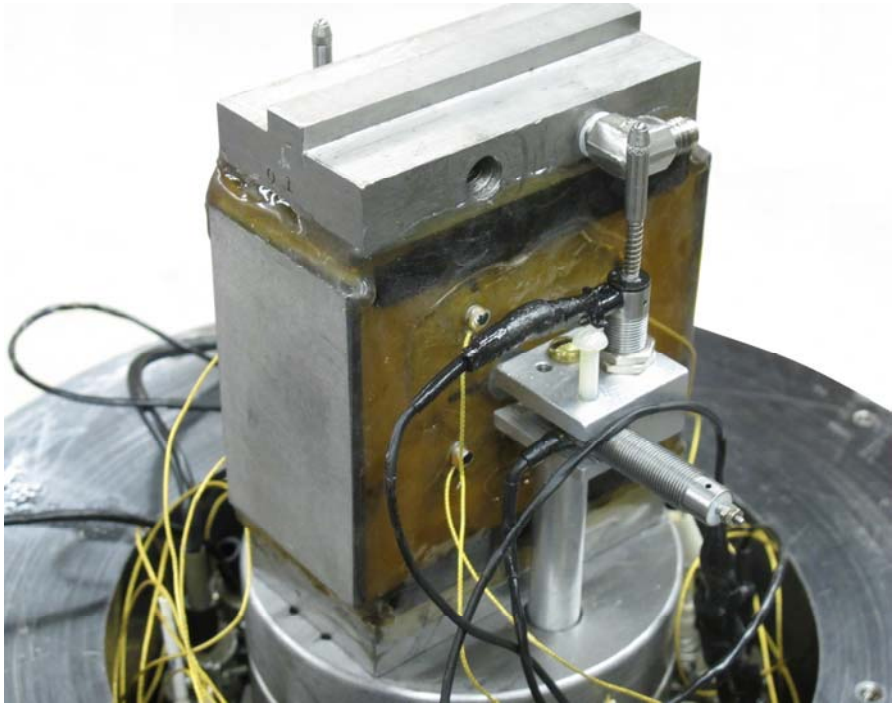

Figure 3.6: Specimen for plane strain testing with AE sensors and LVDTs.

3.3.2 Constitutive relationships in plane strain compression

Isotropic parameters

The prismatic specimen is wedged in the frame in a way that the stress in the plane strain direction (z-axis) is higher than the desired cell pressure. The principal directions are aligned with the Cartesian coordinates: $\varepsilon_1 = \varepsilon_{yy}$, $\varepsilon_2 = \varepsilon_{zz}$, $\varepsilon_3 = \varepsilon_{xx}$ ($\sigma_1 = \sigma_{yy}$, $\sigma_2 = \sigma_{zz}$, $\sigma_3 = \sigma_{xx}$). Generally, the frame restricts ε_2 and thus applies the intermediate principal stress σ_2. Deformation of the frame is measured by strain gages and can be related to the deformation of the specimen in that direction (Figure 3.7). Major principal stress σ_1 is applied in the vertical (axial) direction and is called axial stress, minor principal stress σ_3 is applied laterally by the confining fluid and is called cell pressure.

The intermediate principal stress cannot be controlled, but it can be calculated from generalized Hooke's law for an isotropic linearly elastic solid (see Appendix A for the details of calculating σ_2 for true triaxial testing):

$$\sigma_2 = E\varepsilon_2 + \nu(\sigma_1 + \sigma_3) \tag{3.14}$$

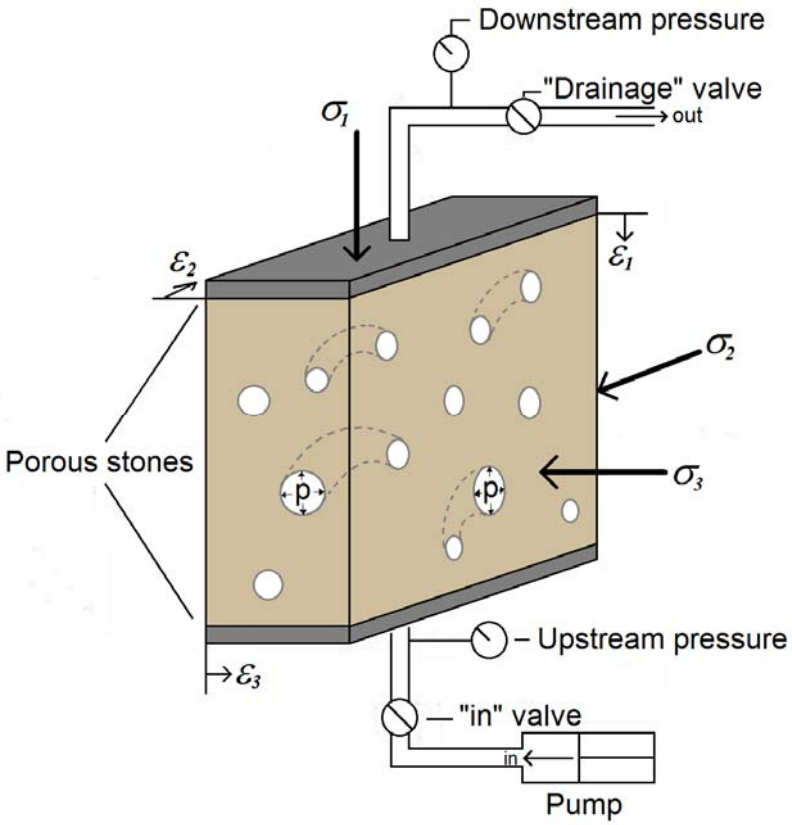

Figure 3.7: Principal stresses acting on the plane strain specimen and corresponding strains.

Increments of principal strains and stresses can be written as ($\varepsilon_2 = 0$):

$$\Delta\varepsilon_1 = \frac{1+\nu}{E}\left[(1-\nu)\Delta\sigma_1 - \nu\Delta\sigma_3\right]$$

$$\Delta\varepsilon_3 = \frac{1+\nu}{E}\left[(1-\nu)\Delta\sigma_3 - \nu\Delta\sigma_1\right] \tag{3.15}$$

$$\Delta\sigma_2 = \nu\left(\Delta\sigma_1 + \Delta\sigma_3\right)$$

Performing a test at constant confining pressure ($\Delta\sigma_3 = 0$) and taking the sign convention of compression positive, Young's modulus E and Poisson's ratio v are

$$E = \Delta\sigma_1 \frac{\Delta\varepsilon_1 - 2\Delta\varepsilon_3}{\left(\Delta\varepsilon_1 - \Delta\varepsilon_3\right)^2} \tag{3.16}$$

$$\nu = \frac{-\Delta\varepsilon_3}{\Delta\varepsilon_1 - \Delta\varepsilon_3} \tag{3.17}$$

For plane problems, it is convenient to introduce the invariants named (i) average stress s, (ii) shear stress t, (iii) volume strain ε, and (iv) shear strain γ:

$$s = \left(\sigma_1 + \sigma_3\right)/2 \tag{3.18}$$

$$t = \left(\sigma_1 - \sigma_3\right)/2 \tag{3.19}$$

$$\varepsilon = \varepsilon_1 + \varepsilon_3 \tag{3.20}$$

$$\gamma = \varepsilon_1 - \varepsilon_3 \tag{3.21}$$

This set of invariants satisfies the requirement of preserving the work increment dW constant while changing the coordinate system:

$$dW = \sigma_1 d\varepsilon_1 + \sigma_2 d\varepsilon_2 + \sigma_3 d\varepsilon_3 = s d\varepsilon + \pi d\gamma \tag{3.22}$$

Generalized Hooke's law for plane strain becomes

$$\Delta\varepsilon = \frac{2(1+\nu)}{3K}\Delta s \tag{3.23}$$

$$\Delta\gamma = \frac{1}{G}\Delta t \tag{3.24}$$

Drained bulk modulus K and shear modulus G are expressed as

$$K = \frac{E}{3(1-2\nu)} \tag{3.25}$$

$$G = \frac{E}{2(1+\nu)} \tag{3.26}$$

For undrained elastic behavior, undrained Young's modulus E_u and undrained Poisson's ratio ν_u are used. Then, generalized Hooke's law for undrained plane strain loading can be written in terms of equations (3.23) and (3.24), but for undrained elastic parameters:

$$\Delta\varepsilon = \frac{2(1+\nu_u)}{3K_u}\Delta s \tag{3.27}$$

$$\Delta\gamma = \frac{1}{G_u}\Delta t \tag{3.28}$$

where undrained bulk and shear moduli are

$$K_u = \frac{E_u}{3(1-2\nu_u)} \tag{3.29}$$

$$G_u = \frac{E_u}{2(1+\nu_u)} \tag{3.30}$$

In case of undrained testing, the pore pressure p must be considered and Terzaghi's effective stresses take the following form:

$$\sigma_1' = \sigma_1 - p \tag{3.31}$$

$$\sigma_3' = \sigma_3 - p \tag{3.32}$$

and in-plane effective mean and shear stresses become

$$s' = (\sigma_1' + \sigma_3')/2 \tag{3.33}$$

$$t' = (\sigma_1' - \sigma_3')/2 = (\sigma_1 - \sigma_3)/2 = t \tag{3.34}$$

Furthermore, because $\Delta t' = \Delta t$,

$$G_u = G \tag{3.35}$$

A drained test can be performed by maintaining the pore pressure in the specimen constant; this condition is applied and preserved by connecting the pore water lines to a microprocessor-based hydraulic pump that maintains water pressure at a constant value, within a tolerance of 0.02 MPa. By closing the inlet and drainage valves (Figure 3.7) and

thus keeping the mass of the fluid in the specimen constant, the undrained testing condition can be achieved.

Once v, E, v_u, and E_u are obtained from drained and undrained plane-strain tests, other parameters such as K, K_u, and G can be determined. Another parameter that can be measured under the undrained condition is the Skempton coefficient B. The detailed description of the saturation process and measurement of B is given in section 3.5.

Moreover, performing plane strain tests under drained conditions with $p = 0$ and assuming full saturation of the rock, such that the volume of the fluid in the pores is equal to the pore volume of the specimen, the volume of the fluid drained away from it during elastic deformation can be precisely measured. Thus, it is possible to calculate α as a ratio between the drained fluid volume ΔV_f and the change in specimen volume ΔV (Detournay and Cheng, 1993):

$$\alpha = \frac{\Delta V_f}{\Delta V} \tag{3.36}$$

Measurements of K then allow the calculation of the unjacketed bulk modulus K_s'.

Transversely isotropic parameters

Some of the transversely isotropic poroelastic material parameters can be measured using the plane strain configuration. Prismatic rock specimens are prepared in such a way that the axis of rotational symmetry is parallel to the direction of axial stress σ_1 (Figure 3.8).

If the cell pressure σ_3 is preserved constant, then application of only axial stress $\Delta\sigma_1$ induces intermediate principal stress $\Delta\sigma_2$ and corresponding strains take the form:

$$\Delta\varepsilon_1 = -\frac{\nu'}{E'}\Delta\sigma_2 + \frac{\Delta\sigma_1}{E'} \tag{3.37}$$

$$\Delta\varepsilon_2 = 0 = \frac{\Delta\sigma_2}{E} - \frac{\nu'}{E'}\Delta\sigma_1 \tag{3.38}$$

$$\Delta\varepsilon_3 = -\frac{\nu}{E}\Delta\sigma_2 - \frac{\nu'}{E'}\Delta\sigma_1 \tag{3.39}$$

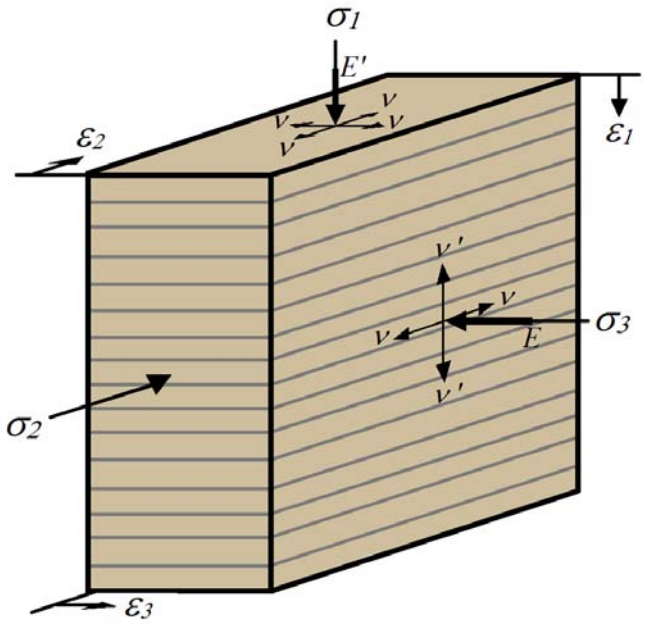

Figure 3.8: Transversely isotropic parameters in the plane strain configuration.

Then $\Delta\sigma_2$ is calculated to be

$$\Delta\sigma_2 = \frac{\nu' E}{E'}\Delta\sigma_1 \tag{3.40}$$

and the following relationships are written for the increments of ε_1, ε_3, and σ_1:

$$\frac{\Delta\varepsilon_1}{\Delta\sigma_1} = \left(\frac{1}{E'} - \frac{\nu'^2}{E'^2}E\right) \tag{3.41}$$

$$\frac{\Delta\varepsilon_3}{\Delta\sigma_1} = -\frac{\nu'}{E'}(1+\nu) \tag{3.42}$$

Similarly, if the axial stress σ_1 is preserved constant, then application of only cell pressure $\Delta\sigma_3$ induces intermediate principal stress $\Delta\sigma_2$ and corresponding strains take the form:

$$\Delta\varepsilon_1 = -\frac{\nu'}{E'}\Delta\sigma_3 - \frac{\nu'}{E'}\Delta\sigma_2 \tag{3.43}$$

$$\Delta\varepsilon_2 = 0 = -\frac{\nu}{E}\Delta\sigma_3 + \frac{\Delta\sigma_2}{E} \tag{3.44}$$

$$\Delta\varepsilon_3 = \frac{\Delta\sigma_3}{E'} - \frac{\nu}{E}\Delta\sigma_2 \tag{3.45}$$

and the following equalities hold for the increments of ε_1, ε_3, and σ_1:

$$\frac{\Delta\varepsilon_1}{\Delta\sigma_3} = -\frac{\nu'}{E'}(1+\nu) \tag{3.46}$$

$$\frac{\Delta\varepsilon_3}{\Delta\sigma_3} = \frac{(1-\nu)(1+\nu)}{E} \tag{3.47}$$

Hence, by measuring increments of axial and lateral strains while applying separately axial and lateral load to the prismatic specimens, the right hand sides of equations (3.41), (3.42), (3.46), and (3.47) can be measured.

3.4 Conventional triaxial compression

3.4.1 Triaxial testing apparatus

Another geometry, which allows direct measurements of applied principal stresses and corresponding strains, is a cylindrical specimen tested in conventional triaxial (axisymmetric) compression. To conduct axisymmetric compression experiments on fluid-saturated rock specimens, the plane-strain apparatus was modified (Figure 3.9), which allowed testing of a cylindrical specimen (1) (h =104 mm, d = 51 mm), in the chamber filled with hydraulic oil. The axial load is controlled by the movement of the piston (2) and measured by the confining pressure-compensated load cell (4). Axial and tangential strains are measured by the two pairs of strain gages (3); axial displacement is also measured by a pair of LVDTs (5). AE sensors (6) are used to monitor the microseismic activity in the specimen, and the pore pressure is applied and monitored both upstream and downstream (7) by two pressure transducers.

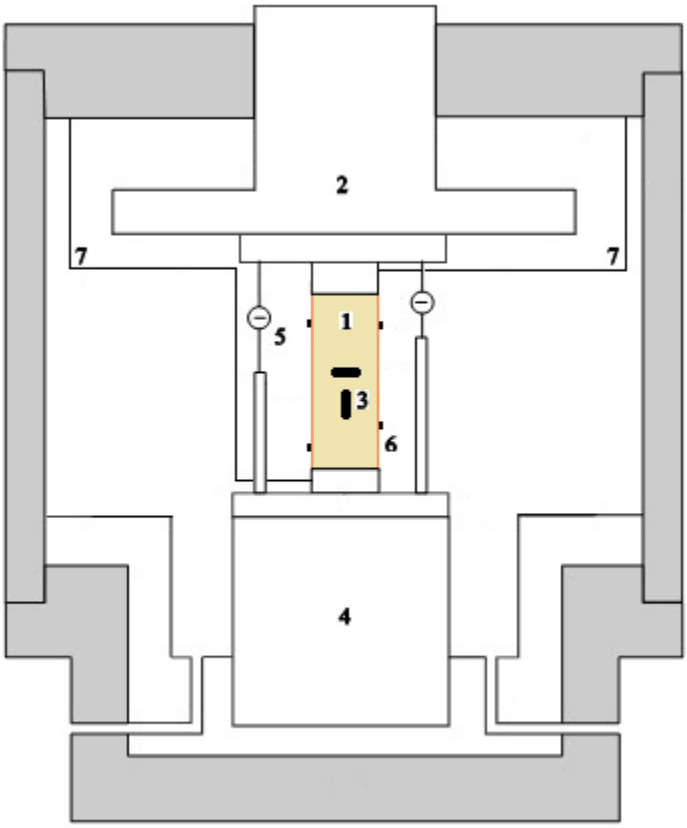

Figure 3.9: Apparatus for conventional triaxial testing of fluid-saturated rock.

The ends of cylindrical specimens were ground so that they were parallel to each other and perpendicular to the main axis within ±0.01 mm in 104 mm. The specimen (Figure 3.10) is assembled with porous stones between the upper and lower steel platens; two small (4 mm diameter) circular brass buttons 1 mm thick were glued to the specimen to provide firm contact for the probes of the AE sensors. The specimen, porous stones, and platens were held together and "rotated," such that a thin and uniform layer of polyurethane was achieved to seal the specimen and prevent confining fluid from penetrating the rock.

Figure 3.10: Cylindrical specimen with glued strain gages, AE sensors and LVDTs.

Additionally, a relatively simple apparatus can be used for conventional triaxial tests on dry specimens. Franklin and Hoek (1970) suggested the design of the cell (Figure 3.11), where a cylindrical specimen (1) is put inside the rubber membrane (2) and subjected to the axial load through steel platens (4), and hydraulic pressure is applied by confining liquid filling the chamber (3).

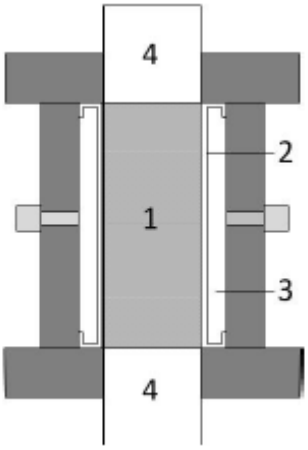

Figure 3.11: Hoek-Franklin cell for conventional triaxial testing (Meyer 2012).

3.4.2 Constitutive relationships in conventional triaxial compression

Isotropic parameters

In conventional triaxial compression, the major principal stress $\sigma_1 = \sigma_z$ is applied axially while the intermediate and minimum principal stresses are applied in the radial direction by the confining fluid; thus $\sigma_2 = \sigma_3 = \sigma_r$ and σ_3 is called the cell pressure. Axial strain ε_1 can be measured by strain gages $\varepsilon_l = \varepsilon_{axial}$ and LVDTs, tangential and radial strains ε_θ and ε_r are equal to each other and are measured by lateral strain gages: $\varepsilon_\theta = \varepsilon_r = \varepsilon_2 = \varepsilon_3 = \varepsilon_{lateral}$ (Figure 3.12).

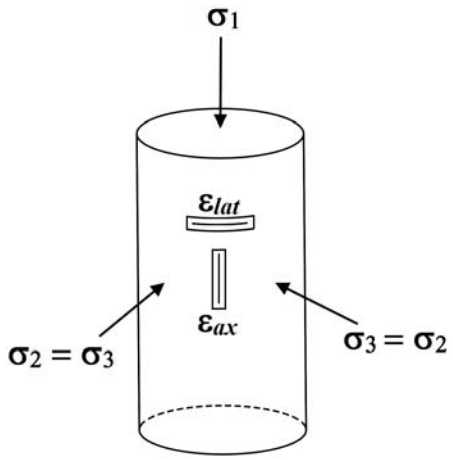

Figure 3.12: Principal stresses and measured strains in the conventional triaxial compression test.

For this geometry, the following invariants can be considered: mean stress P, shear stress t, volume strain ε_v, and shear strain ε_s:

$$P = (\sigma_1 + 2\sigma_3)/3 \tag{3.48}$$

$$t = (\sigma_1 - \sigma_3)/2 \tag{3.49}$$

$$\varepsilon_v = \varepsilon_1 + 2\varepsilon_3 \tag{3.50}$$

$$\varepsilon_s = 4(\varepsilon_1 - \varepsilon_3)/3 \tag{3.51}$$

Note that here the shear strain ε_s is chosen such that this set of invariants satisfies the requirement of preserving the work increment constant (equation 3.22).

Because application and measurement of the three principal stresses and corresponding strains is straightforward in conventional triaxial compression, unjacketed test can be conducted by applying increments of pore pressure equal to the increments in the mean stress: $\Delta p = \Delta P$. Drained and undrained compression are performed by preserving the same boundary conditions as in plane strain compression. The bulk moduli related to these three limiting states, *i.e.* unjacketed K_s', drained K, and undrained K_u, can be measured by applying hydrostatic loading to the cylindrical specimens and recording the corresponding volume strain. If axial and cell pressures are applied separately, drained and undrained Young's moduli and Poisson's ratios can also be measured.

Measurements of K_s' and K allow the calculation of Biot coefficient α from equation (2.31). The detailed description of the measurement of the Skempton coefficient B under axisymmetric loading is given in section 3.5. It will be shown in section 4.5 that measurement of the aforementioned isotropic poroelastic parameters is sufficient for the calculation of effective bulk modulus K_{eff}, which plays a role in the characterization of the inelastic response of fluid-saturated rock.

Transversely isotropic poroelastic parameters

By applying axial (parallel to the axis of symmetry) and lateral stress to cylindrical specimens independently and measuring the corresponding strains, some of the transversely isotropic poroelastic parameters can be calculated (Figure 3.13).

Application of the stress increment only in the radial direction $\Delta\sigma_r$ leads to the following relationships for measured strains ($\Delta\sigma_\theta = 0$):

$$\frac{\Delta\varepsilon_\theta}{\Delta\sigma_r} = -\frac{\nu}{E} \tag{3.52}$$

$$\frac{\Delta\varepsilon_z}{\Delta\sigma_r} = -\frac{\nu'}{E'} \tag{3.53}$$

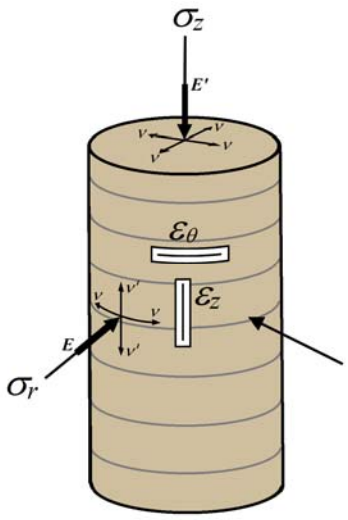

Figure 3.13: Transversely isotropic parameters in conventional triaxial testing.

If the increment in the stress is applied only in the axial direction $\Delta\sigma_z$, then the measured strains take the form:

$$\frac{\Delta\varepsilon_z}{\Delta\sigma_z} = \frac{1}{E'} \tag{3.54}$$

$$\frac{\Delta\varepsilon_\theta}{\Delta\sigma_z} = -\frac{\nu'}{E'} \tag{3.55}$$

Hence, the independent application of axial stress and confining pressure in the axisymmetric configuration allows the determination of the following quantities: E', ν', and ν/E.

Combining the results of conventional triaxial and plane strain compression, the four parameters E, E', ν, and ν' can be determined from equations (3.46), (3.47), (3.54) and (3.55). Hence, using equations (2.64) – (2.67), all transversely isotropic parameters can be computed from drained and undrained response, but not G', the shear modulus normal to the plane of isotropy. Determination of G' would require, for example, application of a shear stress σ_{zr} and it cannot be achieved by either the plane strain or axisymmetric configuration. Consequently, seven of the eight independent parameters governing

transversely isotropic poroelastic response of fluid-saturated material can be measured or calculated.

3.5 Saturation and *B*-check

3.5.1 Skempton coefficient

For undrained triaxial tests on soil, Skempton (1954) introduced the pore-pressure coefficient B to express the pore pressure change Δp that occurs due to a change in the hydrostatic pressure ΔP. For soil with porosity ϕ,

$$B = \frac{\Delta p}{\Delta P} = \frac{1}{1 + \frac{\phi K}{K_f}} \tag{3.56}$$

and since the bulk modulus of a soil structure K (order of MPa) is negligible with respect to that of the fluid K_f (order of GPa), $B \approx 1.0$ for soft soil. While saturating soft or medium stiff soil, B is increasing until it becomes equal to 1.0, meaning that all load is taken by the pore fluid and the specimen is fully saturated. However, for rock, K is on the order of GPa and it is comparable to the bulk modulus of the saturating fluid, such as water (K_w = 2.24 GPa) or hydraulic oil (K_{oil} = 1.3 GPa). It means that rock's stiff framework feels the applied mean stress at least as much as the pore fluid; hence the Skempton coefficient for rock can be significantly smaller than one. A number of experimental studies (Mesri *et al.* 1976; Green and Wang 1986; Blöcher *et al.* 2007; Hart and Wang 2010) suggests that B is decreasing with the effective mean stress and could be as low as 0.3 for sandstones, even at full saturation.

Bishop (1973) extended Skempton's relation (3.56) to include the influence of the bulk modulus of the solid material of the skeleton (or unjacketed bulk modulus) K_s' for any porous mass with interconnected pores. The skeleton and solid material were considered to be elastic and isotropic, and the pore fluid was linearly compressible. B is measured under undrained condition ($\zeta = 0$) and in terms of bulk moduli can be written as

$$B = \left.\frac{\Delta p}{\Delta P}\right|_{\zeta=0} = \frac{\alpha}{\alpha + \phi K\left(\frac{1}{K_f} - \frac{1}{K_s''}\right)} \tag{3.57}$$

Because of the relationships (2.16) and (2.22), B should be always non-negative:

$$0 \le B \le 1 \tag{3.58}$$

Measuring K, K_u, and α experimentally and independently of B, the latter can be calculated from equation (2.22) and compared to the measured B.

3.5.2 Saturation

The degree of saturation S, $0 \le S \le 1$, is determined as

$$S = V_f / V_\phi \tag{3.59}$$

where V_f is the volume of the pore fluid (liquid) in the pores. If the specimen is saturated with water, then the pore fluid in the nearly saturated ($S > 0.95$) soil or rock is a mixture of water and gas that has a fluid bulk modulus K_f. Several studies (Verruijt 1969; Allen *et al*. 1980; Vardoulakis and Beskos 1986) describe the relationship between the fluid bulk modulus K_f and the degree of saturation. However, if $S > 0.98$, then the approximate relationship suggested by Verruijt (1969) is applicable:

$$\frac{1}{K_f} = \frac{1}{K_w} + \frac{1 - S}{p} \tag{3.60}$$

Equation (3.60) shows that even a small variation in the degree of saturation strongly influences the bulk modulus of the fluid and hence B, as indicated by equation (3.57).

For soil, simple injection of water into the specimen at low back pressure (order of 0.1 MPa) provides $S \sim 0.98$ (Black and Lee 1973). However, further increase of S to 1.00 is an involved process. Schuurman (1966) suggested that for $S > 0.85$, the pore air is presented as individual bubbles rather than as a continuous phase. Pressures at which air bubbles in the water approach a critical value and collapse are relatively small (order of 0.1 MPa). However, time to fully dissolve all the air trapped in the pores and drainage lines can be on the order of weeks (Schuurman 1966; Black and Lee 1973). It happens

because surface areas of the bubbles and volumes of liquid where they can dissolve are much smaller than in a large water reservoir; hence the diffusion of the pore air in the pore water becomes a very time consuming procedure (Lee and Black 1972). To facilitate this process, Black and Lee (1973) suggested initial flushing of the specimen with deaired water and further gradual application of the back pressure in the pore lines that is significantly greater than the theoretical critical pressure for air bubble collapse.

The purpose of back pressure technique is to achieve 100% saturation by forcing any gas into solution of the pore water. Increase of the pore pressure in a partially saturated specimen affects the volume of the gas in the pores in two ways: (1) by direct compression, the gas is reduced in volume according to Boyle's law; (2) by application of a higher pressure, additional amounts of gas are dissolved in the pore water in accordance with Henry's law of solubility (Lowe and Johnson 1960).

Wissa (1969) suggested a method to check if a very stiff soil specimen is fully saturated by determining Skempton coefficient B at gradually increasing back pressures while keeping the effective mean stress approximately constant. If the rock is not fully saturated, then the B-value will be increasing with increasing pressure, as more air is forced into solution. A measured B-value that is constant and independent of the magnitude of the back pressure indicates full saturation.

Once the air is driven into solution, the air-water mixture behaves as a fluid with a bulk modulus equal to that of pure water (Schuurman 1966; Fredlund 1976), so dissolved air in the water has no influence on K_f. Hence, pore fluid bulk modulus becomes a fixed parameter and can be used in calculation of some other poroelastic moduli presented in equations (3.57) and (2.34).

Application of high back pressures (> 10 MPa) can be limited by the pore pressure system. Also, sometimes it could be necessary to duplicate the field conditions, where the pore fluid pressure *in-situ* is on the order of a few MPa. In the next section, the experimental method of achieving and assuring full saturation with minimum back pressure is presented.

3.5.3 Experimental technique

Saturation of plane strain specimens

After the rock specimen was prepared, connected to the pore pressure system, and placed inside the plane-strain apparatus, a small axial seating load was applied. Then, the specimen was stressed axially and laterally (by cell pressure) to 5 – 7 MPa, depending on the pore pressured to be applied later in the test. Once the desired mean stress was achieved, the process of water saturation of the specimen started. Deaired water was pumped from downstream into the specimen with the upstream valve open to the atmosphere, releasing excess air as the pore water permeated through the specimen (Figure 3.7). For each step of water injection (5 – 10 ml/step), the upstream pressure increased to approximately 0.3 MPa and decreased in a minute or so to about 0.1 MPa before the next step of injection. The water started flowing from the upstream valve after injecting about 80 ml, the estimated volume of pore space in the specimen. Further pumping of 100 ml of water through the specimen showed that a mass balance was approximately achieved.

The technique of back-pressure saturation was used next. Pore pressure p was increased in the specimen by pumping water in and having the drainage valve closed; a maximum back pressure of p = 5 – 6 MPa was applied. During this procedure, the axial and lateral stresses were always kept approximately 5 MPa higher than the pore pressure. After each new increase in back pressure, the pore pressure was allowed to equilibrate, meaning that upstream pressure would be equal to the downstream pressure and the change in pressure would not exceed 1 kPa/min. During this process, the remaining gas was dissolved into the pore fluid. When equilibrium of pressure was achieved, Skempton coefficient was measured through a procedure called a B-check.

The B-check is not straightforward under a plane strain condition, because the intermediate principal stress is not measured directly, but calculated with the knowledge of elastic parameters (equation 3.14). The specimen size was chosen so that when equal increments in axial stress $\Delta\sigma_1$ and cell pressure $\Delta\sigma_3$ were applied, the frame deformation due to the stress increment applied by the specimen was compensated by the negative

strain on the inner side of the frame due to the increase in cell pressure; according to Lame's solution, the inner part compresses due to equal pressures applied on the inside and outside of the cylinder. So, $\Delta\varepsilon_2 = 0$ in equation (3.14) and the expression for the measured B takes the form

$$B^{meas} = \frac{\Delta p}{\Delta P} = \frac{3\Delta p}{(1+\tilde{\nu})(\Delta\sigma_1 + \Delta\sigma_3)} \tag{3.61}$$

where $\tilde{\nu}$ is the current Poisson's ratio of the rock and it changes from ν in dry (or drained) condition to ν_u upon saturation, while $\nu_u > \nu$. When the undrained elastic loading performed on the saturated specimen, ν_u independent of B-values can be calculated from the plane strain compression data.

While performing an undrained test in the laboratory, the specimen is connected to the drainage system of the cell and also to the pore pressure transducers. As the drainage system has a non-zero volume filled with water, it experiences volume changes due to its compressibility. Wissa (1969) and Bishop (1976) modified the expression for B to include terms representing the compressibility of the pore-pressure measuring system. The following equation was obtained for the "corrected" value of the Skempton coefficient B^{cor}:

$$B^{cor} = \frac{1}{\dfrac{1}{\left(\dfrac{\Delta p}{\Delta P}\right)_{observed}} - \dfrac{V_L}{V}\dfrac{K}{\alpha K_f} - \dfrac{K(C_L + C_M)}{\alpha V}} \tag{3.62}$$

where V is the volume of the specimen, V_L is the volume of the fluid in the pore-water lines, C_L is the compressibility of the pore-water lines, and C_M is the compressibility of the pore-pressure measuring element. However, several researchers (Mesri *et al.* 1976; Bishop 1976; Ghabezloo and Sulem 2009) noticed that for modern high-pressure tubes and pressure transducers, the main contribution (more than 95%) to the correction term comes from the extra fluid volume in the system V_L. So, only the first two terms in the denominator of the right hand side of (3.62) are considered. The final equation for calculating B^{cor} in plane strain experiments is

$$B^{cor} = \frac{1}{\left(\frac{(1+\tilde{\nu})(\Delta\sigma_1 + \Delta\sigma_3)}{3\Delta p}\right) - \frac{V_L}{V}\frac{K}{\alpha K_f}} \tag{3.63}$$

During the back-pressure saturation procedure, several immediate increments of $\Delta\sigma_1 = \Delta\sigma_3 = 0.34$ MPa were applied and the corresponding increase in pore-water pressure Δp was measured in a few minutes when p equilibrated. If the system is completely saturated, the pore pressure response should be constant and independent of back pressure. On the other hand, if the system is not saturated, the pore pressure response will increase with growing back pressure, because the degree of saturation is augmented and consequently, the bulk modulus of the pore fluid increases according to equation (3.59) as the back pressure is growing (Wissa 1969). If this is the case, the new increment in back pressure is applied and equilibrium is established before performing a new *B*-check. When Δp becomes the same for each increment $\Delta\sigma_1 = \Delta\sigma_3 = \text{const}$, the rock is considered to be saturated.

Saturation of cylindrical specimens

The technique, similar to the plane strain test procedure, is applied for saturation of cylindrical specimens tested in conventional triaxial compression. The Skempton coefficient B is calculated from measurements of pore pressure increase Δp due to application of hydrostatic mean stress $\Delta P = \Delta\sigma_1 = \Delta\sigma_3$ and correcting for the extra fluid volume in the drainage system:

$$B^{cor} = \frac{1}{\left(\frac{(\Delta\sigma_1 + 2\Delta\sigma_3)}{3\Delta p}\right) - \frac{V_L}{V}\frac{K}{\alpha K_f}} \tag{3.64}$$

Additionally, two transversely isotropic Skempton coefficients were measured: B' due to application of $\Delta\sigma_1$ only ($\Delta\sigma_3 = 0$) and B as the result of independent application of $\Delta\sigma_3$:

$$B' = \frac{1}{\left(\frac{\Delta\sigma_1}{3\Delta p}\right) - \frac{V_L}{V}\frac{K}{\alpha K_f}} \tag{3.65}$$

$$B = \frac{1}{\left(\frac{2\Delta\sigma_3}{3\Delta p}\right) - \frac{V_L}{V}\frac{K}{\alpha K_f}} \tag{3.66}$$

Moreover, Skempton coefficient A (equation 2.46) was measured by applying a specific deviatoric loading on the cylindrical specimen: $\Delta\sigma_1 = -2\Delta\sigma_3$. In this case, the mean stress P is preserved constant and A^{cor}, Skempton A coefficient corrected for the presence of extra fluid volume in the measuring system, can be calculated as

$$A^{cor} = \frac{1}{3} + \frac{1/B^{cor}}{\left(\frac{\Delta\sigma_1 - \Delta\sigma_3}{\Delta p}\right) - \frac{V_L}{V}\frac{K}{\alpha K_f}} \tag{3.67}$$

Saturation of specimens tested in hydrostatic compression

For unjacketed hydrostatic compression, the specimens were subjected to a high cell pressure (10 – 12 MPa), which was kept for a few hours to provide full saturation. The unjacketed response (section 4.3.1) shows that this technique guaranteed satisfactory results.

3.6 Acoustic emission technique

3.6.1 AE rate and locations

Two categories of laboratory AE studies are considered. The first category is a simple counting of the number of AE events prior to and after specimen failure. AE rate can then be correlated with inelastic strain rate. The second area involves the location of the AE source. By recording the time histories and identifying the arrival time of the P-wave, it is possible to locate the event with an error of a few millimeters. Two assumptions are often used to simplify the problem: (i) the event is simulated as a point source of displacement discontinuity referred to as a microcrack and (ii) the elastic wave propagation is through a homogeneous, isotropic medium.

A common type of source location algorithm involves the arrival time of the P-wave. Microseismic activity due to a change in stress or environment is recorded by each sensor

with a known position at a given time. From the relative arrival times of the P-wave and the measured P-wave velocity of the material, the event hypocenter can be estimated with a minimum of five sensors. The problem contains four unknowns: the spatial coordinates *x, y, z* of the event and the time *t* at which the event occurred, but a fifth sensor (or other information) is needed to remove ambiguities arising from the quadratic nature of the distance equation. Because some error is associated with arrival-time detection and with the P-wave velocity (as damage accumulates, material properties may change or become anisotropic), the number of sensors should be increased so that the location problem becomes over-determined. Then a solution scheme can be developed whereby the error is minimized to obtain a best-fit type of solution, and statistical methods can be used to evaluate the goodness of the fit.

The distance r_i between the source and the i^{th} sensor is related to the P-wave velocity c_p by

$$r_i = c_p\left(t_i - t\right) + e_i \tag{3.68}$$

where t_i = arrival time at the i^{th} sensor, and e_i = residual of computed distances. A time shift does not affect the source location, so an arbitrary time base can be selected. The travel distance r_i can be expressed by the unknown source coordinates (x, y, z) and the known sensor coordinates (x_i, y_i, z_i) by

$$r_i = \sqrt{\left(x_i - x\right)^2 + \left(y_i - y\right)^2 + \left(z_i - z\right)^2} \tag{3.69}$$

The sum of the squares of the residuals e_i can be written (N = the number of sensors)

$$I = \sum_{i=1}^{N} e_i^2 \tag{3.70}$$

The unknowns *x, y, z* and *t* can be determined using a least-squares method by minimizing *I*. However, the equations are nonlinear in the source coordinates *x, y, z*, so the minimization is carried out numerically using the Levenberg-Marquardt algorithm. The first estimate of *x, y, z* is obtained by a linearization of (3.70).

3.6.2 AE system

The AE system used in experiments is composed of (i) an array of AE sensors; (ii) signal conditioners and preamplifiers; (iii) signal digitizer; and (iv) computer based data acquisition system. Eight AE sensors (Physical Acoustics model S9225, frequency response from 0.3 – 1.8 MHz) are attached with cyanoacrylate adhesive to the small brass tabs on the specimen surface. AE signals are preamplified (Physical Acoustics S1220C), with 40 dB gain and a built-in 0.1 – 1.2 MHz band-pass filter. Typical noise level at the output of the preamplifiers is around ± 2 mV. The high-speed AE data acquisition system records waveforms and it is composed of four modular transient recorders (LeCroy model 6840), with two channels each, 8-bit analog-to-digital (ADC) resolution and a 20 MHz sampling rate (50 nanoseconds between points) over a 100 μs window, with a 50 μs pretrigger. The LeCroy 6010 controller, with a built-in 10 MHz microprocessor (Motorola 68020), communicates to a 486-processor microcomputer through National Instrument AT-GPIB card and cable. AE data are transferred to the host computer after every 128 kbytes of digitizer memory is filled (equivalent to 64 events). A downloading time of approximately 4 seconds is required before the system memory is ready for the next incoming AE events. All recording is triggered when the signal amplitude exceeds a certain threshold (±7 mV) on the first sensor. The threshold of amplitude must be set so that environmental noise does not trigger the system, but the threshold should not be set too high as to exclude signals of low amplitude.

3.7 Summary of experimental methods

The description of the performed tests in terms of boundary conditions and measured and calculated isotropic poroelastic parameters is presented in Table 3.1. The measurements related to the calculation of drained and undrained transversely isotropic poroelastic parameters are summarized in Table 3.2. Methods for determining the parameters related to the description of inelastic behavior of fluid-saturated rock under drained and undrained conditions are described in section 4.5.

Table 3.1: Summary of isotropic poroelastic measurements.

Boundary conditions	Test type	Measurements	Parameters
Dry: $p = 0$	Hydrostatic	ΔP, $\Delta\varepsilon$	K
	Plane strain	$\Delta\sigma_1$, $\Delta\sigma_3$, $\Delta\varepsilon_1$, $\Delta\varepsilon_3$	E, ν, K, G
Drained: $\Delta p = 0$	Plane strain	$\Delta\sigma_1$, $\Delta\sigma_3$, $\Delta\varepsilon_1$, $\Delta\varepsilon_3$, ΔV_f	E, ν, K, G, α
	Conv traixial	$\Delta\sigma_z$, $\Delta\sigma_r$, $\Delta\varepsilon_z$, $\Delta\varepsilon_r$	E, ν, K, G
Undrained: $\Delta\zeta = 0$	Plane strain	$\Delta\sigma_1$, $\Delta\sigma_3$, $\Delta\varepsilon_1$, $\Delta\varepsilon_3$, Δp	E_u, ν_u, K_u, B
	Conv triaxial	$\Delta\sigma_z$, $\Delta\sigma_r$, $\Delta\varepsilon_z$, $\Delta\varepsilon_\theta$, Δp	E_u, ν_u, K_u, B, A
Unjacketed: $\Delta p = \Delta P$	Hydrostatic	ΔP, $\Delta\varepsilon$	K_s'
	Conv triaxial	ΔP, $\Delta\varepsilon$	K_s'

Table 3.2: Summary of transversely isotropic poroelastic measurements

Boundary conditions	Test type	Measurements	Parameters
Drained: $\Delta p = 0$	Plane strain	$\Delta\sigma_1$, $\Delta\sigma_3$, $\Delta\varepsilon_1$, $\Delta\varepsilon_3$	$\frac{\nu'}{E'}(1+\nu)$, $\frac{(1-\nu)(1+\nu)}{E}$
	Conv triaxial	$\Delta\sigma_z$, $\Delta\sigma_r$, $\Delta\varepsilon_z$, $\Delta\varepsilon_r$	$\frac{\nu}{E}$, E', ν'
Undrained: $\Delta\zeta = 0$	Plane strain	$\Delta\sigma_1$, $\Delta\sigma_3$, $\Delta\varepsilon_1$, $\Delta\varepsilon_3$, Δp	$\frac{\nu_u'}{E_u'}(1+\nu_u)$, $\frac{(1-\nu_u)(1+\nu_u)}{E_u}$
	Conv triaxial	$\Delta\sigma_z$, $\Delta\sigma_r$, $\Delta\varepsilon_z$, $\Delta\varepsilon_r$, Δp	$\frac{\nu_u}{E_u}$, E_u', ν_u', B, B'

Chapter 4

Results and Discussion

4.1 Berea sandstone

4.1.1 Dry properties

Berea sandstone was selected for the rock-fluid interaction experiments, as data for this material is available from different experiments previously performed on the dry rock in the UMN Rock Mechanics Laboratory (*e.g.* Riedel and Labuz 2007; Dehler and Labuz 2007) and from poroelastic studies (Rice and Cleary 1976; Green and Wang 1995; Zimmerman 1991; Lockner and Stanchits 2002; Hart and Wang 2010). The sandstone found in Berea, Ohio was formerly quarried for construction and now is frequently used for core analysis (Dullien 1992). Manufacturer reports that the sandstone is composed of 93% silica, 4% alumina, plus other trace elements. According to the petrographic analysis performed by American Engineering Testing (St. Paul, MN), the tested rock is a fine-grained (0.12 – 0.25 mm), well-compacted, well sorted, cross-bedded sandstone comprised chiefly (~ 90% of solid volume) of sub-rounded to rounded quartz grains (Figure 4.1). The other minerals that are present include potassium feldspar (~ 7%), calcite (~ 1%), ferric oxides (~ 0.5%), and traces of plagioclase, hornblende, pyroxene, muscovite, weathered clays, and zircon. Cementation of the sandstone occurs mainly as interstitial microquartz and syntaxial quartz overgrowths. The rock is light gray with closely spaced (~ 5 mm) planar bedding surfaces clearly demarked by laminations of rust-red iron oxides.

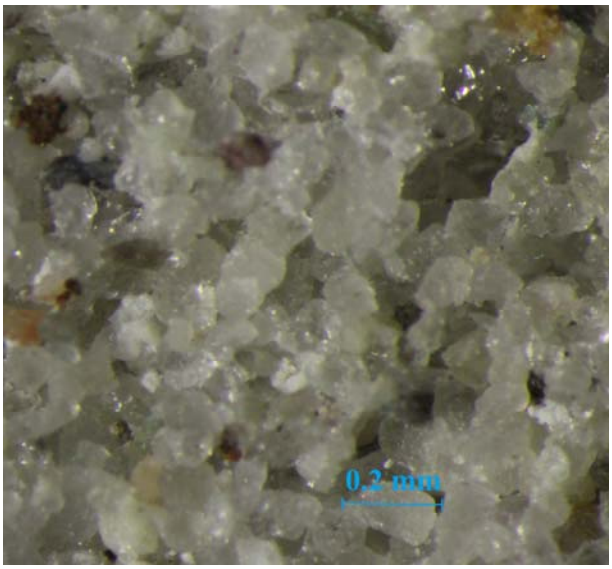

Figure 4.1: Microphotograph of Berea sandstone sample.

A single block, 305 x 305 x 245 mm (*x, y, z*-axes) with density ρ = 2100 kg/m^3 was used to fabricate all specimens. Ultrasonic velocity measurements show that rock has a low level of anisotropy: P-wave and S-wave velocities (c_p [km/s], c_s [km/s]) in *x*, *y*, and *z*-directions were measured to be (2.12, 1.41), (2.11, 1.36), and (1.98, 1.34), so there is 6-7 % difference in the velocities measured in different directions. Also, uniaxial compressive strength (UCS) tests were performed on six right cylindrical specimens (h = 105 mm, d = 50 mm), prepared in accordance with ISRM standards (Brown 1981) and loaded at an axial displacement rate of 5 x 10^{-4} mm/s. Axial and tangential strains were monitored by foil strain gages attached to one side of a specimen to determine Young's modulus E and Poisson's ratio v. Additionally, an opposite side was ground and painted, so that the digital image correlation (DIC) technique could be used for calculation of the displacement field (Lin *et al.* 2010). The UCS measured in the direction perpendicular to the bedding planes was found to be 41-43 MPa, which is 7 – 8% larger than the one along the beds. Young's modulus and Poisson's ratio measured by strain strain gages and calculated by DIC method were found to be consistent and equal to E = 14 – 15 GPa and ν = 0.31 (Figure 4.2).

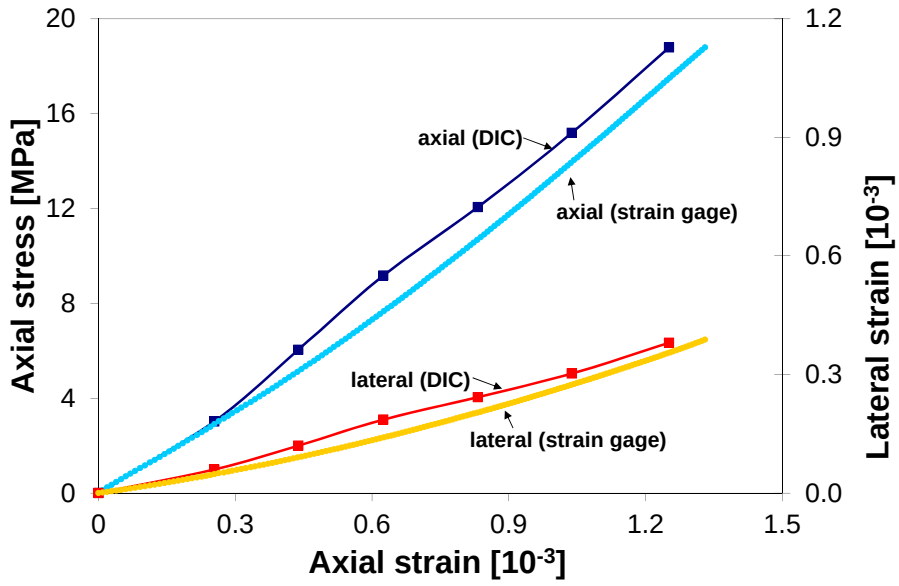

Figure 4.2: Strain gage and DIC data from uniaxial compression test on Berea sandstone.

4.1.2 Failure criteria

For the characterization of the failure response, ten conventional triaxial tests and five plane strain compression tests were conducted on dry Berea sandstone specimens such that the axial load was applied in the direction perpendicular to the bedding planes. Paul-Mohr-Coulomb (PMC) failure criterion is linear with three principal stresses (Paul 1968) $A\sigma_1 + B\sigma_2 + C\sigma_3 = 1$, where $A = (1 - sin\varphi_c)/(2V_o sin\varphi_c)$, $B = (sin\varphi_c - sin\varphi_e)/(2V_o sin\varphi_c)$, $C = -(1 + sin\varphi_e)/(2V_o sin\varphi_e)$, which takes into account an intermediate stress effect. Three material parameters: friction angles in compression, φ_c, and extension, φ_e, and the uniform triaxial tensile strength, V_o, can be identified from conventional triaxial compression and extension experiments and are sufficient to define a six-sided failure surface (Meyer and Labuz 2013).

All specimens were prepared in accordance with ISRM standards (Brown 1981) and loaded at an axial displacement rate of 5 x 10^{-4} mm/s. Of the ten triaxial tests, five were performed in compression with $\sigma_1 = \sigma_{axial}$ and $\sigma_2 = \sigma_3 = \sigma_{radial}$, and five in extension with $\sigma_1 = \sigma_2 = \sigma_{radial}$ and $\sigma_3 = \sigma_{axial}$. The compression tests are conducted as loading tests, where σ_{axial} is increased ($\Delta\sigma_{axial} > 0$) from $\sigma_{axial} = \sigma_{radial}$ until failure and $\sigma_{radial} =$

constant. The remaining five triaxial specimens are tested in extension unloading, with σ_{axial} decreasing ($\Delta\sigma_{axial} < 0$) from $\sigma_{axial} = \sigma_{radial}$ until failure and σ_{radial} = constant. The results from the triaxial compression and extension experiments, as well as the results of plane strain compression tests, are presented in Table 4.1.

Table 4.1: Principal stresses at failure for plane strain compression and conventional triaxial compression and extension experiments.

Test name	σ_1 [MPa]	σ_2 [MPa]	σ_3 [MPa]
BXBS-1	96.9	42.3	8.0
BXBS-5	58.7	24.2	0.0
BXBS-7	95.6	40.9	6.0
BXBS-9	45.3	15.3	0.0
BXBS-10	82.1	33.1	5.0
Triax-comp-1	93.3	5.0	5.0
Triax-comp-2	114.0	10.0	10.0
Triax-comp-3	138.6	20.0	20.0
Triax-comp-4	197.2	30.0	30.0
Triax-comp-5	229.3	40.0	40.0
Triax-ext-6	62.0	62.0	2.24
Triax-ext-7	60.0	60.0	1.79
Triax-ext-8	57.0	57.0	1.56
Triax-ext-9	51.0	51.0	2.1
Triax-ext-10	48.0	48.0	1.48

For the axisymmetric stress state in conventional triaxial testing, stress invariants P and q can be introduced:

$$P = \frac{\sigma_1 + \sigma_2 + \sigma_3}{3} = \frac{\sigma_{axial} + 2\sigma_{radial}}{3} \tag{4.1}$$

$$q = \sqrt{3J_2} = \sigma_{axial} - \sigma_{radial} \tag{4.2}$$

where J_2 is the second invariant of the stress deviator $s_{ij} = \sigma_{ij} - P\delta_{ij}$. The value of q is positive for triaxial compression, $\sigma_{axial} > \sigma_{radial}$, and negative in triaxial extension, $\sigma_{axial} < \sigma_{radial}$.

The linear failure criterion in compression in terms of P and q for conventional triaxial testing can be written as

$$q = \frac{6\sin\varphi_c}{3 - \sin\varphi_c} P + \frac{6c_c\cos\varphi_c}{3 - \sin\varphi_c} \tag{4.3}$$

The extension line can be given in a similar manner:

$$q = -\frac{6\sin\varphi_e}{3 - \sin\varphi_e} P - \frac{6c_e\cos\varphi_e}{3 - \sin\varphi_e} \tag{4.4}$$

where c_c and c_e are the cohesion measured in compression and extension respectively.

The compression and extension data must be fitted by adding a constraint so that the lines intersect the P-axis at the same point V_o, which is required for any failure surface. The corresponding lines of best fit with a common vertex to a data set from compression and extension testing are determined by finding the maximum value of the sum of the correlation coefficients ($R_c^2 + R_e^2$), under the condition that absolute value of the difference $\left| R_c^2 - R_e^2 \right|$ is a minimum (Meyer and Labuz 2013). This approach forces the vertex away from the original P-intercepts obtained from the lines of least-squares fit. The data and the best fit lines with the constraint of the same V_o = 7.5 MPa are shown in Figure 4.3 ($R_c^2 \approx 0.964$ and $R_e^2 \approx 0.951$).

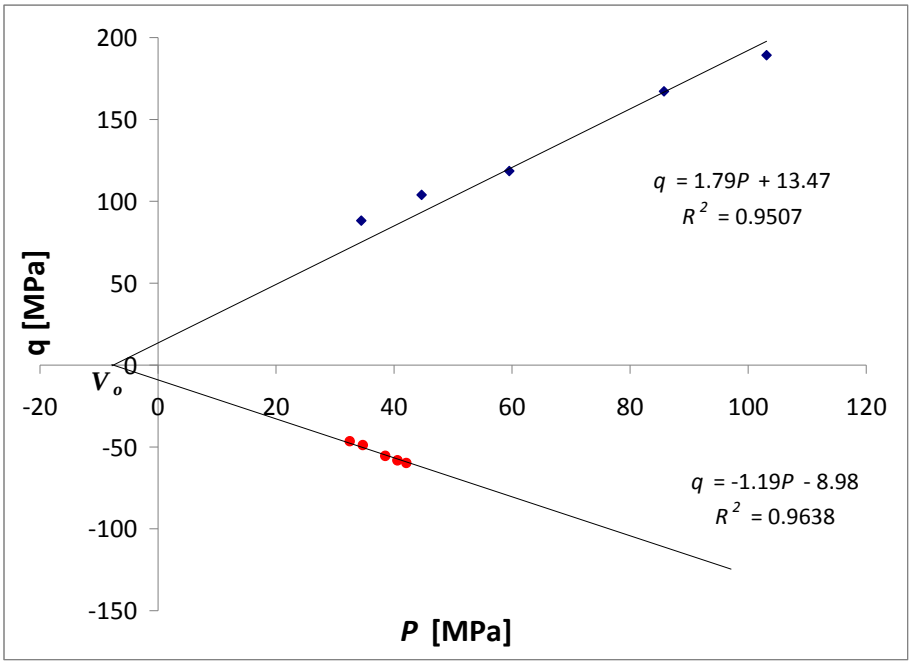

Figure 4.3: Failure envelope for dry Berea sandstone in q-P plane.

A difference in friction angles in compression and extension is observed: $\varphi_c = 43.6°$ and $\varphi_e = 47.9°$. The friction angle measured in conventional triaxial extension tests was larger than the one measured from compression tests, a sufficient but not necessary condition of the intermediate stress effect.

For the Mohr-Coulomb failure criterion, it is interesting to note that the friction angle φ can be obtained from the angle of shear band inclination θ measured from the direction of minor principal stress (Jaeger and Cook 1976):

$$\theta = 45^o + \varphi/2 \tag{4.5}$$

The friction angle from the specimen shown in Figure 4.4 was measured to be $\varphi = 42°$.

Figure 4.4: Berea sandstone specimen failed in triaxial compression.

For isotropic rock, knowledge of the two internal friction angles φ_c and φ_e, and one strength parameter such as the vertex V_o, is sufficient to define a six-sided failure surface in the principal stress space σ_1, σ_2, σ_3, now with no order implied (Figure 4.5).

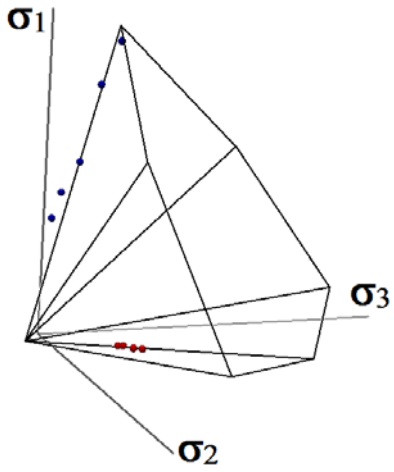

Figure 4.5: Six-sided failure surface for Berea sandstone in principal stress space.

To compare the results of the conventional triaxial tests with the plane strain experiments, a plane perpendicular to the hydrostatic axis ($\sigma_1 = \sigma_2 = \sigma_3$) called the π-plane and described by $P = constant$ can be considered. The intersection of the failure surface and the π-plane is a hexagon that displays a three-fold symmetry. The result of a plane strain compression tests can be presented on the plane (Figure 4.6).

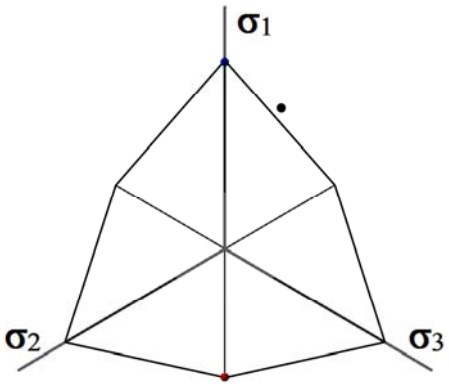

Figure 4.6: The result of plane strain compression test (black dot) in π-plane, red and blue dots represent the lines fitting the conventional triaxial extension and compression data.

It was observed that the six-sided failure surface did not predict well the principal stresses at failure measured for five specimens tested in plane strain compression. However, a best-fit line (R^2 = 0.97) was constructed in the principal stress space to fit the plane strain test data with the constraint that V_o = 7.5 MPa, the same one as measured in conventional triaxial testing. Using again the assumption of isotropy, and hence three-fold symmetry, the new failure surface is presented as a twelve-sided pyramid (Figure 4.7).

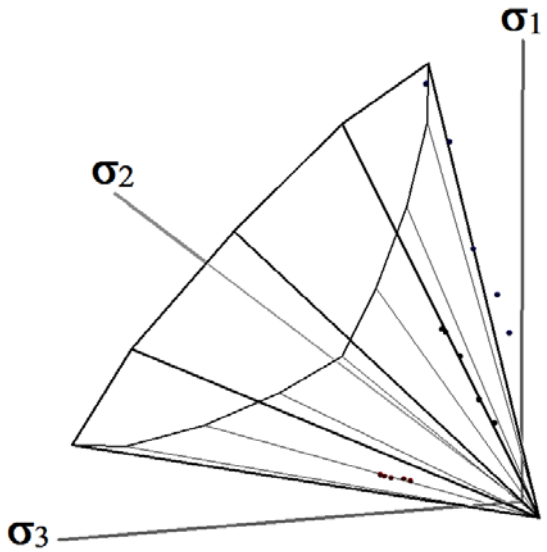

Figure 4.7: Results of conventional triaxial extension (red dots) and compression (blue dots) tests and plane strain compression tests (black dots) in π-plane.

The intermediate stress effect can also be illustrated by projecting the results of plane strain compression and axisymmetric compression and extension experiments on $\sigma_1 - \sigma_3$ plane and presenting them in terms of parameters $t = (\sigma_1 - \sigma_3)/2$ and $s = (\sigma_1 + \sigma_3)/2$. In Figure 4.8, it can be seen that the largest "plane" friction angle is observed for conventional triaxial extension, where $\sigma_2 = \sigma_1$. The case $\sigma_2 = \sigma_3$ is illustrated by the conventional triaxial compression, where the plane friction angle is the smallest. Finally, the intermediate value of the plane friction angle is calculated for the case of plane strain compression where $\sigma_1 > \sigma_2 > \sigma_3$.

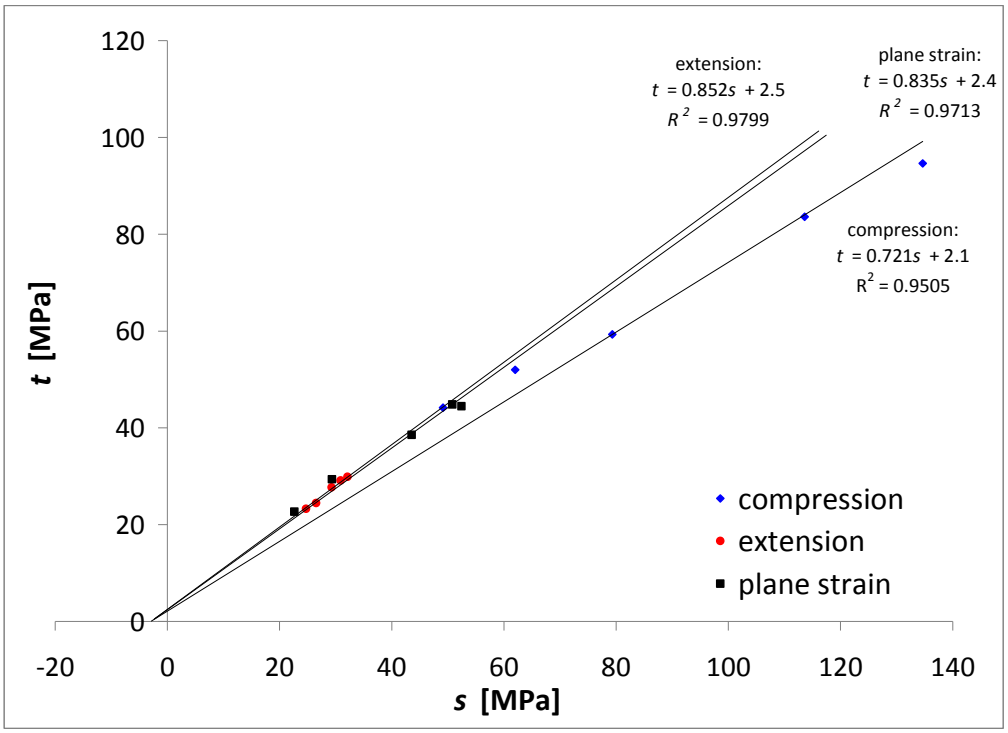

Figure 4.8: Results of conventional triaxial extension and compression tests and plane strain compression data in *s*-*t* plane.

4.1.3 Index properties

Porosity

Six specimens of different size (at least 50 mm long) and shape (cylindrical and prismatic) were oven dried and then submerged in deaired water. The water tank was

placed in a sealed container and the air was evacuated for 15 minutes. Then, wet specimens were weighed. The procedure was repeated twice a day for three days until the weight of the wet specimens became constant, so it could be assumed that all the air trapped in the pores was replaced by water, and hence water volume was equal to the (connected) pore volume. Knowing wet and dry masses of the specimens, m_{wet} and m_{dry}, and $\rho_{water} = 1000$ kg/m^3, interconnected porosity ϕ_o was calculated from

$$\phi_o = \frac{m_{wet} - m_{dry}}{V \rho_{water}} \tag{4.6}$$

and found to be $\phi_o = 0.23$ for all the specimens.

Permeability

In the case of zero body forces acting on the specimen, Darcy's law states that the flow q_i in the x_i direction is proportional to the pore pressure change in this direction:

$$q_i = -\kappa \frac{\partial p}{\partial x_i} \tag{4.7}$$

where $\kappa = k/\mu$ is the mobility coefficient expressed in terms of intrinsic permeability k and fluid dynamic viscosity μ. Interpreting the parameters from equation (4.7) in terms of quantities that can be experimentally measured, k can be written as:

$$k = \frac{\Delta V_f \cdot \mu \cdot L}{\Delta t \cdot A \cdot \Delta p} \tag{4.8}$$

where ΔV_f is the volume of water coming out of the saturated specimen in the downstream channel for the time Δt due to an increment of pore pressure Δp applied upstream. L and A are the specimen length and cross-sectional area in the direction of flow and μ = 0.001 Pa·s for water at room temperature. Intrinsic permeability k was measured to be 40 mD (1 mD = 10^{-15} m^2) at P = 5.2 MPa and p = 0.2 MPa, and k = 29 mD at P = 20 MPa and p = 0.2 MPa.

Diffusivity

The diffusion equation describes the pore pressure change in the specimen:

$$c\nabla^2 p = \frac{\partial p}{\partial t} \tag{4.9}$$

where c is the diffusivity, which governs the rate of diffusion and can be expressed by the intrinsic permeability k and poroelastic parameters (Rice and Cleary 1976):

$$c = \frac{2kG(1-\nu)(\nu_u - \nu)}{\mu\alpha^2(1-2\nu)^2(1-\nu_u)} \tag{4.10}$$

For P' = 5 MPa, using G, ν, ν_u and α reported in section 4.3, c was calculated to be equal to 0.2 m^2/s. Berchenko *et al.* (2004) suggested that the time t for the dissipation of the stress-induced pore pressure is of order $L^2/4c$ for the mean stress increment of 1 MPa. For the given c and the characteristic specimen length L = 0.1 m, the time to equilibrate pore pressure in the specimen is on order of 0.01 s, meaning that the changes in strain can be recorded simultaneously with the applied load for the rates considered (< 0.1 MPa/s).

4.2 Saturation

The results of the back pressure saturation process for one of the undrained plane strain compression experiments are presented in Figure 4.9. The increments of pore pressure Δp for constant increments of $\Delta\sigma_1 = \Delta\sigma_3 = 0.34$ MPa are plotted versus back pressure.

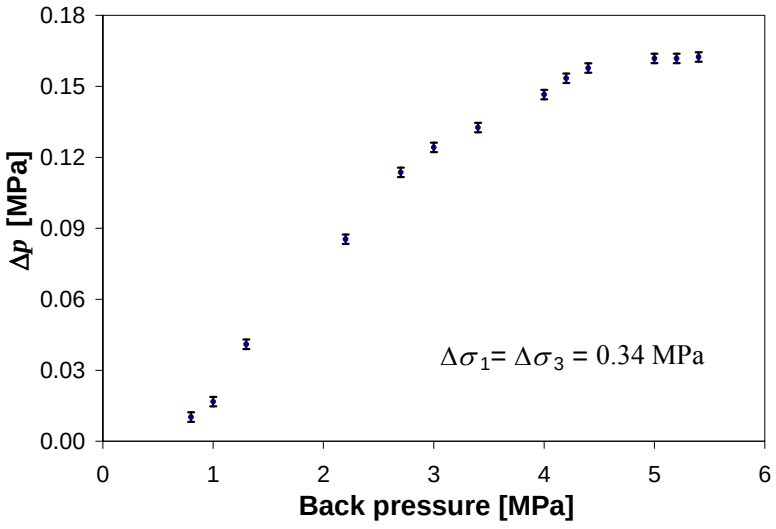

Figure 4.9: Changes in the pore pressure due to the constant increments in the mean stress as a function of back pressure.

It can be observed that at low back pressures, increments of pore pressure due to increments in mean stress are very small, which can be explained by the load taken by the rock matrix. The pore fluid at $p < 4$ MPa consists of water and air, and hence is more compressible than just pure water. However, with increasing back pressure, air bubbles dissolve in water; Δp is increasing and becomes constant when $p > 4$ MPa. At back pressures above this value, the specimen is fully saturated and K_f can be taken as that of pure water: $K_f = K_{water} = 2.24$ GPa.

Using independently measured drained bulk modulus K and Biot coefficient α (see section 4.3), B^{cor} can be calculated from equation (3.63), assuming $\tilde{\nu}$ is changing from $\nu = 0.31$ in a drained condition to $\nu_u = 0.35$ in an undrained case (section 4.3), and that pore water lines were filled with deaired water, $K_f = 2.24$ GPa, from the beginning of the back pressure saturation process. The calculated B-values are presented in Figure 4.10.

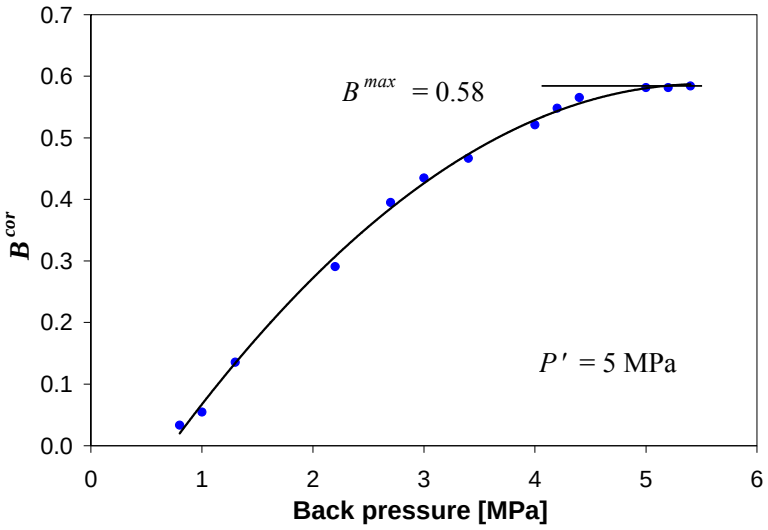

Figure 4.10: Change in B^{cor} with back pressure at $P' = 5$ MPa.

The maximum value of the Skempton coefficient achieved in plane strain compression experiments at $P' = 5$ MPa ($P' = P - p$) and corrected for the compliance of the measuring system was $B^{cor} = 0.58$. However, the maximum B-value measured in conventional triaxial compression was $B^{cor} = 0.61$. This difference in the results cannot be explained by the accuracy of measurements, which is estimated to be 0.01. As it was mentioned in section 3.3, pure hydrostatic loading cannot be applied in plane strain testing because the

intermediate principal stress σ_2 is not controlled. Thus, when $\Delta\sigma_1 = \Delta\sigma_3$ is applied, some deviatoric load is still present and the Skempton A coefficient plays a role. Its development with increasing back pressure was measured and corrected (equation 3.67) for the compliance of the measuring system (Figure 4.11).

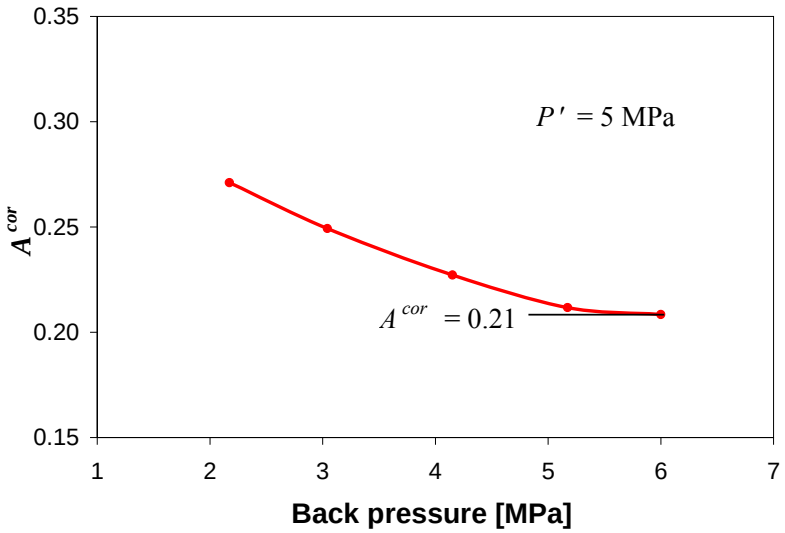

Figure 4.11: Change in Skempton parameter A^{cor} with back pressure at $P' = 5$ MPa.

The value of A achieved at full saturation was measured to be $A^{cor} = 0.21$. Now, from equation (2.47), it can be obtained that the value of B measured in plane strain compression is underestimated by 4 – 5% if the influence of $A \neq 1/3$ is disregarded. So, $B^{cor} = 0.61$ could be taken as the final value of the Skempton coefficient at $P' = 5$ MPa and compared with B calculated from the results of drained and undrained compression experiments (see section 4.3) using equation (2.22): $B = 0.47 – 0.63$. The latter one has a wide range because of the variation in measured drained and undrained bulk moduli and Biot coefficient. Nevertheless, reaching $B = 0.61$ means that full saturation was achieved. These results are also in agreement with the experimental observations of Hart and Wang (2010), who measured B-values for their Berea sandstone to be in the range 0.61 – 0.68 from conventional triaxial tests conducted at 4.0 – 5.7 MPa effective mean stress, and Lockner and Stanchits (2002) with the measured $B = 0.55 – 0.65$ for effective mean stresses of 5 – 10 MPa.

The alternative way to check saturation of a lab specimen is based on the observation that compressional waves (P-waves) propagate in saturated geomaterials with a velocity that is strongly affected by water filling the voids (Bardet and Sayed 1993). Strachan (1985) suggested the following criterion for ensuring full saturation: P-wave velocity in the saturated material becomes constant with increasing back pressure keeping effective mean stress constant. Two sensors were attached to the opposite sides of a prismatic specimen and P-wave velocity was measured during the saturation process at a constant effective mean stress $P' = 5$ MPa (Figure 4.12).

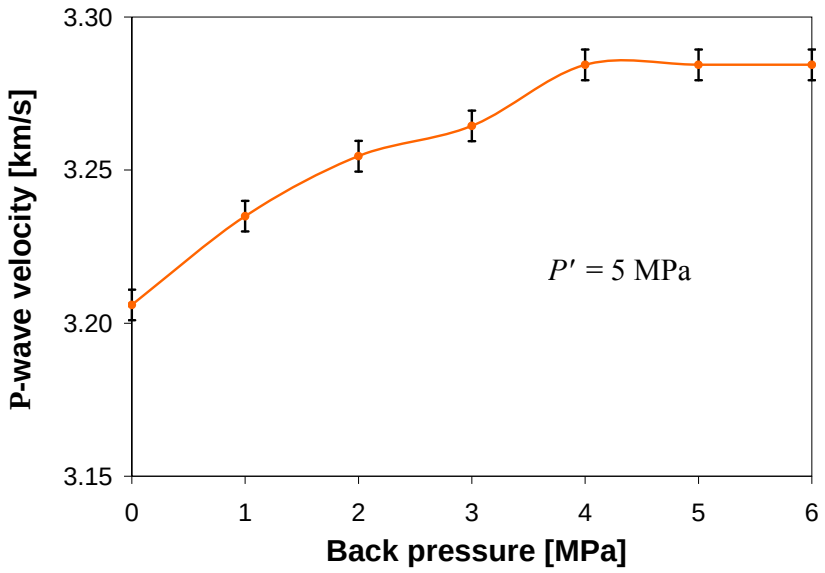

Figure 4.12: Change in P-wave velocity with back pressure.

The change in P-wave velocity with back pressure in Berea sandstone is not strongly pronounced as in soil (Strachan 1985; Bardet and Sayed 1993). However, it can be seen that the velocity is increasing with the back pressure and becomes constant when p exceeds 4 MPa, which supports the proposed B-check method in achieving full saturation.

Skempton B coefficient was also measured in axisymmetric compression test at $P' = 17$ MPa (Figure 4.13). Its value stabilized at back pressures > 3 MPa with the maximum $B^{cor} = 0.38$. This value is significantly smaller than the one measured at $P' = 5$ MPa, and

shows that B is decreasing with increasing effective mean stress at low (< 30 MPa) pressures (Blöcher *et al.* 2007; Hart and Wang 2010).

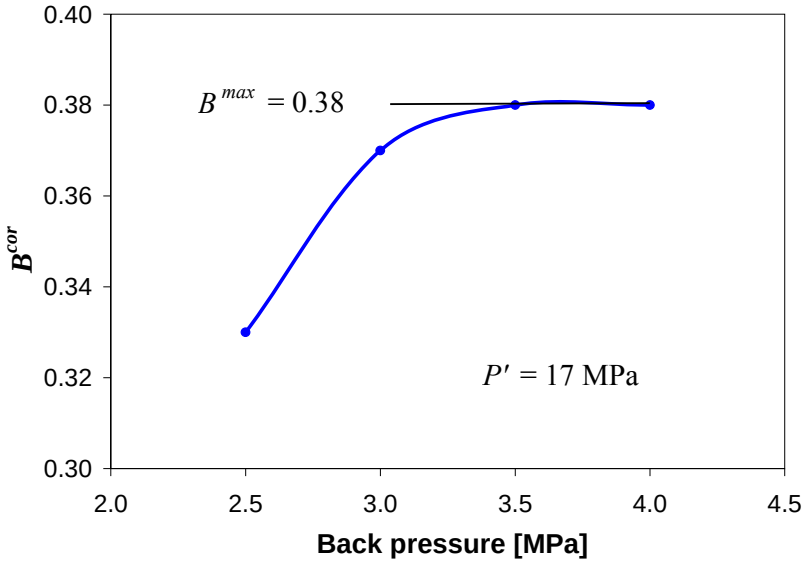

Figure 4.13: Change in B^{cor} with back pressure at P' = 17 MPa.

4.3 Isotropic poroelastic parameters

4.3.1 Hydrostatic compression results

Three prismatic 53 x 35 x 35 *mm* specimens were tested under jacketed and then unjacketed conditions. Linear strains measured in the direction perpendicular to bedding planes (z – direction) are 5 – 8% smaller than those along the beds, which confirms a slight material anisotropy. Strains measured in three perpendicular directions (x, y, z) in jacketed and unjacketed compression are shown in Figures 4.14 and 4.15, respectively. It can be seen from Figure 4.14 that strains measured in three perpendicular directions are different within 10%, showing that the rock is elastically anisotropic in dry conditions. However, the presense of liquid in the material (unjacketed condition) makes two strains measured along the bedding planes approximately the same, and hence the rock can be treated as poroelastically transversely isotropic.

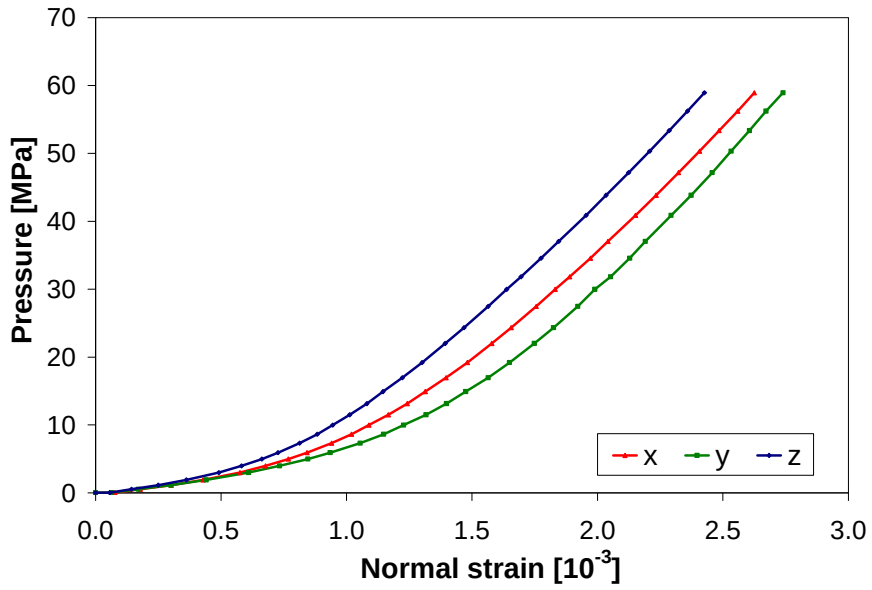

Figure 4.14: Strains measured in x, y, z directions in hydrostatic jacketed compression (dry specimen).

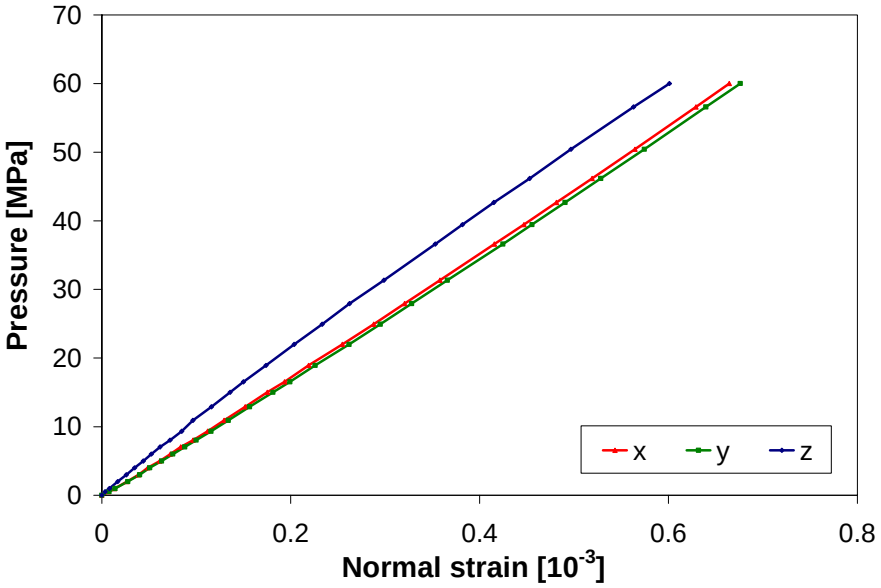

Figure 4.15: Strains measured in x, y, z directions in hydrostatic unjacketed compression (saturated specimen).

Bulk moduli calculated from jacketed hydrostatic compression tests are found to be increasing with pressure: K = 5 GPa for P = 2 MPa, K = 7 GPa at P = 5 MPa, and K = 13

GPa (and constant) when hydrostatic pressure exceeded 30 MPa. The unjacketed bulk modulus is measured to be constant for pressures from 1 – 60 MPa: K_s' = 29.4 – 30.9 GPa. Additionally, a fused quartz specimen was tested; its volumetric strain response is linear up to P = 60 MPa and its bulk modulus is K_{quartz} = 37.0 GPa. The results of the hydrostatic compression experiments are summarized in Table 4.2 and presented in Figure 4.16.

Table 4.2: Jacketed and unjacketed bulk moduli measured in three hydrostatic compression tests.

Test name	$K_{5\ MPa}$ [GPa]	$K_{>30\ MPa}$ [GPa]	K_s' [GPa]
HCBS-1	7.1	13.3	30.9
HCBS-2	6.9	12.9	29.4
HCBS-3	6.8	12.7	29.8

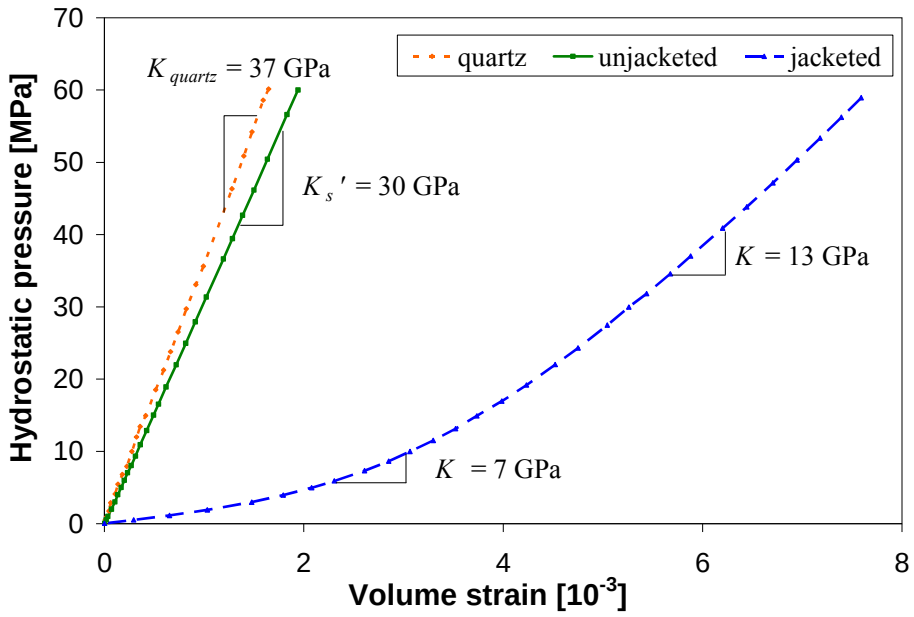

Figure 4.16: Results of jacketed and unjacketed hydrostatic compression tests on Berea sandstone and quartz.

By measuring strains in the diagonal directions, all components of the strain tensor ε_{ij} can be calculated. As an example, the stress tensor at P = 60 MPa for unjacketed HCBS-3 specimen was:

$$\varepsilon_{ij} = \begin{pmatrix} \varepsilon_{xx} & \varepsilon_{xy} & \varepsilon_{xz} \\ \varepsilon_{xy} & \varepsilon_{yy} & \varepsilon_{yz} \\ \varepsilon_{xz} & \varepsilon_{yz} & \varepsilon_{zz} \end{pmatrix} = \begin{pmatrix} 0.690 & -0.015 & 0.045 \\ -0.015 & 0.700 & -0.025 \\ 0.045 & -0.025 & 0.630 \end{pmatrix} \times 10^{-3}$$

Calculated eigenvectors and eigenvalues for the strain tensor are

$$eigenvalues = (\varepsilon_1,\ \varepsilon_2,\ \varepsilon_3) = \begin{pmatrix} 0.733 & 0 & 0 \\ 0 & 0.683 & 0 \\ 0 & 0 & 0.603 \end{pmatrix} \times 10^{-3}$$

$$eigenvectors = (\underline{e}_1,\ \underline{e}_2,\ \underline{e}_3) = \begin{pmatrix} 0.658 & -0.616 & 0.432 \\ -0.615 & -0.772 & 0.162 \\ 0.434 & -0.159 & 0.887 \end{pmatrix}$$

Eigenvectors are represented in Figure 4.17; $\underline{e}_3$ is almost aligned with the z-direction and $\underline{e}_1$ and $\underline{e}_2$ are approximately parallel to the beddings plane. Also, ε_3 is smaller than ε_1 and ε_2, and the latter two are different but very sensitive to small variations in ε_{xx}, ε_{yy}, and ε_{xy}, which allowed the approximation of the sandstone as transversely isotropic.

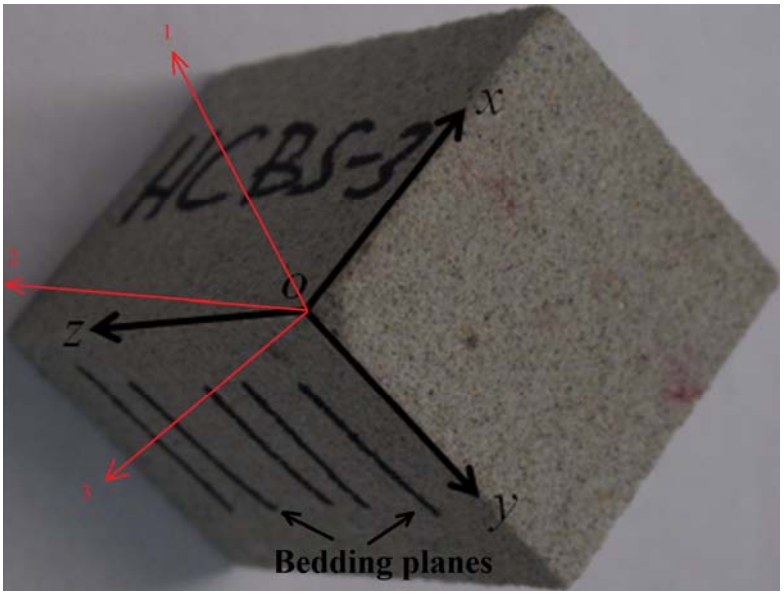

Figure 4.17: Directions of principal strains calculated for the prismatic specimen tested in hydrostatic unjacketed compression.

4.3.2 Plane strain and axisymmetric compression results

Berea sandstone prismatic specimens were cut and then precisely ground from the same block in the same direction, such that the axial load in plane strain testing was applied approximately perpendicular to the bedding planes. Eight tests were performed and identified as BxBS-ij (i is the test number, j = d for drained test or u for undrained). Drained and undrained Young's moduli and Poisson's ratios E, E_u, ν, and ν_u were measured in deviatoric unloading ($\Delta\sigma_1 < 0$, $\Delta\sigma_3 = 0$) at $P' = 5.0 - 5.5$ MPa. These parameters are presented in Table 4.3, along with the calculated drained and undrained bulk moduli K and K_u and shear modulus G.

Table 4.3: Poroelastic results of drained and undrained plane strain experiments.

Test #	P [MPa]	p [MPa]	E, E_u [GPa]	ν, ν_u	K, K_u [GPa]	G [GPa]
BxBS-6d	6.0	0.5	10.9	0.31	9.6	4.2
BxBS-11d	5.0	0.0	10.8	0.32	10.0	4.1
BxBS-13d	8.0	3.0	11.3	0.30	9.4	4.3
BxBS-14d	10.0	5.0	11.3	0.31	9.9	4.3
BxBS-2u	8.0	2.6	13.2	0.34	13.8	4.9
BxBS-3u	10.0	4.4	13.5	0.35	15.0	5.0
BxBS-12u	10.0	4.8	15.1	0.34	15.9	5.9
BxBS-15u	10.0	5.0	14.5	0.34	15.1	5.4

An estimate of the Biot coefficient α was attempted by measuring the change in pore volume from the fluid expelled from the specimen (equation 3.36). In one of the drained plane strain compression test performed at $P = 5 - 7$ *MPa* and $p = 0$ *MPa*, water coming out of the specimen during deviatoric loading was collected and weighed. The measured volume of drained water was around 0.20 ml (typical specimen volume $V = 380$ ml) in each of the three loading cycles of this type. The Biot coefficient α is calculated (equation 3.36) to be $\alpha = 0.7$. This type of measurements is not precise because the water drained from the specimen came in the form of small drops 0.02 – 0.03 ml each.

Additionally, two cylindrical specimens were prepared such that the axial load was applied approximately perpendicular to the bedding planes. Bulk moduli were measured

under drained, undrained, and unjacketed conditions in conventional triaxial hydrostatic unloading at $P' = 5$ MPa ($P = 10$ MPa, $p = 5$ MPa) and are reported in Table 4.4.

Table 4.4: Results of drained, undrained, and unjacketed conventional triaxial tests.

Test #	P [MPa]	p [MPa]	K [GPa]	K_u [GPa]	K_s' [GPa]
TriBS-1	10	5	9.8	15.9	29.4
TriBS-2	10	5	10.1	15.6	29.1

4.3.3 Discussion

The unjacketed bulk modulus of the rock and the bulk modulus of quartz, the main mineral that forms it, were measured in hydrostatic compression experiments and are found to be stress independent at the range of stresses applied (up to 60 MPa). K_s' was also measured in conventional triaxial tests performed at the effective mean stresses equal to 5 MPa ($P = 10$ MPa and $p = 5$ MPa) and 17 MPa ($P = 20$ MPa and $p = 3$ MPa). The obtained results are consistent and give the following range for unjacketed bulk modulus $K_s' = 29.1 – 30.9$ GPa. The reported values are smaller than the measured bulk modulus of quartz $K_{quartz} = 37.0$ GPa, where it is often assumed $K_s = K_s' = K_s''$ for sandstones (Rice and Cleary 1976; Mesri *et al.* 1976; Sulem and Ouffroukh 2006).

To investigate the observed difference, the rock's microstructure was viewed. American Engineering Testing (St. Paul, MN) performed the microphotograph analysis of a sample of Berea sandstone measuring 95 x 100 x 25 mm, which was vacuum-impregnated, multiple times, with epoxy stained with both black and fluorescent dye in order to lend clarity to the structure of pore space. Thin sections were cut from the original sample and photographed with 100x magnification (Figure 4.18).

Microphotograph analysis showed that some pores, like the one marked in Figure 4.18, were not filled by the epoxy and, hence, contribute to the non-connected porosity. Some other studies (Dullien 1992) estimated that very small and isolated pores can take up to 16% of the total pore volume in Berea sandstone. The presence of non-connected pore space causes $K_s' < K_{quartz}$ and the assumption of $K_{quartz} = K_s' = K_s''$ is not applicable for the tested rock.

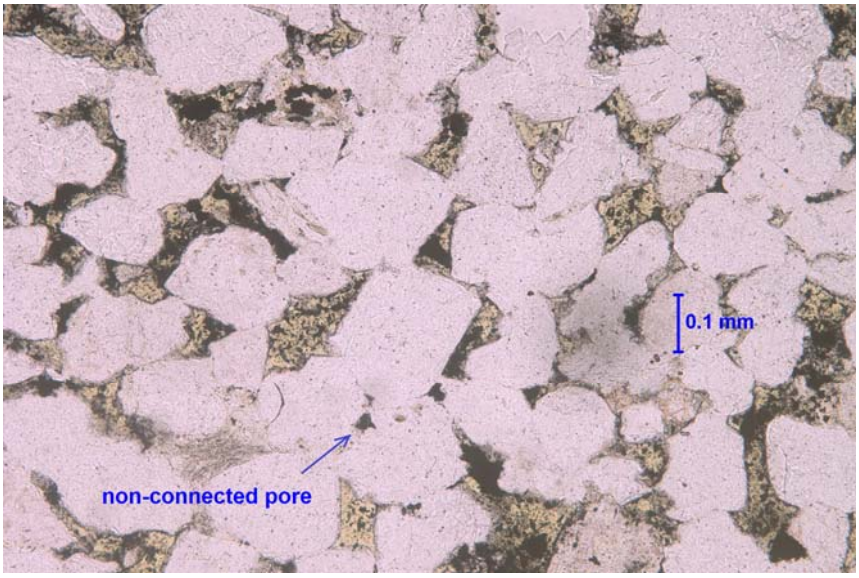

Figure 4.18: Microphotograph of Berea sandstone sample (100x magnification) with the pores filled with fluorescent dye.

Hydrostatic compression tests also show that the dry (drained) bulk modulus of Berea sandstone is a stress dependent parameter at low mean (hydrostatic) stress (< 30 MPa) and reaches its constant value K = 13 GPa only when P > 30 MPa. Because some other parameters, such as K_u and α, are dependent on K, the material response can be treated as poroelastic and stress independent only at mean stress greater than 30 MPa. However, the devices that were utilized for drained and undrained testing do not allow application of high (> 20 MPa) hydrostatic stress and the achievement of full saturation requires p > 3 – 4 MPa, so the maximum P' is limited to 16 – 17 MPa. Because the purpose of each test was not only to investigate poroelastic response but characterize the inelastic behavior and failure, even lower mean stresses were utilized, so drained and undrained parameters are reported at 5 MPa effective mean stress.

Results of the drained compression tests indicate approximately the same value for Poisson's ratio ν = 0.31 – 0.32 but a lower value of Young's modulus E = 11 GPa than those obtained in dry uniaxial compression tests. Also, dry bulk modulus measured at P = 5 MPa in the hydrostatic jacketed compression is smaller than the one calculated from drained plane strain and triaxial compression data: K = 9.4 – 10.1 GPa. These

discrepancies between dry and drained parameters might be related to the different type of loading applied in those tests. To be consistent with the measurements of undrained parameters, only the drained bulk modulus K will be used for further analysis.

Undrained Poisson's ratio was measured to be $\nu_u = 0.34 – 0.35$ and the undrained bulk modulus was calculated to be $K_u = 15.1 – 15.9$ GPa (the result of BxBS-2u was disregarded because full saturation was not achieved in this test). K_u and ν_u are larger than their drained counterparts, as predicted by poroelasticity theory. For the obtained K_s' and K, α is calculated to be in the range of 0.65 – 0.70 and the Biot modulus calculated from equation (2.25) is $M = 10.2 – 15.4$ GPa.

The only poroelastic parameter from equations (2.22), (2.31), and (2.34) that was not measured in the reported experiments is the unjacketed pore volume bulk modulus K_s". Calculation of K_s" from the relationship between drained and undrained bulk moduli (equation 2.34) gives K_s" = 3.7 – 8.6 GPa. The uncertainty in determination of K_s" is caused by the variation in K_u, K, and K_s'. Our measurements of Skempton B coefficient are more precise, so for the reported $B^{cor} = 0.61$, unjacketed pore volume bulk modulus can also be calculated from equation (3.57): K_s" = 3.7 – 4.3 GPa. However, it must be emphasized that the measured parameters are stress dependent, and this strongly affects K_s".

The reported poroelastic parameters are in some agreement with the experimental observation of Hart and Wang (1995, 2010), who performed drained and undrained conventional triaxial tests on Berea sandstone. They measured $K = 3.4 – 5.9$ GPa, $K_u = 11.1 – 14.3$ GPa, $\nu_u = 0.32 – 0.37$, and $B = 0.61 – 0.75$ for the effective mean stress of 3 – 10 MPa; using these data, they found K_s' = 27 – 34 GPa and K_s"= 3.2 – 7.0 GPa.

To analyze why the obtained unjacketed moduli K_s' and K_s" are so different, the relationships between micromechanical elements need to be reviewed. The following equations hold for increments (increment of a quantity is current minus initial quantities) of porosity $\Delta\phi$, total volume ΔV, pore volume ΔV_ϕ, and solid volume ΔV_s (Detournay and Cheng 1993):

$$\begin{cases} \dfrac{\Delta V}{V} = \dfrac{\Delta V_s}{V_s} + \dfrac{\Delta\phi}{1-\phi_o} \\ \dfrac{\Delta V_\phi}{V_\phi} = \dfrac{\Delta V_s}{V_s} + \dfrac{\Delta\phi}{\phi_o(1-\phi_o)} \end{cases} \tag{4.11}$$

If external mean stress (ΔP) and pore pressure (Δp) are now applied to the element, $\Delta P' = \Delta P - \Delta p$ (sign convention is compression positive), then

$$\begin{cases} \dfrac{\Delta V}{V} = \dfrac{\Delta P'}{K} - \dfrac{\Delta p}{K_s'} \\ \dfrac{\Delta V_\phi}{V_\phi} = \dfrac{\Delta P'\alpha}{\phi_o K} - \dfrac{\Delta p}{K_s''} \end{cases} \tag{4.12}$$

and the following expression for the increment in porosity $\Delta\phi$ is obtained:

$$\Delta\phi = \Delta P'\left(\frac{1-\phi_o}{K} - \frac{1}{K_s'}\right) - \phi_o \Delta p\left(\frac{1}{K_s'} - \frac{1}{K_s''}\right) \tag{4.13}$$

So, $\Delta\phi$ for the case of unjacketed compression $\Delta P' = 0$ becomes:

$$\Delta\phi = -\phi_o\left(\frac{1}{K_s'} - \frac{1}{K_s''}\right)\Delta p \tag{4.14}$$

If we now make an assumption that $K_s' = K_s''$, then $\Delta\phi \equiv 0$, so porosity does not change during unjacketed compression. If $K_s' > K_s''$, then $\Delta\phi > 0$ in compression; or, conversely, if porosity is increasing during unjacketed compression, then $K_s' > K_s''$ should be satisfied.

The difference between unjacketed bulk modulus K_s' and unjacketed pore bulk modulus K_s'' could be explained by the presence of highly compressible clay cement between quartz grains in Berea sandstone. Christensen and Wang (1985) showed that the quartz grains were coated with clay, which also partially filled the pores in the sandstone they tested. In case of unjacketed compression, compliant clay grains strain at a greater rate than the stiffer quartz grains, with the result that the porosity increases because the more compliant grains now contribute less to the volume of the solid portion of the rock. So, an increase in pore pressure has a stronger impact on the change of pore volume than the

equal increase in confining pressure. Hence, unjacketed bulk modulus could be significantly larger than unjacketed pore volume bulk modulus. However, according to the petrographic analysis provided in section 4.1.1, this is not the case for the Berea sandstone tested in this work, because only traces of clay were found in the material. The cementation of quartz grains is claimed to occur mainly as interstitial microquartz overgrowths, which should not make the rock pores significantly more compliant than the bulk.

The lower limit for K_s'' predicted by poroelasticity theory can be obtained from the equation derived by Brown and Korringa (1975) from the definitions of K_s', K_s'' and K_s (equations 2.27 – 2.29):

$$\frac{1}{K_s'} = \frac{\phi_o}{K_s''} + \frac{1-\phi_o}{K_s} \tag{4.15}$$

If we assume now that the maximum value of K_s is K_{quartz} = 37.0 GPa, then the minimum value of K_s'' is 17 GPa. Equation (4.15) also shows that K_s'' = 4 GPa is not physically possible if the tested sandstone is assumed to behave as linear poroelastic material, since in this case $K_s < 0$. The unjacketed pore volume bulk modulus was not measured, but calculated from stress dependent parameters, and is thus a stress dependent parameter itself. Bulk modulus K, Biot coefficient α, and Skempton coefficient B^{cor} were also measured for fully saturated specimen at P' = 17 MPa (P = 20 MPa, p = 3 MPa): K = 11.3 GPa, α = 0.61, and B^{cor} = 0.38 (see section 4.5). For this case, K_s'' calculated from equation (3.57) is 18.1 GPa. Hence, when poroelastic moduli approach constant values, a value of K_s'' may become more reliable in terms of micromechanical considerations of poroelasticity theory. However, the direct experimental measurement of K_s'' is needed to investigate if it is stress independent parameter and behaves similar to K_s' or is an increasing function of applied stress like K.

Finally, the shear modulus calculated from the drained deviatoric loading G = 4.1 – 4.3 GPa was found to be smaller than the undrained one: G = 4.9 – 5.9 GPa. This violates the requirement of isotropic poroelasticity, as these two parameters should be the same. Berryman (2005) showed that such a discrepancy in shear moduli can be explained by

anisotropy of the tested material. Poroelastic parameters measured for the special case of anisotropy, transverse isotropy, are considered in the next section.

4.4 Transversely isotropic poroelastic parameters

The results of hydrostatic compression experiments show that Berea sandstone can be treated as a transversely isotropic material. Performing conventional triaxial tests, independent loading (1 MPa) was applied in axial (perpendicular to the bedding planes) and radial (parallel to the beds) directions and correspondent changes in pore pressure in the specimen were recorded and corrected for the extra volume of the fluid in the measuring system. The transversely isotropic Skempton B coefficients, B' and B related to the application of axial and radial loads, respectively, were calculated at $P' = 5$ MPa and plotted vs back pressure in Figure 4.19.

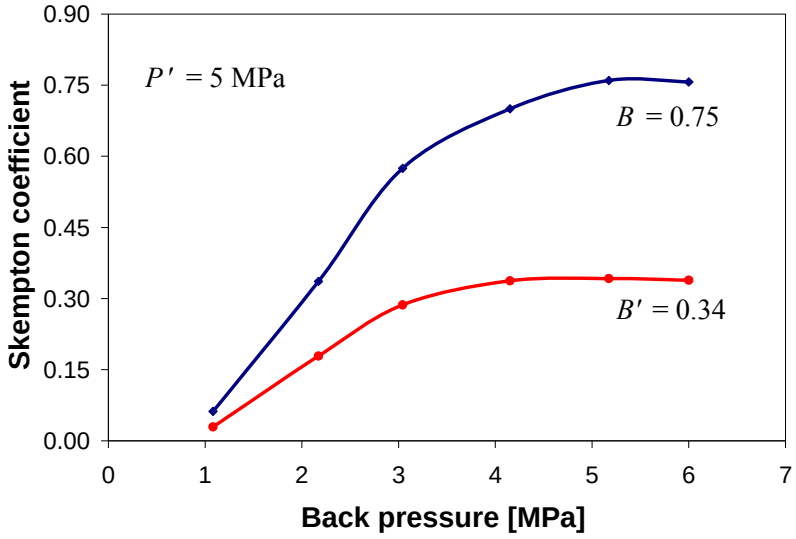

Figure 4.19: Generalized Skempton coefficients B' and B as functions of back pressure.

Axial stress was found to produce significantly smaller increments in pore pressure than the stress applied to the cylindrical specimens in the radial direction. The maximum values of B and B' were calculated to be 0.75 and 0.34. The tested specimen was considered to be fully saturated at $p > 4$ MPa.

Using the methods described in sections 3.2 and 3.3, drained and undrained parameters E, E', ν, and ν' were calculated from the plane strain and axisymmetric compression data.

The tests were performed at P = 10 MPa, p = 5 MPa as 1 MPa unloading steps in either axial or radial direction. The results are presented in Table 4.5.

Table 4.5: Measured drained and undrained transversely isotropic poroelastic parameters.

	E (GPa)	E' (GPa)	ν	ν'
Drained	10.0	10.9	0.33	0.28
Undrained	15.0	16.1	0.40	0.34

The results satisfy the inequalities (2.80) and (2.81), which have to be preserved for transversely isotropic poroelastic parameters. Components of the stiffness matrix $\underline{\underline{M}}$ and compliance matrix $\underline{\underline{C}}$ under drained and undrained conditions, as well as the shear modulus G, were computed from equations (2.56) – (2.61) and are reported in Table 4.6.

Table 4.6: Elements of drained and undrained stiffness matrix (reported in GPa) and compliance matrix (reported in 1/GPa).

	G	M_{11}	M_{12}	M_{13}	M_{33}	C_{11}	C_{12}	C_{13}	C_{33}
Drained	3.8	13.3	5.7	5.3	13.9	0.100	-0.033	-0.026	0.092
Undrained	5.4	24.9	14.1	13.3	25.1	0.067	-0.027	-0.021	0.062

The calculation of G from the components of transversely isotropic stiffness matrix explains the result reported earlier: the shear modulus obtained from the undrained response is significantly larger than the drained one. The consistency of other presented data and the assumption of transversely isotropic poroelastic material behavior can be tested by comparing the parameters measured under undrained conditions with those predicted from the drained response. B, B', α, and α' calculated using the governing equations (2.64) – (2.67) can be compared with the measured B and B', as well as with α and α', provided by relations (2.77) – (2.78). Also, the components of the undrained stiffness matrix, M_{11}^{u}, M_{12}^{u}, M_{13}^{u}, and M_{33}^{u} can be compared with their predictions from equations (2.73) – (2.76).

Taking ϕ_o = 0.23, K_f = 2.24 GPa, K_s' = 30 GPa, and assuming that K_s'' takes its estimated pressure independent value of 18.1 GPa, Biot modulus was calculated to be M = 12.7 GPa, which in the range of M reported for isotropic poroelastic response. The other parameters predicted by the model are presented in Table 4.7.

Table 4.7: Measured and predicted transversely isotropic poroelastic parameters assuming K_s'' = 18.1 GPa (M_{ij}^u reported in GPa).

	α	α'	B	B'	M_{11}^u	M_{11}^u	M_{11}^u	M_{11}^u
Measured	0.73	0.73	0.75	0.34	24.9	14.1	13.3	25.1
Predicted	0.88	0.74	0.50	0.49	23.2	15.7	13.7	20.9

Large discrepancy between measured B and B' is not predicted by the transversely isotropic poroelastic model. However, the components of the undrained stiffness matrix and α' are predicted closely. Moreover, Lockner and Beeler (2003) performed drained and undrained triaxial tests on Berea sandstone at different mean stresses and reported the following values at P = 20 MPa, p = 10 MPa: B = 0.64, B' = 0.38, α = 0.75, and α' = 0.69. So, similarly to the present study, nearly isotropic Biot coefficients and strongly anisotropic Skempton coefficients were observed.

Finally, undrained poroelastic response of Berea sandstone can be well predicted by the transversely isotropic model in terms of Biot coefficient α' and the components of the stiffness matrix. However, the big discrepancy between Skempton coefficients measured due to the loading applied along the bedding planes, B = 0.75, and perpendicular to them, B' = 0.34, is not captured by the model. It might have a more involved nature than just the difference in compliances along and perpendicular to the bedding planes. Moreover, the assumption of microhomogeneity, *i.e.* homogeneity of the skeleton at the microscopic pore scale (Nur and Byerlee 1971; Cheng 1997) might not be true for the tested sandstone.

4.5 Inelastic deformation

Failure of rock involves microcracking, which generates elastic waves known as acoustic emission (AE). For a wide variety of brittle rocks and over a wide range of confining pressures, dilatant deformation was found to be accompanied by small-scale fracturing (Scholz *et al.* 1968; Riedel and Labuz 2007). Thus, monitoring of AE activity in the rock can be a tool for the determination of the onset of inelastic response. Figure 4.20 represents the results of dry plane strain compression experiment on the sandstone in terms of volume strain and recorded AE events. It can be seen that AE rate increases at the onset of inelastic deformation, where the volume strain response deviates from linearity, and is approximately constant almost up to the peak load. The same technique can be implemented for fluid-saturated rock testing.

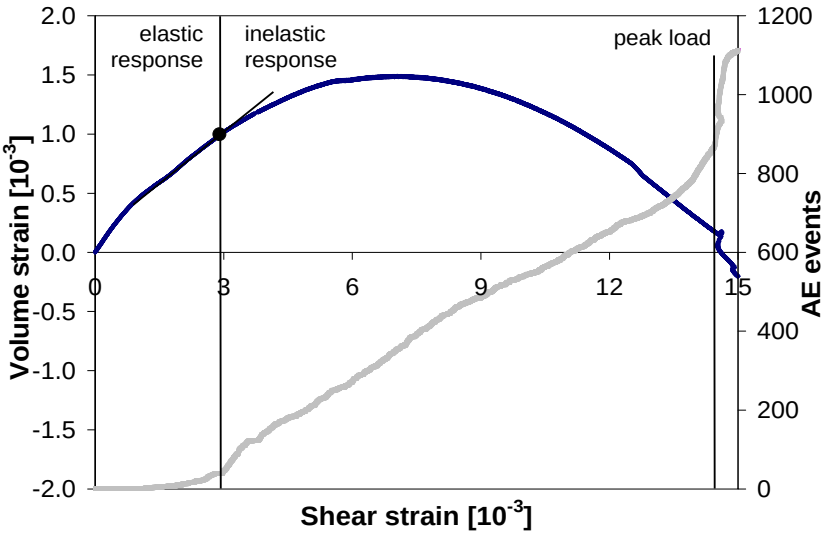

Figure 4.20: Volume strain and AE in plane strain compression of dry sandstone.

4.5.1 Plane strain compression

After the full saturation of the sandstone specimens was achieved and the poroelastic parameters were measured, plane strain compression loading was performed to failure. Axial load was applied (axial strain rate was kept at ~ 10^{-6} s^{-1}) and the cell pressure σ_3 was preserved constant. Five drained and five undrained plane strain compression

experiments were conducted. The results of four of them, two drained and two undrained, are presented in Figure 4.21.

Effective mean stresses at failure, designated as P' in Figure 4.21, were significantly different for the tests reported in Figure 4.21, although the initial effective mean stress for each of them was approximately the same, 5 – 7 MPa (Figure 4.22).

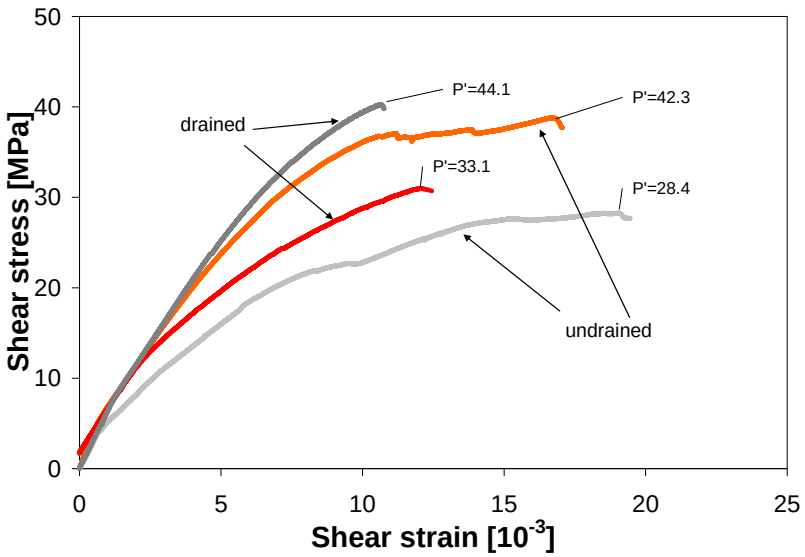

Figure 4.21: Constitutive response in drained and undrained plane strain compression.

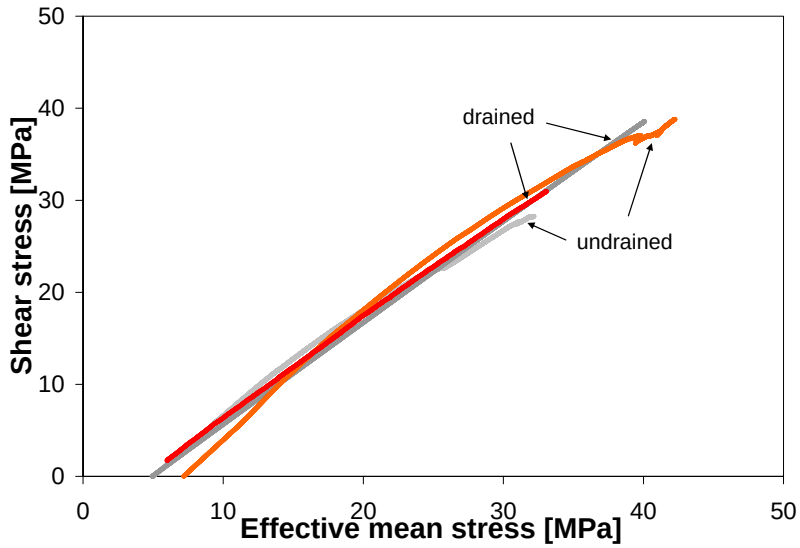

Figure 4.22: Stress paths in the plane strain compression experiments.

The drained-undrained test pair (red and orange curves, respectively, in Figure 4.20) can be considered. The drained test was performed with σ_3 = 6.0 MPa and initial pore pressure p = 0.5 MPa, and the undrained test was conducted at σ_3 = 10.0 MPa and initial pore pressure p = 2.8 MPa. It can be seen from Figure 4.20 that the undrained response is stronger than its drained counterpart starting from a value of $\gamma = 2.2\times10^{-3}$. The effective mean stress at the beginning of the undrained shearing is slightly larger than that in the drained test (for the same level of shear stress). However for t = 12 MPa, drained and undrained effective stresses become equal and then further in loading the latter one becomes slightly smaller than the corresponding effective mean stress for the drained test (Figure 4.22).

The increasing mean stress leads to the specimens' compaction (the sign convention is compression positive) before they dilate, and their dilatancy is accompanied by approximately constant AE rate in both drained (Figure 4.23) and undrained (Figure 4.24) experiments. It should be noted that undrained deformation of water-saturated soil is usually considered to preserve the volume of the specimen constant (Terzaghi 1943), because the bulk modulus of a soil (order of MPa) is much smaller than the bulk modulus of water (K_{water} = 2.24 GPa), which means that it takes most of the load. However, in the undrained testing of porous rock, its bulk modulus is on the same order or higher than water ($K_u \sim K_f$), and hence rock's stiff framework feels the applied load at least as much as the pore fluid and deforms. Because the applied effective mean stress was significantly larger in undrained compression, this specimen compacted twice as much as the drained one.

It is also observed that in the undrained test, pore pressure is increasing from 2.8 to 7.2 MPa when the sandstone is compacting (Figure 4.25), and it starts decreasing only when the deformation of the specimen becomes inelastic (volume strain response deviates from linearity). However, the pore pressure is still larger at the peak load than its initial value, because the undrained specimen compacts more than it dilates prior to failure.

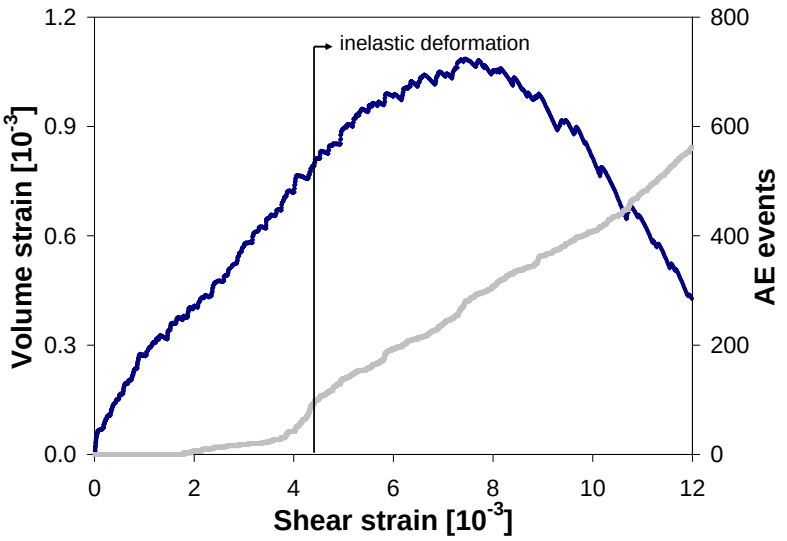

Figure 4.23: Volume strain and AE for the plane strain drained test.

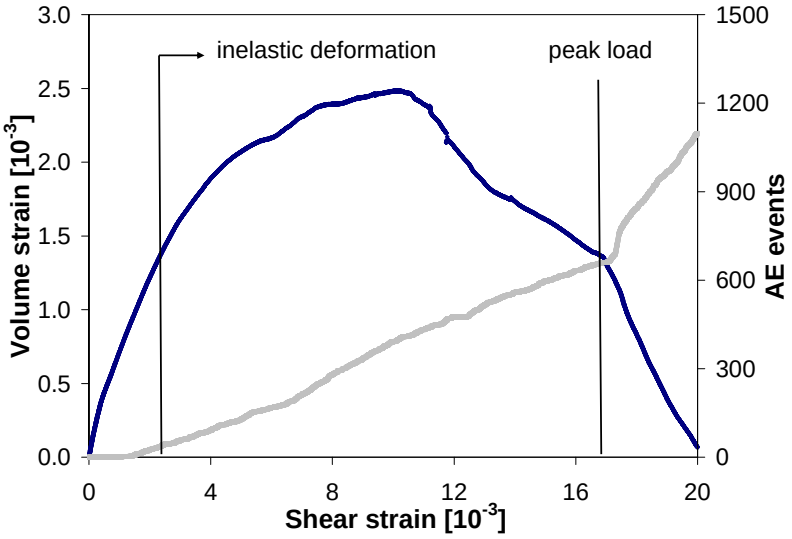

Figure 4.24: Volume strain and AE for the plane strain undrained test.

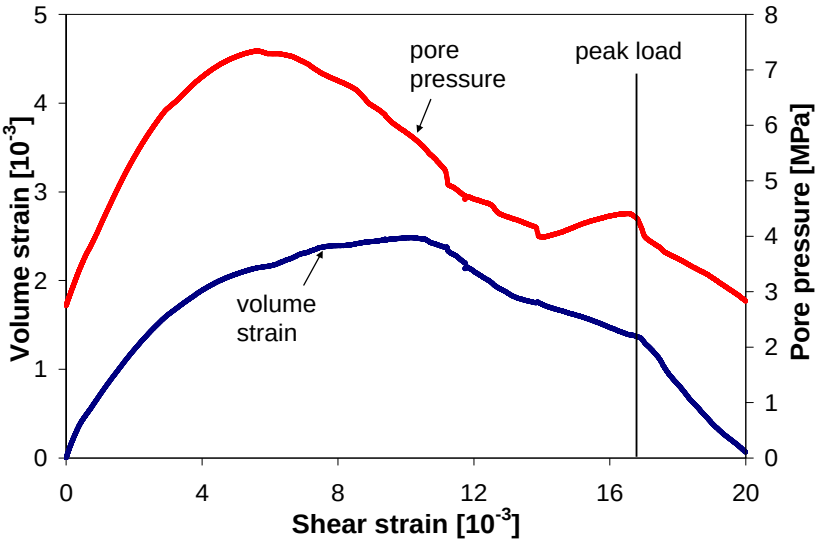

Figure 4.25: Volume strain and pore pressure for the plane strain undrained test.

4.5.2 Hardening parameters

To compare the undrained behavior with the constitutive model prediction, the hardening parameters such as friction coefficient μ, dilatancy factor β, and effective bulk modulus K_{eff} need to be calculated from the corresponding drained test.

Dilatancy factor

The measured principal strains contain both elastic and plastic components. The onset of the nonlinear response was used as a benchmark signifying when plastic deformation initiated (Figure 4.23). The plastic strains were determined by removing the calculated elastic response from the measured deformation assuming no change in elastic parameters (Riedel and Labuz 2007):

$$\Delta\varepsilon^{p} = \Delta\varepsilon^{meas} - \Delta\varepsilon^{e} \tag{4.16}$$

$$\Delta\gamma^{p} = \Delta\gamma^{meas} - \Delta\gamma^{e} \tag{4.17}$$

For the drained test conducted at 5.5 MPa effective cell pressure, plastic deformation was only associated with a dilatant response (Figure 4.26). The increase of plastic volume strain was fairly linear from the onset of inelasticity up to the peak. The dilatancy factor can be calculated from

$$\beta = \sin\psi = -\frac{\Delta\varepsilon^p}{\Delta\gamma^p} \tag{4.18}$$

where ψ is the dilatancy angle (Hansen 1958) and it is presented in Figure 4.26. It can be seen that even though the data are scattered, for $\gamma^p > 0.5\times10^{-3}$, the dilatancy angle of the sandstone becomes approximately constant and equal to 24°. Hence, the dilatancy factor β can be taken as a constant value $\beta = \sin 24° \approx 0.41$.

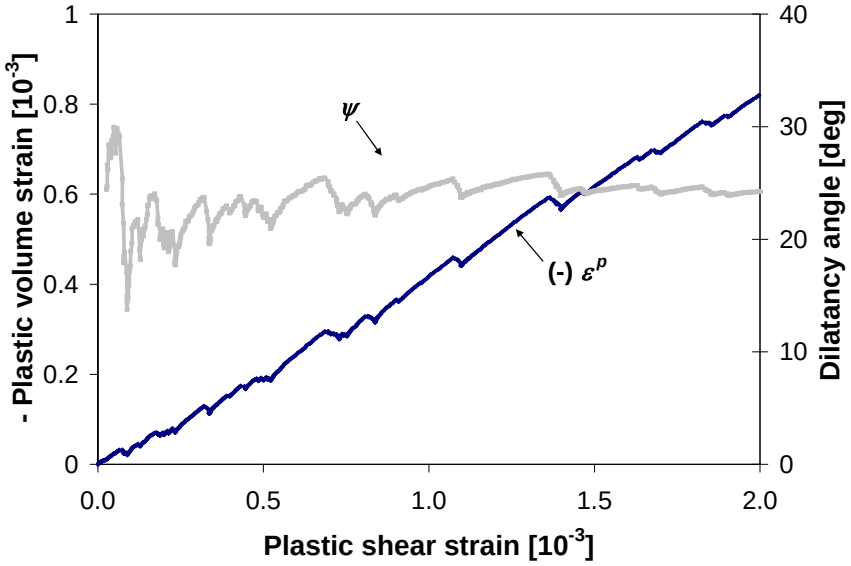

Figure 4.26: Plastic volume strain and dilatancy angle after the onset of inelastic deformation.

Friction coefficient

The Mohr-Coulomb linear yield function can be written as (Riedel and Labuz 2007)

$$\sin\varphi = \frac{\sigma_1 - \sigma_3}{\sigma_1 + \sigma_3 + 2V_o} \tag{4.19}$$

where φ is the friction angle and the parameter V_o the uniform triaxial tensile strength V_o was determined from the linear failure criterion (Figure 4.3).

The friction coefficient μ, which is used in the dilatant hardening model, can be written as

$$\mu = \tan\varphi \tag{4.20}$$

We are interested in behavior of μ only for inelastic deformation, so it can be presented as a function of plastic shear strain γ^p (Figure 4.27). It appears that the friction coefficient μ is approximately constant throughout the inelastic deformation process, and it is taken as $\mu = 1.2$ in the calculation of the dilatantly hardened response.

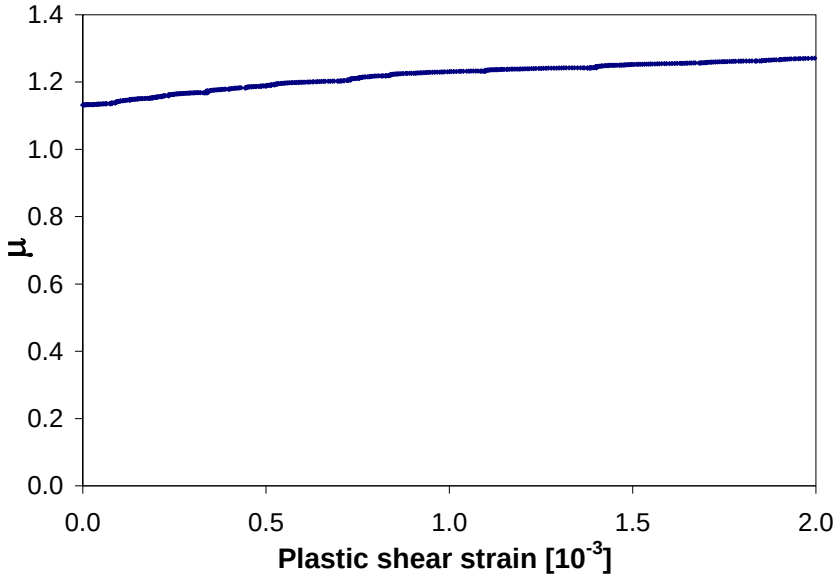

Figure 4.27: Development of the friction parameter μ in plane strain drained experiment.

Effective bulk modulus K_{eff}

K_{eff} is the parameter that links the poroelastic response of the material with the dilatant hardening model. To calculate K_{eff}, the change in the porosity $\Delta\phi = \phi - \phi_o$ during deformation needs to be determined. From equation (2.89), it can be seen that $\Delta\phi$ has "stress" in the numerator with order of MPa, and poroelastic bulk moduli in the denominator with order of GPa. Hence $|\Delta\phi| < 0.01$ and is on the order of the accuracy of the porosity measurements, so it can be neglected. Then, the equation (2.92) can be simplified and K_{eff} is expressed in terms of the Skempton B coefficient:

$$K_{eff} = \frac{BK}{\alpha} \tag{4.21}$$

Substituting the reported values for poroelastic parameters into (4.21), we obtain K_{eff} = 7.9 – 9.5 GPa, with the average value of 8.7 GPa.

The inelastic hardening modulus H can be calculated from inelastic incremental shear stress – shear strain behavior and shear modulus G = 4.2 GPa:

$$H = \frac{1}{\frac{\Delta\gamma}{\Delta t} - \frac{1}{G}} \tag{4.22}$$

The data were recorded every second, which means that H can be calculated for each $\Delta\gamma = 0.007\times10^{-3}$ increment of shear strain (the shear strain rate was approximately constant during the test). To describe the corresponding undrained response, increments of shear stress are calculated from equation (2.93) by substituting the previously obtained values of G, μ, β, K_{eff} = 8.7 GPa (constants), and H. The results of the drained and undrained tests, along with the constitutive model prediction, are presented in Figure 4.28.

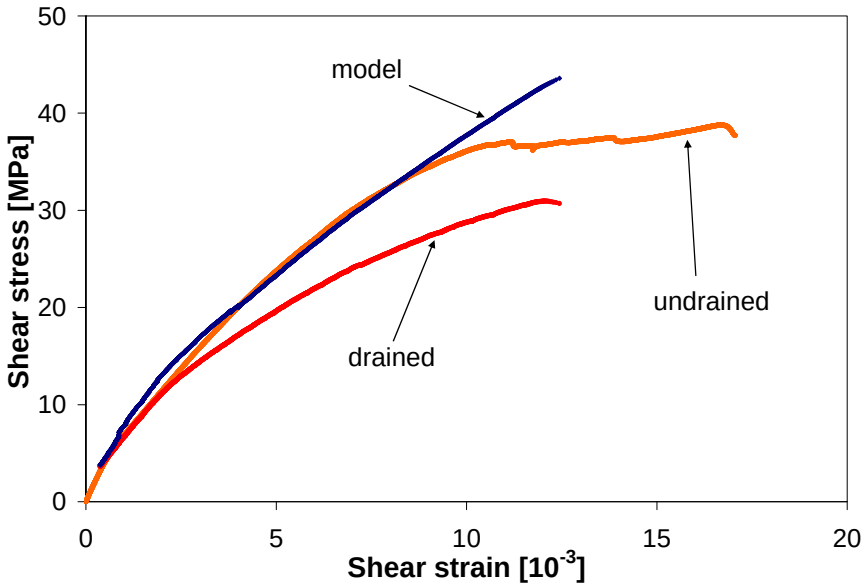

Figure 4.28: Results of the plane strain tests and the model prediction for undrained behavior.

The response predicted by the model is slightly stiffer than the experimental undrained response at the beginning of loading ($\gamma < 3.8\times10^{-3}$). At higher shear stresses, the model predicts undrained behavior fairly well up to the 90% of maximum shear stress. In the

final region of undrained inelastic deformation, increase of axial stress "tries" to facilitate failure but the increase of the effective confinement due to dilatancy delays it. The presence of these two competing factors explains why it takes about the half of the total shear strain ($\Delta\gamma \sim 8\times10^{-3}$) to bring the specimen from 90% of the peak stress to failure.

However, most of the results of plane strain experiments with constant cell pressure are not consistent in terms of undrained response being hardened with respect to the drained one. Based on volume strain data, it can be concluded that it is related to the changing mean stress, which makes rock specimens compacting during elastic deformation by the larger amount than they dilate later, when the response becomes inelastic.

4.5.3 Compression with constant mean stress

Cylindrical specimens were tested in conventional triaxial compression under drained and undrained conditions, where $P = (\sigma_a + 2\sigma_r)/3 = \text{const}$ can be preserved by applying increments of $\Delta\sigma_a > 0$ (axial strain rate $\sim 10^{-6}$ s^{-1}) and decreasing the radial stress (cell pressure) by $\Delta\sigma_r = -\Delta\sigma_a/2 < 0$. The stress path for this type of loading can be plotted in the principal stress space along with the six-sided failure surface (Figure 4.29) determined in section 4.1.2.

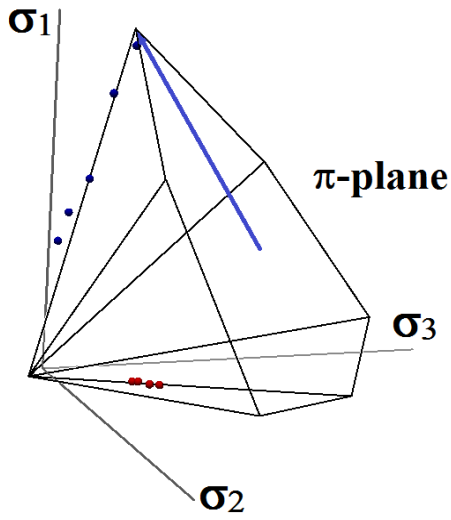

Figure 4.29: Six-sided failure surface and the stress path preserving constant $P = 20$ MPa in the principal stress space.

A drained conventional triaxial experiment was performed under the conditions of P = const = 20 MPa and p = const = 3 MPa. The initial mean stress was significantly larger than the one used in the plane strain compression test reported in the previous section, because the failure of the specimen for the case of constant mean stress loading can be assured only if $P' = P - p >$ UCS/3 ≈ 15 MPa is used. The development of principal stresses in the triaxial drained experiment is shown in Figure 4.30. The specimen failed at σ_1 = 51 MPa and $\sigma_2 = \sigma_3$ = 4.5 MPa. The results of the drained test in terms of volume strain, AE activity, and pore pressure are presented in Figure 4.31.

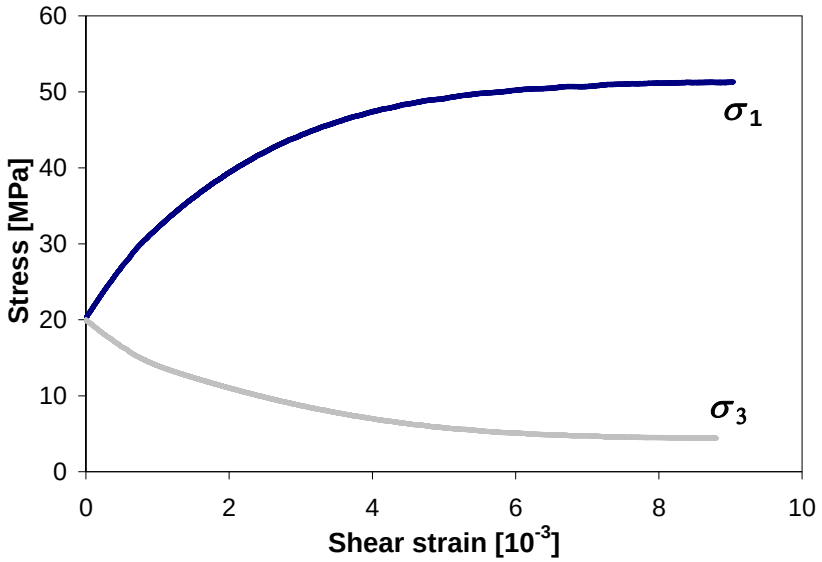

Figure 4.30: Principal stresses in triaxial drained test conducted at P = const = 20 MPa.

Monotonically decreasing volume strain indicates that the drained specimen started dilating from the beginning of the deviatoric loading. It is also confirmed by the AE activity and the observations from initial loading – unloading procedure, which indicated the presence of permanent strain. For the case of constant P, there should be no elastic volume change: $\Delta\varepsilon^e = 0$ and $\Delta\varepsilon^p = \Delta\varepsilon^{meas}$ because only a change in P produces elastic volume strain. An increment of shear strain consists of elastic and plastic parts; hence $\Delta\gamma^p = \Delta\gamma^{meas} - \Delta\gamma^e$. Then, friction coefficient μ and dilatancy factor β can be calculated for this loading condition using the method described in section 4.5.2 (Figure 4.32).

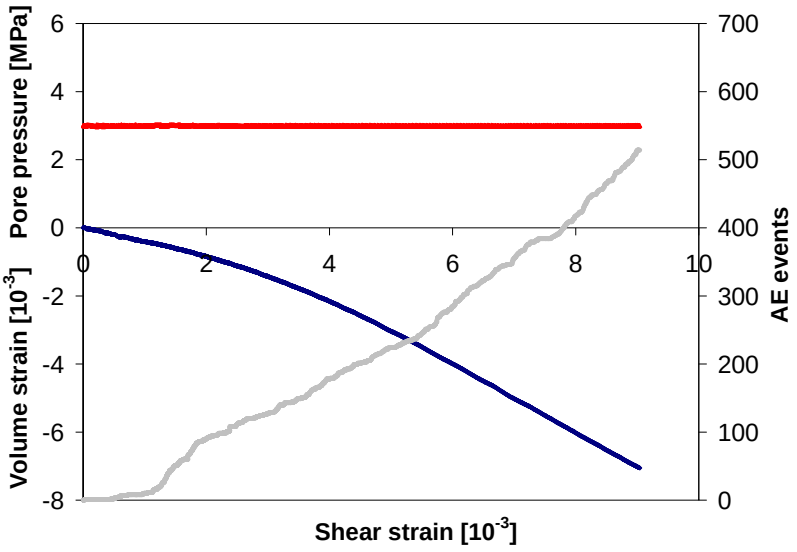

Figure 4.31: Volume strain, pore pressure, and AE in conventional triaxial drained test.

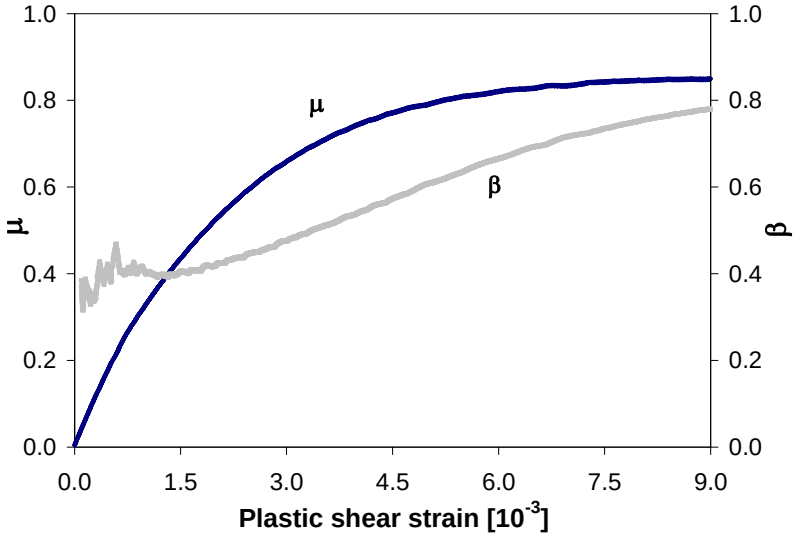

Figure 4.32: Development of friction coefficient μ and dilatancy factor β in the triaxial drained test.

Friction coefficient was found to be monotonically increasing, being equal to 0 at the beginning of deviatoric loading and 0.85 at the peak stress, which is smaller than $\mu \approx 1.2$ measured in the plane strain test. Dilatancy factor was sensitive to the initial fluctuations in ε^p and then ($\gamma^p > 10^{-3}$) monotonically increased to 0.78.

The effective bulk modulus K_{eff} also is recalculated for the state of stress, $P = 20$ MPa and $p = 3$ MPa. The specimen was found to be fully saturated at $P' = 17$ MPa when the back pressure exceeded 3 MPa and the maximum Skempton coefficient was $B = 0.38$ (Figure 4.13). Drained bulk modulus was measured to be $K = 11.3$ GPa and shear modulus was taken as the initial slope of shear stress – shear strain curve: $G = 9.0$ GPa. Taking unjacketed bulk modulus (independent of the mean stress) as $K_s' = 30$ GPa and $\alpha = 0.62$, $K_{eff} = 6.9$ GPa is calculated.

All the parameters that characterize the hardening undrained response are now available. To evaluate the goodness of the model prediction, the undrained conventional triaxial test was performed with the same initial conditions as the drained test: $P = \text{const} = 20$ MPa and $p_o = 3$ MPa. In this test, mass of the fluid inside the specimen was kept constant, so the pore pressure was allowed to change. During the test, p decreased from 3 MPa to 0.5 MPa, which produced the increase in effective mean stress and delayed the specimen failure to the point where $\sigma_1 = 55.2$ MPa and $\sigma_2 = \sigma_3 = 2.4$ MPa. The development of the volume strain, AE activity, and pore pressure with shear strain in undrained conventional triaxial compression is presented in Figure 4.33.

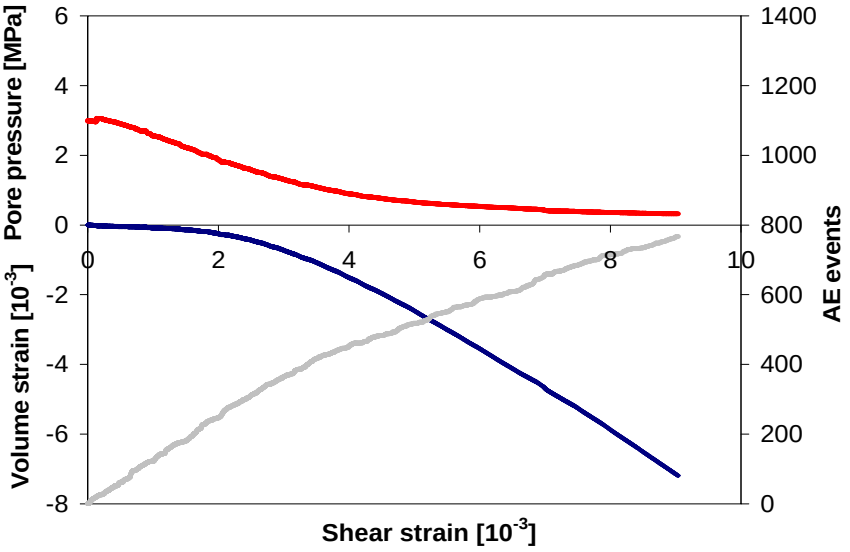

Figure 4.33: Volume, pore pressure, and AE in triaxial undrained experiment with constant $P = 20$ MPa.

Similar to the drained condition, in the undrained test conducted at constant mean stress, no initial compaction was observed and the specimen dilated by approximately the same amount. AE activity was observed from the beginning of deviatoric loading, which confirmed the inelastic nature of the undrained deformation. It also should be mentioned that both drained and undrained conventional triaxial tests were stopped soon after peak load was reached. A localized failure plane was not visible in the specimens, and nothing can be stated on the possible differences between types of failure under two limiting rock-fluid interaction conditions.

Moreover, an undrained plane strain experiment was conducted preserving P = const = 20 MPa and the same initial pore pressure p_o = 3 MPa. Using equation (3.14) and neglecting the deformation of the prismatic specimen in the intermediate principal stress direction ($\varepsilon_2 = 0$), the following relationship can be written for the mean stress:

$$P = (\sigma_1 + \sigma_2 + \sigma_3)/3 = (1 + \nu_u)(\sigma_1 + \sigma_3)/3 \tag{4.23}$$

Therefore, when applying axial stress ($\Delta\sigma_1 > 0$) to the specimen, σ_3 has to be preserved as

$$\sigma_3 = 3P/(1 + \nu_u) - \sigma_1 \tag{4.24}$$

and ν_u was measured to be 0.35. The undrained plane strain compression test was stopped at σ_1 = 43.6 MPa, σ_2 = 15.6 MPa, σ_3 = 0.8 MPa, and p = 0.7 MPa. The specimen did not fail at this point, but the condition of $\sigma_3' = \sigma_3 - p \leq 0$ was avoided. The results of this test in terms of volume strain, AE activity, and pore pressure are presented in Figure 4.34. Volume strain and pore pressure response in the plane strain test is observed to be similar to the conventional triaxial test, even though the change in their values is smaller. It happens because the plane strain test was stopped at significantly smaller shear strain compared to conventional triaxial test.

Results of the drained and two undrained experiments conducted at P = const = 20 MPa and the constitutive model prediction are presented in Figure 4.35.

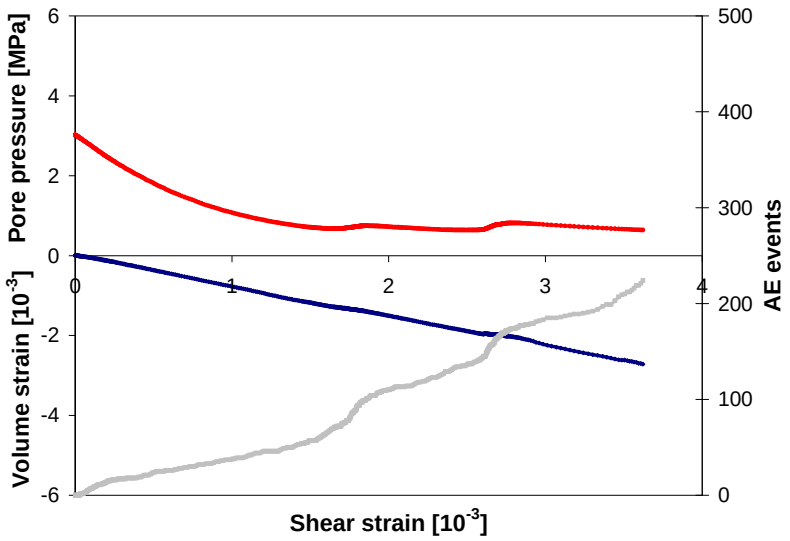

Figure 4.34: Volume, pore pressure, and AE in plane strain undrained experiment with constant $P = 20$ MPa.

The constitutive model predicts the undrained behavior of fluid-saturated sandstone up to 95% of the peak axial stress. From this point, each increment of shear strain requires much larger increment in shear stress compared to the beginning of loading. This behavior is not captured by the model, which still can be treated as a good first order approximation to the inelastic behavior of fluid-saturated porous rock.

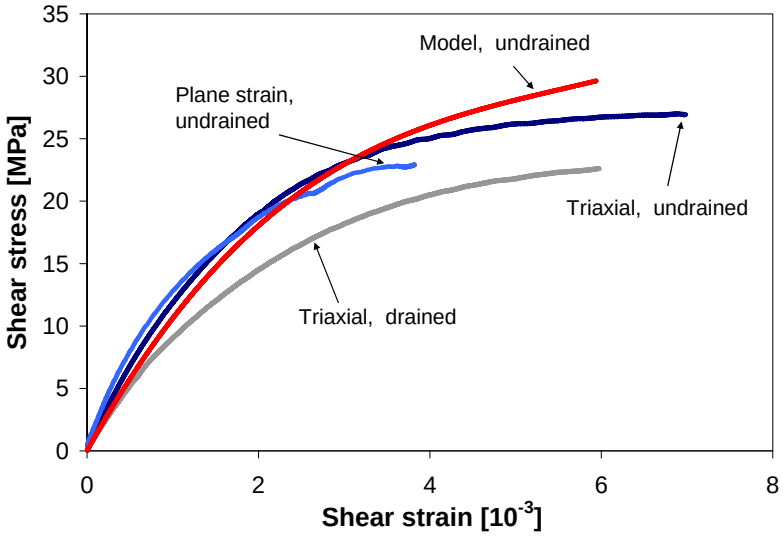

Figure 4.35: Results of the experiments and the model prediction for the undrained behavior.

Chapter 5

Conclusions and Future Work

Experimental techniques were developed to characterize the deformation of fluid-saturated porous rock. The methods to achieve full saturation of laboratory specimens and accurately determine applied loads and produced deformations were suggested and successfully implemented.

A series of hydrostatic, plane strain, and conventional triaxial compression tests were performed on water-saturated Berea sandstone. The poroelastic behavior of the rock was investigated at 5 MPa effective mean stress. Skempton and Biot coefficients and drained and undrained bulk moduli were measured. The response of the material under undrained conditions was found to be stiffer than the drained one. Also, two bulk moduli associated with the unjacketed material behavior were evaluated. Unjacketed bulk modulus K_s' was directly measured and found to be 30 GPa, which is 20% lower than that usually assumed equal to its dominant mineral (quartz) bulk modulus. Microphotograph analysis showed that it can be explained by the presence of non-connected pore space in the rock. Unjacketed pore volume bulk modulus K_s'' was not measured directly, but calculated from the poroelastic relations. It was found to be strongly influenced by the stress-dependent deformation of the rock at low effective mean stresses ($P' \sim 5$ MPa), but achieved a more reliable value of 18 GPa when calculated from data obtained at $P' = 17$ MPa.

Additionally, the rock was treated as a transversely isotropic material and related drained and undrained parameters were measured. Undrained poroelastic response of Berea sandstone was well predicted by the transversely isotropic model in terms of Biot coefficient α' and the components of the stiffness matrix. However, the large difference between Skempton B coefficients measured due to the loading applied along the bedding planes and perpendicular to them was not captured by the model.

The results of drained and undrained plane strain and conventional triaxial compression experiments were discussed in the framework of an elasto-plastic, dilatant hardening constitutive model. The parameters that govern the inelastic deformation of fluid-saturated rock, *i.e.* dilatancy angle β, friction coefficient μ, poroelastic coefficient K_{eff}, shear modulus G, and inelastic hardening modulus H, were calculated from the drained response. In the case of plane strain testing with constant minimum principal stress, the constitutive model predicts the undrained inelastic behavior of the rock fairly well, almost up to the peak axial stress if compared with the undrained test that had the same

effective mean stress at the onset of inelasticity. If the mean stress is preserved constant during the test, then the model prediction based on the drained conventional triaxial experiment is found to be consistent with the results of two undrained tests, one conventional triaxial and one plane strain compression.

To summarize, the main contributions of this thesis are:

1. development of a linear failure criterion with three different principal stresses;
2. independent measurement of a number of poroelastic parameters by various experimental methods;
3. measurement of the overdetermined set of transversly isotropic poroelastic parameters;
4. characterization of the inelastic response of porous rock under different drainage conditions.

Future work should involve the direct measurement of the unjacketed pore volume bulk modulus K_s''. A variation of the pore volume should be measured accurately. An apparatus should have a precisely known external storage tank so that variation of volume and fluid pressure in the apparatus could be accurately related to variation of the pore space in the rock. Because this measurement is technically very difficult, no direct measurements have been made (up to date) to obtain K_s''. Accurate measurements of K_s'' along with the more detailed analyses of the nature of non-connected pore space can be used to characterize the microporomechanical behavior.

Furthermore, the proposed experimental techniques can be utilized for testing some rock from the field, for example shales (Makhnenko *et al.* 2011). Also, characterization of the interaction between sedimentary rock and pore fluid can be critical for safe CO_2 storage. Some studies (*e.g.* Oye *et al.* 2012) show that the injection of gas into the sandstone aquifer can cause its inelastic deformation accompanied by seismicity. So the proposed experimental methods can be used to obtain the parameters governing this behavior.

References

Abousleiman, Y., A. H.-D. Cheng, L. Cui, E. Detournay, and J.-C. Roegiers. 1996. Mandel's problem revisited. *Geotechnique,* 46:187-195.

Aldrich, M.J. 1969. Pore pressure effects on Berea sandstone subjected to experimental deformation. *Geol. Soc. Am. Bull.,* 80:1577-1586.

Al-Hussaini, M.M. 1968. The behavior of sand under plane strain conditions. Ph.D. dissertation, Georgia Institute of Technology.

Allen, N.F., F.E. Richart, Jr., and R.D. Woods. 1980. Fluid wave propagation in saturated and nearly saturated sands. *J. Geotech. Eng. Division, ASCE*. 106:235-253.

Ask, D., O. Stephansson, F.H. Cornet, and M.V.S. Ask. 2009. Rock stress, rock stress measurements, and the integrated stress determination method (ISDM). *Rock Mech. Rock Eng.*, 42:559-584.

Bardet, J.P. and H. Sayed. 1993. Velocity and attenuation of compressional waves in nearly saturated soils. *Soil Dyn. Earthquake Eng.,* 12: 391-401.

Berchenko, I., E. Detournay, N. Chanler, and J. Martino. 2004. An in-situ thermo-hydraulic experiment in a saturated granite I: design and results. *Int. J. Rock Mech. Min. Sci.*, 41 (8):1377-1394.

Berge, P.A., H.F. Wang, and B.P. Bonner. 1993. Pore pressure buildup coefficient in synthetic and natural sandstones. *Int. J. Rock Mech. Min. Sci. & Geomech. Abstr.* 30(7): 1135-1141.

Berryman, J.G. 2005. Poroelastic fluid effects on shear for rocks with soft anisotropy. *Geophys. J. Int.*, 161:881-890.

Bésuelle, P., and S.A. Hall. 2011. Characterization of the strain localization in a porous rock in plane strain condition using a new true-triaxial apparatus. In *Advances in bifurcation and degradation in geomaterials*, eds. S. Bonelli, C. Dascalu, and F.Nicot. Springer, 345-352.

Biot, M.A. 1935. Le problème de la consolidation des matières argileuses sous une charge. *Ann. Soc. Sci. Bruxelles*, B55:110-113.

Biot, M.A. 1941. General theory of three-dimensional consolidation. *J. Appl. Phys.,* 12: 155-164.

Biot, M.A. 1955. Theory of elasticity and consolidation for a porous anisotropic solid. *J. Appl. Phys.,* 26: 182-185.

Biot, M.A. 1956. Theory of propagation of elastic waves in a fluid saturated porous solid, parts I and II. *J. Acoust. Soc. Am*., 28(2):168-191.

Biot, M.A., D.G. Willis. 1957. The elastic coefficients of the theory of consolidation. *J. Appl. Mech., Trans. ASME*, 79:594-601.

Biot, M.A. 1973. Nonlinear and semilinear rheology of porous solids. *J. Geophys. Res.*, 78:4924-4937.

Bishop, A. W. 1973. The influence of an undrained change in stress on the pore-pressure in porous media of low compressibility. *Geotechnique*, 23(3): 435–442.

Bishop, A. W. 1976. Influence of system compressibility on observed pore pressure response to an undrained change in stress in saturated rock. *Géotechnique*, 26(2):371-375.

Black, D.K. and K.L. Lee. 1973. Saturating laboratoty samples by back pressure. *J. Soil Mech. & Found. Division, ASCE*. 99:75-93.

Blöcher, G., D. Bruhn, G. Zimmerman, C. McDermott, and E. Huenges, E. 2007. Investigation of the undrained poroelastic response of sandstones to confining pressure via laboratory experiment, numerical simulation and analytical calculation. In *Rock Physics and Geomechanics in the Study of Reservoirs and Repositories*, eds. C. David and M. Le Ravalec-Dupin, The Geological Society, 284:71-87.

Boussinesq, J.V. 1885. Sur l'integration par approximations successive d'une equation… don't dependent les pressions intérieurs d'un massif des sable á l'état ébouleux. In *Application des potentials á l'étude de l'equilibre et du movement des solides élastiques, Gauthier-Villas*, 27:705-712.

Boutéca, M., J.P. Sarda, and J. Laurent. 1991. Rock mechanics contribution to the determination of fluid flow properties. In *Proceedings of 2nd Symposium on Core Analysis*, 239-253.

Brace, W.F. and R.J. Martin. 1968. A test of the law of effective stress for crystalline rocks of low porosity. *Int. J. Rock Mech. & Mining Sci.*, 5:415-436.

Brace, W.F., B.W. Paulding, and C. Scholz. 1966. Dilatancy in the fracture of crystalline rocks. *J. Geophys. Res*., 71(16):3939-3953.

Brown, E.T. 1981. *Rock Characterization, Testing and Monitoring: ISRM Suggested Methods.* International Society for Rock Mechanics, Pergamon Press.

Brown, R. J. and J. Korringa. 1975. On the dependence of the elastic properties of a porous rock on the compressibility of the pore fluid. *Geophysics*, 40:608–616.

Campanella, R.G. and Y.P. Vaid. 1973. Influence of stress path on the plane strain behavior of sensitive clay. In *Proceedings of 8th Int. Conf. Soil Mech. Found. Engng.,* 1:85-92.

Carvalho, F. and J.F. Labuz. 2002. Moment tensors of acoustic emission in shear faulting under plane-strain compression. *Tectonophysics,* 356:199-211.

Chaney, R.C., E. Stevens, and N. Sheth. 1979. Suggested test method for determination of degree of saturation of soil samples by *B* value measurement. *Geotech. Testing J.,* 2(3):158-162.

Cheng, A. H.-D. 1997. Material coefficients of anisotropic poroelasticity. *Int. J. Rock Mech. Min. Sci.,* 34(2):199-205.

Cornforth, D.H. 1964. Some experiments on the influence of strain conditions on the strength of sand. *Geotechnique,* 14(2):143-167.

de Boer, R. 2000. *Theory of porous media: Highlights in historical development and current state.* Springer-Verlag Berlin.

Dehler, W. and J.F. Labuz. 2007. Stress path testing of anisotropic sandstone. *J. Geotech. Geoenviron. Eng.,* 133:116-119.

Detournay, E., A. Cheng. 1993. Fundamentals of poroelasticity. In *Comprehensive Rock Engineering, Vol. II,* ed. C. Fairhurst, 113-171.

Dormieux, L., A. Molinari, and D. Kondo. 2002. Micromechanical approach to the behavior of poroelastic materials. *J. Mech. & Phys. Solids,* 50:2203-2231.

Drescher, A., I. Vardoulakis, and C. Han. 1990. A biaxial apparatus for testing soils. *Geotech. Testing J. ASTM,* 13:226-234.

Dullien, F.A.L. 1992. *Porous Media: Fluid transport and Pore Structure, 2nd edn.* Academic Press, London.

Duncan J.M. and H.B. See. 1966. Strength variation along failure surface in clay. *Proceedings ASCE*, 92(SM6):81-104.

Fabre, D. and J. Gustkiewicz. 1997. Poroelastic properties of limestones and sandstones under hydrostatic conditions. *Int. J. Rock Mech. Min. Sci*., 34(1):127-134.

Fatt, I. 1958. The compressibility of sandstones at low to moderate pressures. *Bull. Amer. Ass. Petr. Geol.*, 42(8):1924-1927.

Fatt, I. 1959. The Biot-Willis elastic coefficients for a sandstone. *J. Appl. Mech., Trans. ASME,* 26:296-297.

Fillunger, P. 1915. Versuche über die Zugfestigkeit bei allseitigem Wasserdruck. *Österreichische Wochenschrift für den öffentlichen Baudienst*, 29:443-448.

Frank, F.C. 1965. On dilatancy in relation to seismic sources. *Reviews of Geophysics*, 3 (4): 485-503.

Franklin J.A., and E. Hoek. 1970. Developments in triaxial testing technique. *Rock Mechanics*, 2(4):223-228.

Fredlund, D.G. 1976. Density and compressibility characteristics of air-water mixtures. *Can. Geotech. J.*, 13:386-396.

Gassman, F. 1951. Über die elastizität poröser medien. *Vierteljahrsschriftder Naturforschenden Gessellschaft in Zurich*, 96:l–23.

Gassman, F. 2007. On elasticity of porous media (translation of the 1951 paper from the German). In *Classics of elastic wave theory: SEG*, eds. M. A. Pelissier, H. Hoeber, N. van de Coevering, and I. F. Jones, 389–407.

Geertsma, J. 1957. The effect of fluid pressure decline on volumetric changes of porous rocks. *Trans.AIMME*, 210:331-340.

Geertsma, J. 1966. Problems of rock mechanics in petroleum production engineering. In *Proceedings of the 1st Congress of Int. Soc. Rock Mechanics, Lisbon*, 1:585-594.

Ghabezloo, S. and J. Sulem. 2009. Effect of the volume of the drainage system on the measurement of undrained thermo-poro-elastic parameters. *Int. J. Rock Mech. Min. Sci*., 47:60-68.

Christensen, N.I., and H.F. Wang. 1986. The influence of pore pressure and confining pressure on dynamic elastic properties of Berea sandstone. *Geophysics*, 50:207-213.

Green, D.H. and H.F. Wang. 1986. Fluid pressure response to undrained compression in saturated sedimentary rock, *Geophysics*, 51:948–956.

Haimson, B. 1978. The hydrofracturing stress measuring method and recent field results. *Int. J. Rock Mech. Min. Sci. & Geomech. Abstr*., 15(4):167-178.

Haimson, B., and C. Chang. 2000. A new true triaxial cell for testing mechanical properties of rock, and its use to determine rock strength and deformability of Westerly granite. *Int. J. Rock Mech. Min. Sci*., 37:285-296.

Haimson, B.C., and C. Fairhurst. 1969. Hydraulic fracturing in porous-permeable materials. *J. Pet. Technol*., 21:811-817.

Hall, H.N. 1953. Compressibility of reservoir rocks. *Trans. AIME*, 198:309-311.

Han, D., and M.L. Batzle. 2004. Gassmann's equation and fluid-saturation effects on seismic velocities. *Geophysics,* 69(2):398-405.

Hansen, B. 1958. Line ruptures regarded as narrow rupture zones: basic equations based on kinematic considerations. In *Proceedings of the Conference on Earth Pressure Problems, Brussels, Belgium*, 1:39-49.

Hart, D.J. and H.F. Wang. 1995. Laboratory measurements of a complete set of poroelastic moduli for Berea sandstone and Indiana limestone. *J. Geophys. Res.,* 100:17,741–17,751.

Hart, D.J. and H.F. Wang. 2010. Variation of unjacketed pore compressibility using Gassmann's equation and an overdetermined set of volumetric poroelastic measurements. *Geophysics*, 75:9-18.

Hashin, Z., and S. Shtrikman. 1961. Note on variational approach to the theory of composite elastic materials. *J. Franklin Inst.*, 271:336-341.

Henkel, D.J. 1960. The shear strength of saturated remoulded clays. In *Proceedings of the ASCE Research Conference on Shear Strength of Cohesive Soils*, 533-554.

Henkel, D.J. and N.H. Wade. 1966. Plane strain tests on a saturated remolded clay. *J. Soil Mech. Found. Engng. ASCE*, 92(SM6):67-80

Hughes D.S. and C.E. Cook Jr. 1953. The effect of pressure on the reduction of pore volume of consolidated sandstones. *Geophysics*, 18:298-309.

Ince, N.F., C.-S. Kao, M. Kaveh, A. Tewfik, and J.F. Labuz. 2009. Averaged acoustic emission events for accurate damage localization. In *Proceedings of IEEE International Conference on Acoustics, Speech and Signal Processing, 2009.*

Jaeger, J.C., and N.G.W. Cook. 1976. *Fundamentals of Rock Mechanics*. John Wiley, New York.

Katsube, N., and M.M. Carroll. 1987. The modified mixture theory for fluid-filled porous materials: theory. *J. Appl. Mech*., 54:35-40.

Kjellman, W. 1936. Report on an apparatus for consummate investigation of the mechanical properties of soil. In *Proceedings of the 1st Int. Conf. Soil Mech. Found. Engng.* II, 16-20.

Labuz, J.F., and J.M. Bridell. 1993. Reducing frictional constraint in compression testing through lubrication. *Int. J. Rock Mech. Min. Sci. & Geomech. Abst*., 30:451-455.

Labuz, J.F., S.-T. Dai, and E. Papamichos. 1996. Plane-strain compression of rock-like materials. *Int. J. Rock Mech. Min. Sci.,* 33(6):573-584.

Lee, K.L. and D.K. Black. 1972. Time to dissolve air bubble in drain line. *J. Soil Mech. & Found. Division, ASCE*. 98:181-194.

Lei, X., T. Tamagawa, K. Tezuka, and M. Takahashi. 2011. Role of drainage conditions in deformation and fracture of porous rocks under triaxial compression in the laboratory. *Geophys. Res. Letters*, 38, L2430.

Leussink, H. and W. Wittke. 1963. Difference in triaxial and plane strain shear strength. *ASTM Special Publication*, No. 361:77-89.

Lin, Q., J.F. Labuz, and S. Cattaneo. 2010. Digital Image Correlation and the Fracture Process in Rock. In *Proceedings of 44th US Rock Mechanics Symposium and 5th U.S.-Canada Rock Mechanics Symposium, Salt Lake City, 27-30 June 2010.*

Lockner, D.A and S.A. Stanchits. 2002. Undrained poroelastic response of sandstones to deviatoric stress change. *J. Geophys. Res.*, 107:2353-2366.

Lockner, D.A and N.M. Beeler. 2003. Stress induced anisotropic poroelasticity response in sandstone. In *Proceedings of 16th ASCE Engineering Mechanics Conference, Seattle, WA, 16-18 July*.

Loret, B., E. Rizzi, and Z. Zerfa. 2001. Relations between drained and undrained moduli in anisotropic poroelasticity. *J. Mech. Phys. Solids*, 49:2593-2619.

Lowe, J. and T.C. Johnson. 1960. Use of back pressure to increase degree of saturation of triaxial test specimen. In *Proceedings of the ASCE Research Conference on Shear Strength of Cohesive Soils*, 819-836.

Makhnenko, R., and J. Labuz. 2012. Drained and undrained plane strain compression of porous rock. In *Proceedings of XXIII ICTAM, Beijing, China, 19-24 August 2012*, paper No. FS10-020.

Makhnenko, R.Y., J.J. Riedel, and J.F. Labuz. 2011. Undrained plane strain compression of shale. In *Proceedings of 45th US Rock Mechanics/Geomechanics Symposium, San Francisco, 26-29 June 2011.*

Marsal, R.J., L.R. DeArellano, and G.A. Nunez. 1967. Plane strain testing of rockfill materials. In *Proceedings of 3rd Pan-American Conference on Soil Mech. and Found. Engng.*, 1:249-270.

Mesri, G. K., K. Adachi, and C.R. Ullrich. 1976. Pore-pressure response in rock to undrained change in all-round stress. *Geotechnique,* 26(2):317–330.

Meyer, J.P. 2012. Linear failure criteria with three principal stresses. Master thesis. University of Minnesota.

Meyer, J.P., and J.F. Labuz. 2013. Linear failure criteria with three principal stresses. *Int. J. Rock Mech. Min. Sci.,* 60:180-187.

Mogi, K. 1967. Effect of the intermediate principal stress on rock failure. *J. Geophys. Res.,* 72:5117-5131.

Nur, A. 1972. Dilatancy, pore fluids, and premonitory variations of t_s/t_p travel times. *Bull. Seismol. Soc. Amer.*, 62:1217-1222.

Nur, A. and J.D. Byerlee. 1971. An exact effective stress law for elastic deformation of rock with fluids. *J. Geoph. Res*., 76:6414–6419.

Oye, V., P. Zhao, D. Kühn, K. Iranpour, E. Aker, and B. Bohloli. 2012. Monitoring of the In Salah CO2 storage site (Krechba) using microseismic data analysis. In *Proceedings of 3rd EAGE CO2 Geological Storage Workshop, Edinburgh, 26 -27 March 2012*.

Palciauskas, V.V. and P.A. Domenico. 1982. Characterization of drained and undrained response of thermally loaded repository rocks. *Water Resources Res.,* 18(2):281-290.

Paul, B. 1968. Generalized pyramidal fracture and yield criteria. *Int. J. Solids Struct.,* 4:175-196.

Reynolds, O. 1883. An experimental investigation of the circumstances, which determine whether the motion of water shall be direct or sinuous, and of the law of resistance in parallel channels. *Philosoph. Transact. Royal Society of London*, 174:935-982.

Reynolds, O. 1886. Dilatancy. *Nature*, 33:429-430.

Rice, J.R. 1975. On the stability of dilatant hardening for saturated rock masses. *J. Geophys. Res.,* 80(11):1531-1536.

Rice, J. R. 1977. Pore pressure effects in inelastic constitutive formulations for fissured rock masses. In *Advances in Civil Eng. through Eng. Mech*., *ASCE,* 360-363.

Rice, J.R., and M.P. Cleary. 1976. Some basic stress diffusion solutions for fluid-saturated elastic porous media with compressible constituents. *Rev. Geophys. Space Phys.,* 14:227-241.

Rice, J.R. and J.W. Rudnicky. 1979. Earthquake precursory effects due to pore fluid stabilization of a weakening fault zone. *J. Geophys. Res.,* 84:2177-2194.

Riedel, J.J. and J.F. Labuz. 2007. Propagation of shear band in sandstone. *Int. J. Numer. Anal. Meth. Geomech.,* 31:1281-1299.

Roeloffs, E. 1996. Poroelastic techniques in the study of earthquake-related hydrologic phenomena: *Adv. Geophys.*, 37:135–195.

Rudnicki, J.W. 1985. Effect of pore fluid diffusion on deformation and failure of rock. In *Mechanics of Geomaterials*, ed. Z. P. Bažant, New York: John Wiley & Sons, 315-347.

Scholz, C.H. 1968. Microfracturing and the inelastic deformation of rock in compression. *J. Geophys. Res.*, 73(4):1417-1432.

Scholz, C.H., L.R. Sykes, and Y.P. Aggarwal. 1973. Earthquake prediction: a physical basis. *Science*, 181:803-810.

Schuurman, I.E. 1966. The compressibility of an air/water mixture and a theoretical relation between the air and water pressures. *Geotechnique*, 16(4):269-281.

Skempton, A.W. 1954. The pore-pressure coefficients A and B. *Geotechnique*, 4:143-147.

Skempton, A.W. 1960. Significance of Terzaghi's concept of effective stress (Terzaghi's discovery of effective stress). In *From theory to practice in soil mechanics*, eds. L. Bjerrum, A. Casagrande, R. B. Peck, and A.W. Skempton, Wiley, New York.

Smith, I.M. 1963. An investigation of the strength characteristics of soft clay under condition of plane strain. Graduate research report, University of California, Berkeley.

Strachan, P. 1985. Alternative test method for ensuring full saturation in triaxial samples. *Geotech. Testing J.* 8(1):43-46.

Sulem, J. and H. Ouffroukh. 2006. Hydromechanical behavior of Fontainebleau sandstone. *Rock Mech. Rock Engng*., 39(3):185-213.

Terzaghi, K. 1923. Die berechnung der durchlassigkeitsziffer des tones aus dem verlauf der hydrodynamischen spannungsercheinungen. *Sitzungsber. Akad. Wissen., Wien Math. Naturwiss. Kl. Abt. IIa*, 132:105-124.

Terzaghi, K. 1936. The shearing resistance of saturated soils and the angle between the planes of shear. In *Proceedings of International Conference on Soil Mechanics and Foundation Engineering.* Harvard University Press, Cambridge, Mass., 1:54-56.

Terzaghi, K. 1943. *Theoretical Soil Mechanics.* John Wiley, New York.

Thompson, M., and J.R. Willis. 1991. A reformulation of the equations of anisotropic poroelasticity. *J. Appl. Mech., ASME,* 58:612-616.

van der Kamp, G., and J.E. Gale. 1983. Theory of earth tide and barometric effects in porous formations with compressible grains. *Water Resources Res.*, 19(2):538-544.

Vardoulakis, I. 1996. Deformation of water-saturated sand: I. uniform undrained deformation and shear banding. *Geotechnique*, 46(3):441-456.

Vardoulakis, I. 1996. Deformation of water-saturated sand: II. The effect of pore water flow and shear banding. *Geotechnique*, 46(3):457-471.

Vardoulakis, I.G., and M. Goldscheider. 1981. Biaxial apparatus for testing shear bands in soils. In *Proceedings of the 10th International Conference on Soil Mechanics and Foundation Engineering, Stockholm*, 819-824.

Vardoulakis, I. and D.E. Beskos. 1986. Dynamic behavior of nearly saturated porous media. *Mech. Materials*. 5:87-108.

Verruijt, A. 1969. Elastic storage of aquifers. In *Flow through Porous Media*, ed. R.J.M. De Wiest, 331-376.

Viesca, R. C., E. L. Templeton, and J. R. Rice. 2008. Off-fault plasticity and earthquake rupture dynamics: 2. Effects of fluid saturation. *J. Geophys. Res.*, 113:B09307.

Wang, H.F. 1997. Effects of deviatoric stress on undrained pore pressure response on fault slip. *J. Geophys. Res.*, 102:17,943–17,950.

Wang, H.F. 2000. *Theory of Linear Poroelasticity with Applications to Geomechanics and Hydrogeology*. Princeton University Press.

Wawersik, W.R., L.W. Carlson, D.J. Holcomb, and R.J. Williams. 1997. New method for true-triaxial rock testing. *Int. J. Rock Mech. Min. Sci*., 34 (3-4), paper # 330.

Wissa, A. E. 1969. Pore pressure measurements in saturated stiff soils. *J. Soil Mech. & Found. Division, ASCE*, 95:1063–1073.

Yew, C.H., and P.N. Jogi. 1978. The determination of Biot's parameters for sandstones, Part 1: Static tests. *Exp. Mech*., 18:167-172.

Zimmerman, R.W., W.H. Somerton, and M.S. King. 1986. Compressibility of porous rocks. *J. Geophys. Res.*, 91:12,765–12,777.

Zimmerman, R.W. 1991. *Compressibility of Sandstones*. Elsevier Sci., New York.

Appendices

A. Plane strain testing with passive restraint

A plane strain condition for testing rock is developed through passive restraint in the form of a thick-walled cylinder. The so-called biaxial frame allows the application and measurement of the intermediate principal stress that imposes a triaxial state of stress on a prismatic specimen. Major and minor principal stresses and corresponding strains can be measured, providing data to calculate the elastic (Young's modulus and Poisson's ratio), inelastic (dilatancy angle), and strength (friction angle and cohesion) parameters of the rock. Results of experiments conducted on Indiana limestone in plane strain compression are compared with the results of axisymmetric compression and extension. With proper system calibration, Young's modulus and Poisson's ratio are consistent among the tests. The plane strain apparatus, which enforces in-plane deformation with the three principal stresses at failure being different, allows determination of dilatancy characteristics and fitting of the Paul-Mohr-Coulomb failure surface, which includes an intermediate stress effect.

Introduction

Axisymmetric or "conventional" triaxial testing if often used to determine the elastic and inelastic response of rock, as well as to measure strength characteristics, *e.g.* friction angle and cohesion (Jaeger and Cook 1976). However, questionable predictions may arise when data obtained from axisymmetric tests are applied to two-dimensional models, specifically for those simulating behavior of structures in plane strain. In addition, a number of *in-situ* stress measurements show that principal stresses underground are often not equal (*c.f.* Haimson 1978). Thus, in the investigation of rock failure, the intermediate principal stress effect should be considered (Mogi 1967). A number of true triaxial testing apparatus for rock have been developed in recent years (Wawersik *et al.* 1997; Haimson and Chang 2000; Bésuele and Hall 2011), and these devices rely on some type of piston actively applying an intermediate principal stress. It should be noted that plane

strain apparatus using an active component (a force applied to eliminate displacement) were used in research laboratories of soil mechanics for some time (Kjellman 1936; Leussink and Wittke 1963; Cornforth 1964; Henkel and Wade 1966; Al-Hussaini 1968).

Another approach to plane strain testing is passive restraint, where a stiff structure is used to restrict displacement in one direction (Marsal *et al.* 1967; Campanella and Vaid 1973). A passive device for soil designed by Smith (1963) and modified by Duncan and Seed (1966) relied on bar-type, axial restraint to restrict deformation; for a material such as soil with Young's modulus on the order of MPa, the stiffness requirements of the bars were modest. A clever passive restraint device, also for testing soil, was built by Vardoulakis and Goldscheider (1981). A unique feature of the device was the inclusion of a linear bearing; once deformation localized, the loading platen translated and valuable information was still obtained into the post-peak region with no system interaction (Drescher *et al.* 1990).

A passive restraint system for rock is the University of Minnesota Plane-Strain Apparatus (Labuz *et al.* 1996), which uses a thick-walled cylinder called a biaxial frame for passive restraint and it allows the intermediate stress to be measured. The biaxial frame is sized to ensure that the deformation in the direction of plane strain is below a tolerable amount, *e.g.* one percent of the axial strain. An advantage of a plane strain apparatus is the measurement of in-plane displacements, providing accurate data for determining deformation (shear strain and volume strain) response, and the calculation of elastic and inelastic material parameters.

Biaxial frame

Passive restraint for the University of Minnesota plane-strain apparatus is developed by a thick-walled cylinder (Figure A1) of mild steel called a biaxial frame, which has no seams or interfaces to provide maximum stiffness (Labuz *et al.* 1996). The outside diameter is 300 mm, and the inside diameter is 110 mm; based on a three-dimensional finite element analysis, the out-of-plane strain is about one percent of the axial strain for a rock with Young's modulus E = 15 GPa and cross-sectional area A^s = 2250 mm^2. A circular opening with "flats" (chords of the circular opening) provide precise alignment of the prismatic specimen (Figure A1). A pair of wedges and a corresponding spacer,

such that symmetry is maintained, are used to secure the specimen in the frame and apply a prestress, which is recorded by 120 Ω foil strain gages epoxied to the inside of the biaxial frame.

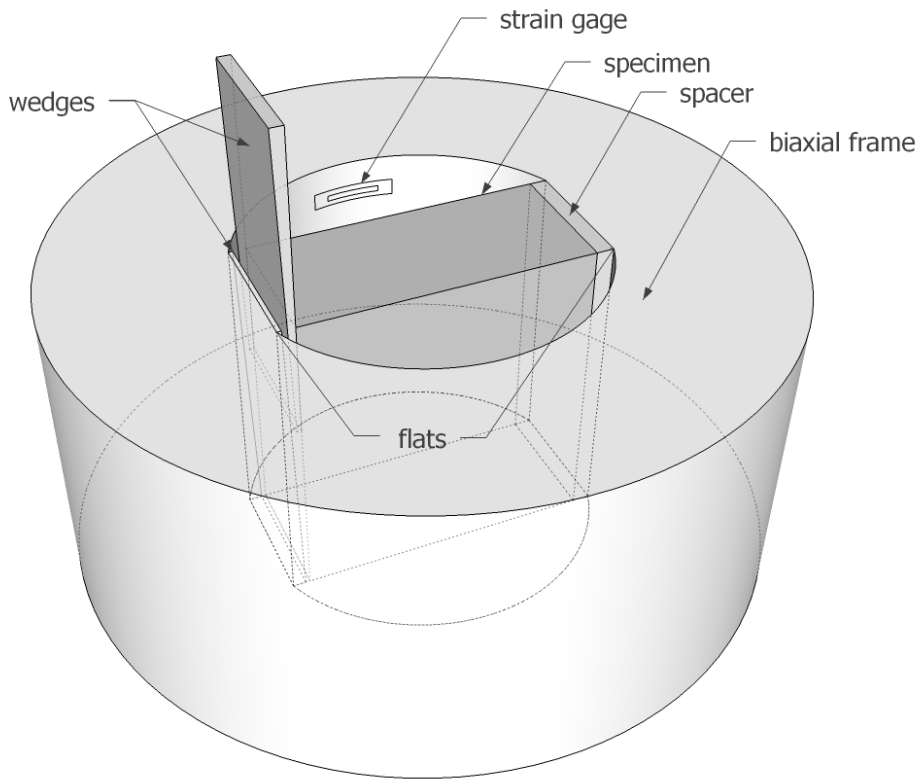

Figure A1: Biaxial frame and specimen installation.

The structural system providing passive restraint can be modeled as a linear spring with stiffness k^f in series with the test specimen (Figure A2):

$$k^f = \frac{F_z^f}{u_z^f} \tag{A1}$$

where u_z^f is the displacement of the frame and F_z^f is the force applied to the specimen-frame interface. For a linearly elastic specimen with Young's modulus E and Poisson's ratio ν, generalized Hooke's law applies:

$$\sigma_{zz} = E\varepsilon_{zz} + \nu(\sigma_{yy} + \sigma_{xx}) \tag{A2}$$

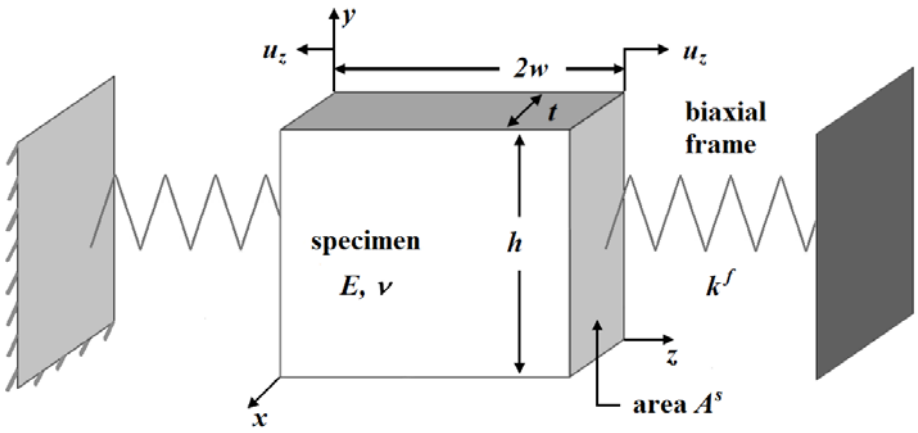

Figure A2: Mechanical model of biaxial frame and specimen interaction.

Force equilibrium, $F_z^f = \sigma_{zz} A^s$, between the frame and the specimen gives

$$k^f u_z^f = A^s (E\varepsilon_{zz} + \nu(\sigma_{yy} + \sigma_{xx})) \tag{A3}$$

where A^s is the cross-sectional area of the specimen (Figure A2) perpendicular to the *z*-axis, the plane strain direction. With perfect contact between the specimen and the frame, specimen deformation u_z^s is equal to the frame deformation:

$$u_z^f = u_z^s = u_z \tag{A4}$$

From the definition of $\varepsilon_{zz} = -u_z / w$ (compressive strain positive) and equation (A3), the displacement u_z can be written as

$$u_z = \frac{wA^s \nu(\sigma_{yy} + \sigma_{xx})}{k^f w - A^s E} \tag{A5}$$

where *2w* is the width of the specimen.

The principal directions are aligned with the Cartesian coordinates: $\varepsilon_1 = \varepsilon_{yy}$, $\varepsilon_2 = \varepsilon_{zz}$, $\varepsilon_3 = \varepsilon_{xx}$ ($\sigma_1 = \sigma_{yy}$, $\sigma_2 = \sigma_{zz}$, $\sigma_3 = \sigma_{xx}$). The frame restricts ε_2 and thus applies the intermediate principal stress σ_2. Deformation of the frame ε^f is monitored by the set of tangentially aligned strain gages glued to the inner wall of the biaxial frame (Figure A1). All strain gages are covered with polyurethane to protect them from the hydraulic oil used for cell pressure.

Calibration tests were performed on three specimen sizes referred to as small, medium, and large (height x thickness = 75 x 28 mm, 87 x 44 mm, and 101 x 40 mm with standard width of 100 mm), and three materials: aluminum (E = 68.9 GPa, ν = 0.33) for a small size specimen, PMMA (E = 3.2 GPa, ν = 0.37) for large and medium sizes, and lead (E = 15.7 GPa, ν = 0.40) for medium size. Calibration specimens were instrumented with 120 Ω foil strain gages oriented to measure ε_1 and ε_2. The calibration tests were performed at 0, 5, 10, and 15 MPa cell pressure, and a typical result is shown in Figure A3; the specimen intermediate strain ε_2 and the deformation of the frame ε_θ^f are linearly related.

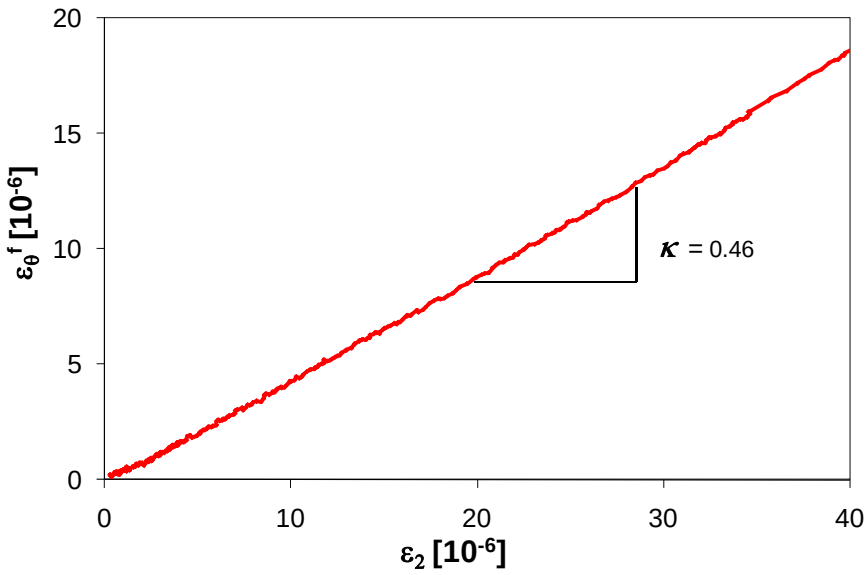

Figure A3: Relationship between frame strain (ε_θ^f) and specimen strain (ε_2) for the small aluminum specimen at 5 MPa cell pressure.

The response shown in Figure A3 can be used to describe the specific strain coefficient of the specimen κ:

$$\kappa\ (A^s, \sigma_3) = \frac{\varepsilon_\theta^f}{\varepsilon_2} \tag{A6}$$

where κ depends on the cross-sectional area of the specimen and cell pressure. Thus, if κ is known, a measure of the plane strain deformation for tests where strain gages on the specimen are not used can be obtained.

The unique relationship, equation (A6), between the specimen strain ε_2 and the frame strain ε_θ^f for a fixed specimen cross-sectional area A^s and cell pressure σ_3 is used to calculate the strain in the rock specimen. Therefore, with known elastic parameters, Young's modulus E and Poisson's ratio v, the intermediate principal stress σ_2 can be determined from equation (A2). Even though inelastic response occurs prior to failure, the elastic parameters in the plane strain direction are not affected appreciably, as microcracks form in the x-y plane of the specimen (Carvalho and Labuz 2002), and this type of damage has no influence on stiffness in the z-direction. During the plane strain compression test performed under constant σ_3 (cell pressure), σ_2 is increasing because of increasing axial stress σ_1 and the frame strain is proportional to ε_2. Passive restraint (the biaxial frame) does not allow the control of the intermediate principal stress, but its value is known and the state of stress is triaxial: $\sigma_1 \neq \sigma_2 \neq \sigma_3$.

Plane strain approximation

Similar to Labuz *et al.* (1996), the degree of plane strain is defined by the ratio

$$R = -\frac{\varepsilon_2}{\varepsilon_1} \tag{A7}$$

Substituting expressions for u_z (equation A5) and ε_1 (generalized Hooke's law) into equation (A7) gives

$$R = \frac{\dfrac{u_z}{w}}{\varepsilon_1} = \frac{\dfrac{A^s \nu(\sigma_1 + \sigma_3)}{k^f w - A^s E}}{\dfrac{1}{E}(\sigma_1 - \nu(\sigma_2 + \sigma_3))} \tag{A8}$$

If the frame is soft, then $k^f \rightarrow 0$ and $\sigma_2 = 0$:

$$R^{soft} = \frac{\nu(\sigma_1 + \sigma_3)}{\sigma_1 - \nu\sigma_3} \tag{A9}$$

The degree of restraint is expressed by the percent plane strain (*PPS*):

$$PPS = \left(1 - \frac{R}{R^{soft}}\right) \times 100\% \qquad \text{(A10)}$$

A summary of the PMMA calibration tests in terms of *PPS* and κ is shown in Fig. 4, where A^s = 3830 *mm* for the medium size specimen and A^s = 4040 *mm* for the large size specimen. While *PPS* = 100% is the case of an ideal plane strain condition (ε_2 = 0), it was shown that *PPS* > 90% is an acceptable approximation (Labuz *et al.* 1996), and the medium size specimen with *E* = 3.2 GPa satisfies this condition. Figure A4 provides the following observations: *PPS* increases with (i) increasing cell pressure, (ii) decreasing Young's modulus *E* (ν = const), and (iii) decreasing specimen area A^s.

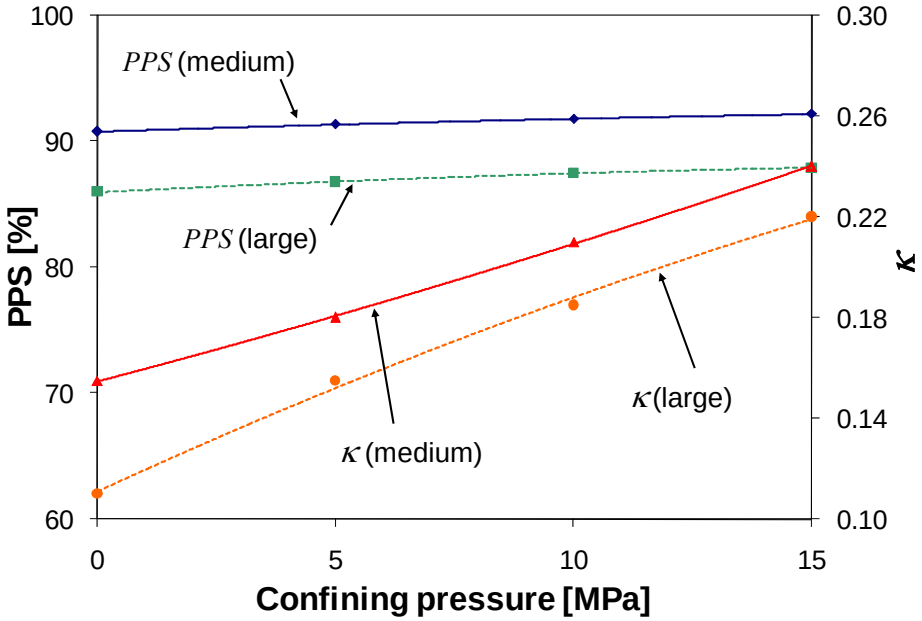

Figure A4: *PPS* and specific frame stiffness κ as functions of confining pressure for medium and large PMMA specimens.

Principal strains

The direction of the major principal stress σ_1 is associated with axial loading, which is measured by upper and lower load cells. Minor principal stress σ_3 is applied by cell pressure (hydraulic oil) and is measured by a pressure transducer. Displacements of the specimen in major (axial) and minor (lateral) principal directions are measured by axial

and lateral LVDTs (Figure A5). However, part of the measured displacement is related to "system" displacement: top and bottom platens attached to the specimen, the internal load cell, and LVDT holders. The system displacement in axial and lateral directions was determined from calibration tests with materials of known elastic properties, such that specimen strains ε_1 and ε_3 can be accurately calculated.

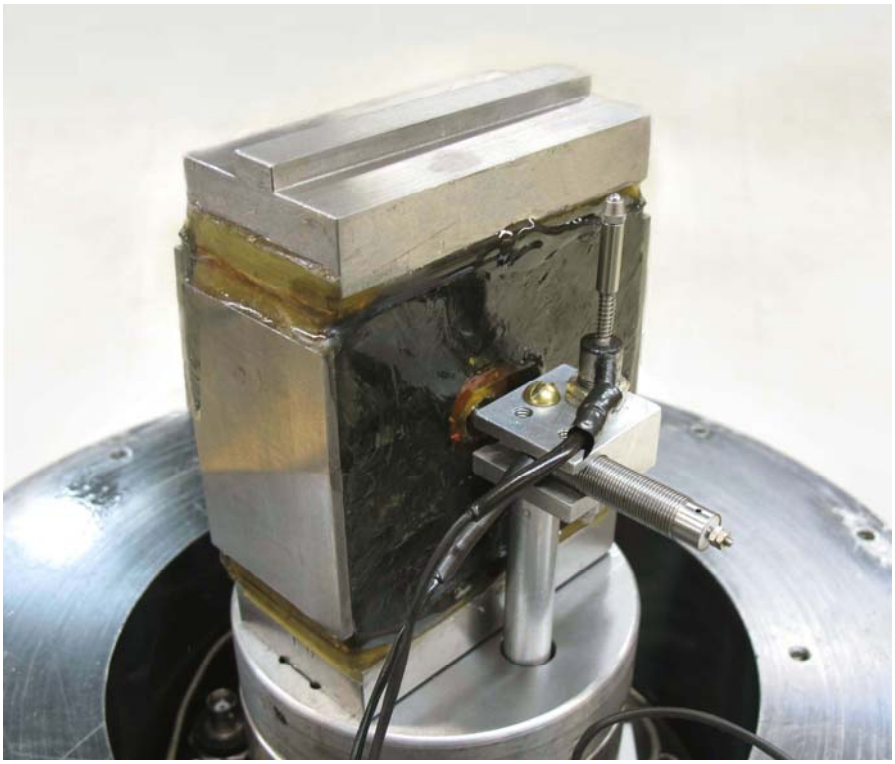

Figure A5: Photograph of the specimen and LVDTs before it is wedged in the frame.

The magnitude of axial system displacement u_1^{sys} is

$$u_1^{sys} = u_1^{LVDT} - \varepsilon_1^{gage} h \tag{A11}$$

where u_1^{LVDT} and $\varepsilon_1^{gage} h$ are the displacement measured with the axial LVDT and the specimen displacement determined from the axial strain gage respectively. It was observed that at low axial loads (< 30 *kN*), a fourth order polynomial is the best fit function to characterize the axial system compliance (Figure A6). However, at higher loads (> 30 *kN*), the dependence of axial system displacement from the load F_1 is linear and can be written as

$$u_1^{sys} = C_A\left(\sigma_3, A^s\right)F_1 \tag{A12}$$

where $C_A(\sigma_3, A^s)$ is the axial system compliance.

Lateral strain cannot be determined from strain gages, as the surfaces of a specimen parallel with the lateral LVDTs are in contact with the biaxial frame (Figure A5), so the lateral specimen strain is calculated with generalized Hooke's law.

Lateral displacement of the system is the difference between the elastic lateral displacement of half of the specimen and the average displacement of two lateral LVDTs:

$$u_3^{sys} = u_3^{LVDT} - \varepsilon_3 t/2 \tag{A13}$$

The lateral system displacement is found to be linearly related to the load F_1 (Figure A6). The average lateral compliance $C_L(\sigma_3, A^s)$ is described with

$$u_3^{sys} = C_L(\sigma_3, A^s)F_1 \tag{A14}$$

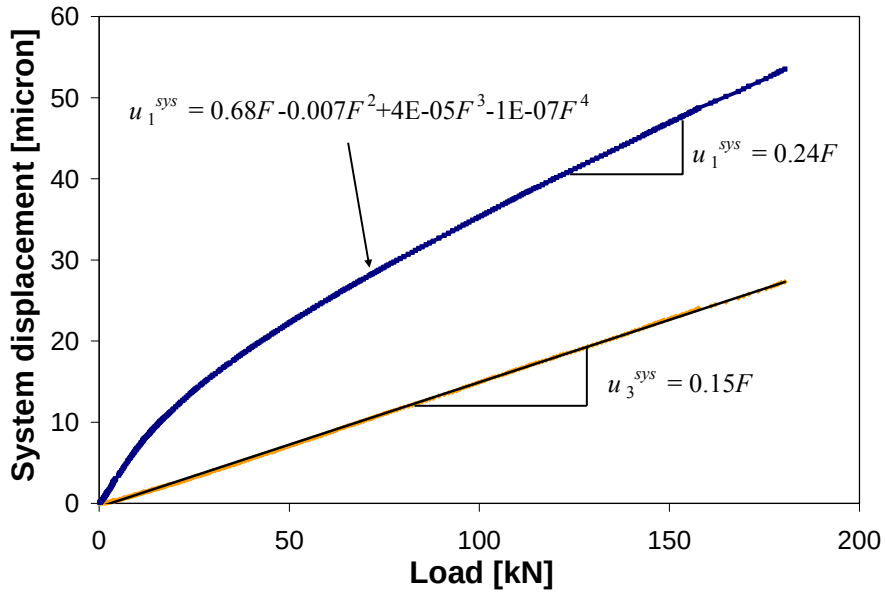

Figure A6: Calibration of axial and lateral displacement response.

C_A and C_L are calculated to be in the range of 0.23-0.73 micron/kN and 0.14-0.38 micron/kN respectively; they are found to be decreasing with increasing confining pressure. Also, they are not dependent on the tested material, but increase with increasing specimen size (Figure A7).

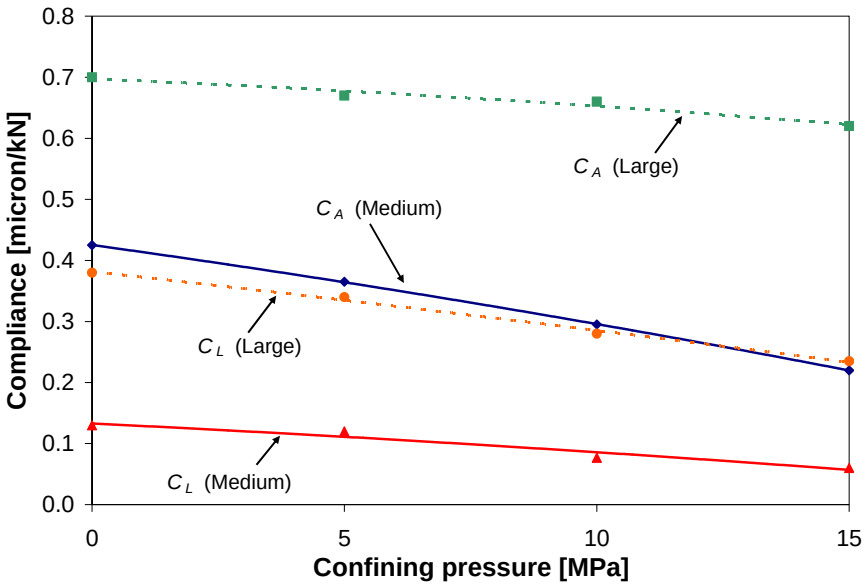

Figure A7: Axial and lateral compliances as functions of confinement for medium and large PMMA specimens.

Indiana limestone properties

To demonstrate the utility of the apparatus, Indiana limestone, a sedimentary rock with grain size less than 1 mm, was selected for plane strain and conventional triaxial compression/extension testing. A single block, 225 x 215 x 200 mm (*x, y, z*-axes), with density ρ = 2300 kg/m^3 and porosity ϕ = 13%, was used to fabricate all specimens. Ultrasonic velocity measurements show that the rock has a low level of anisotropy (less than 3%). P-wave and S-wave velocities (c_p [km/s], c_s [km/s]) in *x*, *y*, and *z*-directions were measured to be (4.23, 2.53), (4.39, 2.54), and (4.29, 2.51). Thus, the rock is assumed to be elastically isotropic.

Uniaxial compression tests were performed on four right circular cylinders (cores), and conventional triaxial compression/extension tests were performed on ten cores; all specimens were prepared in accordance with ISRM standards (Brown 1981) and loaded at an axial displacement rate of 5 x 10^{-4} mm/s. For the uniaxial tests, axial and tangential strains were monitored by foil strain gages to determine Young's modulus *E* and Poisson's ratio *v* within the linear response of the rock, typically from 10-50% of the uniaxial compression strength (UCS). The cylindrical specimens were 31.5 mm in diameter, which is smaller than the suggested diameter size of 54 mm, but the diameter to

grain size ratio is still larger than the recommended value of 10:1. The height of the cylindrical specimens ranged from 82 – 90 mm, within the desired height to diameter ratio of 2 – 3. The ends of the specimens were lubricated with stearic acid (Labuz and Bridell 1993). The results of the uniaxial tests yielded the following range of the parameters: UCS = 42 – 44 MPa, E = 26 – 29 GPa, and ν = 0.19 – 0.21.

Three plane strain compression experiments, BXIL-1, BXIL-2, and BXIL-3 were conducted at 0, 5, and 10 MPa cell pressures respectively. Three small prismatic specimens (100 x 75 x 28 mm) were cut from the block in the same way as the core specimens, *i.e.* bedding aligned normal to the axial stress. For each specimen, all of the faces were ground so that opposite sides were parallel and adjacent sides were perpendicular within ±0.01 mm in 100 mm. The specimen was assembled with the upper and lower steel platens contacting the 100 x 28 mm faces and two steel plates, 3 mm thick, contacting the 28 x 75 mm faces. The four surfaces in contact with polished-steel platens were covered with stearic acid to reduce friction at the platen-specimen interfaces and promote homogeneous deformation (Labuz and Bridell 1993). The specimen and platens were held together in a custom jig and two specimen sides exposed to the cell pressure were sealed by a polyurethane coating (Figure A5).

The specimen with attached platens was wedged in the frame so that the stress in the plane strain direction (z-axis) was at least 10% greater than the cell pressure σ_3. The entire biaxial frame was placed inside the pressure cell and exposed to fluid pressure during an experiment. The cell was filled with hydraulic oil and the pressure was applied with a microprocessor-based hydraulic pump that maintained cell pressure at a constant value, within a tolerance of 0.1 MPa. Closed-loop, servo-controlled tests were performed within a 1000 kN load frame (MTS Systems, Eden Prairie, MN) with an average lateral displacement rate of 5 x 10^{-5} mm/s as a feedback signal. A cell pressure-compensated load cell, with a sensitivity of 5 kN/mV/vdc, was placed below the specimen, between the lower loading platen and the base unit, and provides an accurate measurement of axial load. *PPS* was calculated to be 84.7% (σ_3 = 0 *MPa*), 87.5% (σ_3 = 5 *MPa*), and 90.2% (σ_3 = 10 *MPa*); recall that *PPS* increases with increasing cell pressure for the specimens of the same size and elastic parameters. Only the test conducted at 10 *MPa* (BXIL-3)

satisfied $PPS > 90\%$, and its results are analyzed in terms of elastic and inelastic material response.

Elastic response

Generalized Hooke's law for the incremental behavior of an isotropic linearly elastic solid in plane strain takes the following form for principal strains and stresses ($\varepsilon_2 = 0$):

$$\Delta\varepsilon_1 = \frac{1+\nu}{E}\left[(1-\nu)\Delta\sigma_1 - \nu\Delta\sigma_3\right]$$

$$\Delta\varepsilon_3 = \frac{1+\nu}{E}\left[(1-\nu)\Delta\sigma_3 - \nu\Delta\sigma_1\right] \tag{A15}$$

$$\Delta\sigma_2 = \nu\left(\Delta\sigma_1 + \Delta\sigma_3\right)$$

Noting that cell pressure is constant throughout the test ($\Delta\sigma_3 = 0$) and taking the sign convention of compression positive, Young's modulus E and Poisson's ratio ν are

$$E = \Delta\sigma_1 \frac{\Delta\varepsilon_1 - 2\Delta\varepsilon_3}{\left(\Delta\varepsilon_1 - \Delta\varepsilon_3\right)^2} \tag{A16}$$

$$\nu = \frac{-\Delta\varepsilon_3}{\Delta\varepsilon_1 - \Delta\varepsilon_3} \tag{A17}$$

Using the system corrections for axial and lateral displacements, the increments of principal strains $\Delta\varepsilon_1$ and $\Delta\varepsilon_3$, as well as the increment of axial stress $\Delta\sigma_1$, were calculated in the range of linear response (10-50% peak axial load), providing the values of Young's modulus $E = 28.0$ GPa and Poisson's ratio $\nu = 0.21$, which are close to those measured in the uniaxial compression tests.

Inelastic response

Permanent volume change, both compaction and dilation, has been noted for a wide variety of rock when stressed beyond an elastic limit (Brace *et al.* 1966). To observe inelastic response, elastic compaction and distortion must be removed from the total deformation.

For plane (biaxial) deformation, volume strain ε and shear strain γ are written as

$$\varepsilon = \varepsilon_1 + \varepsilon_3 \tag{A18}$$

$$\gamma = \varepsilon_1 - \varepsilon_3 \tag{A19}$$

Total volume strain and the axial stress difference for BXIL-3 test are plotted as a function of axial strain (Figure A8), and show typical behavior of a dilatant rock. Using compression positive sign convention, the volume strain increased due to compaction of the specimen, and then decreased as the rock dilates. The onset of the nonlinear volume strain response was used as a benchmark signifying when inelastic (plastic) deformation initiated.

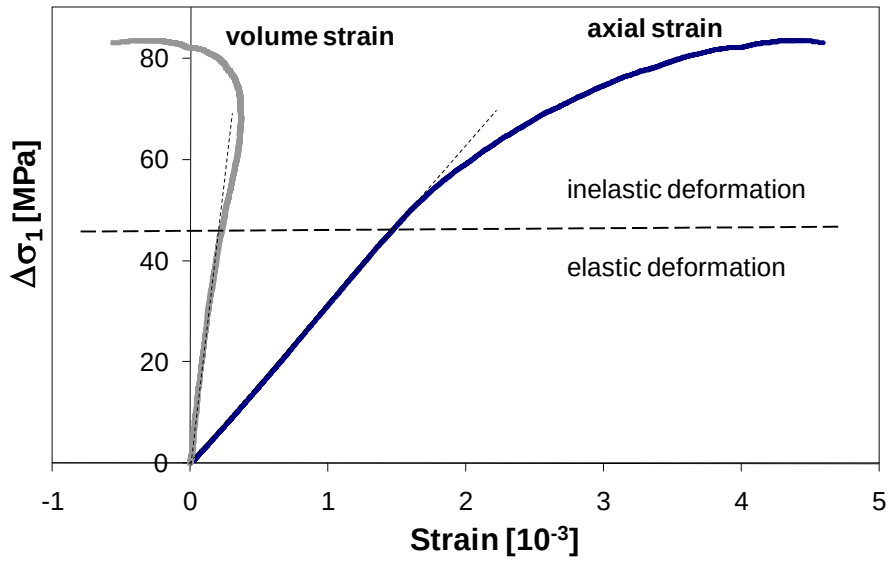

Figure A8: Axial and volume strain response for plane strain compression test.

The plastic strains were determined by removing the calculated elastic response from the measured deformation assuming no change in elastic parameters:

$$d\varepsilon^p = d\varepsilon^{meas} - d\varepsilon^e \tag{A20}$$

$$d\gamma^p = d\gamma^{meas} - d\gamma^e \tag{A21}$$

For the test conducted at 10 MPa cell pressure, plastic deformation was associated with a small amount of plastic compaction followed by a dilatant response (Figure A9). The increase of plastic volume strain was fairly linear near peak axial load, with the plastic shear strain at peak $\gamma^p = 4.5 \times 10^{-3}$. The dilatancy angle ψ (Hansen 1958) is defined by

$$\sin\psi = -\frac{d\varepsilon^p}{d\gamma^p} \tag{A22}$$

As displayed in Figure A9, the compactive behavior of Indiana limestone at the onset of plastic deformation is observed as a negative dilatancy angle, and plastic compaction is followed by a dilatant response shown as a positive dilatancy angle, which increases with plastic shear strain to 11° at peak axial load.

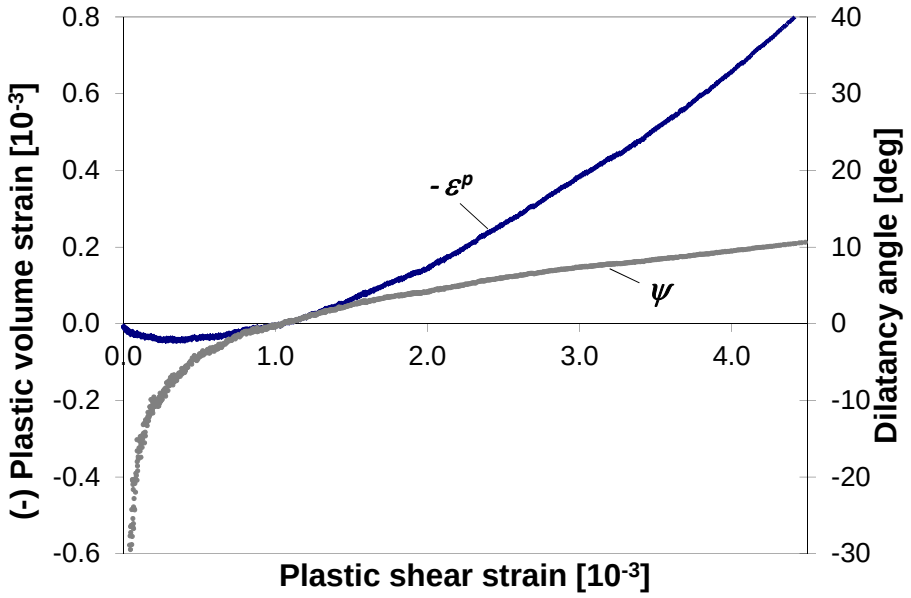

Figure A9: Dilatancy behavior for BXIL-3 test: $-\varepsilon^p$ and ψ vs γ^p.

Strength

The results of three plane strain compression experiments can be compared with the results of the conventional triaxial tests in terms of principal stresses at failure. A linear strength relation that includes the intermediate stress is the Paul-Mohr-Coulomb (PMC) failure criterion (Paul 1967):

$$A\sigma_1 + B\sigma_2 + C\sigma_3 = 1 \tag{A23}$$

where

$$A = (1 - \sin\phi_c)/(2V_o\sin\phi_c),$$
$$B = (\sin\phi_c - \sin\phi_e)/(2V_o\sin\phi_c), \tag{A24}$$
$$C = -(1 + \sin\phi_e)/(2V_o\sin\phi_e).$$

Three material parameters, friction angles in compression ϕ_c and extension ϕ_e, and the uniform triaxial tensile strength V_o, can be identified from conventional triaxial compression and extension experiments and are sufficient to define a six-sided failure surface (Meyer and Labuz 2013).

Of the ten triaxial tests, six were performed in compression with $\sigma_1 = \sigma_{axial}$ and $\sigma_2 = \sigma_3 = \sigma_{radial}$, and four in extension with $\sigma_1 = \sigma_2 = \sigma_{radial}$ and $\sigma_3 = \sigma_{axial}$. The compression tests were conducted as loading tests, where σ_{axial} is increased ($\Delta\sigma_{axial} > 0$) from $\sigma_{axial} = \sigma_{radial}$ until failure and σ_{radial} = constant. The remaining four triaxial specimens were tested in extension unloading, with σ_{axial} decreasing ($\Delta\sigma_{axial} < 0$) from $\sigma_{axial} = \sigma_{radial}$ until failure and σ_{radial} = constant. The results from the compression and extension experiments, as well as the results of plane strain compression tests, are presented in Table A1.

For the axisymmetric stress state in conventional triaxial testing, the stress invariants P and q are:

$$P = \frac{\sigma_1 + \sigma_2 + \sigma_3}{3} = \frac{\sigma_{axial} + 2\sigma_{radial}}{3} \tag{A25}$$

$$q = \sqrt{3J_2} = \sigma_{axial} - \sigma_{radial} \tag{A26}$$

where J_2 is the second invariant of the stress deviator $S_{ij} = \sigma_{ij} - P\delta_{ij}$ and δ_{ij} = Kronecker delta. The PMC failure criterion in compression can be written as

$$q = \frac{6\sin\phi_c}{3 - \sin\phi_c} P + \frac{6c_c \cos\phi_c}{3 - \sin\phi_c} \tag{A27}$$

The extension line can be given in a similar manner:

$$q = -\frac{6\sin\phi_e}{3 - \sin\phi_e} P - \frac{6c_e \cos\phi_e}{3 - \sin\phi_e} \tag{A28}$$

where c_c and c_e are the cohesion in compression and extension respectively (Meyer and Labuz 2013).

Table A1: Principal stresses at failure for plane strain compression and triaxial compression and extension experiments.

Test name	σ_1 [*MPa*]	σ_2 [*MPa*]	σ_3 [*MPa*]
BXIL-1	45.4	8.4	0.0
BXIL-2	61.2	16.8	5.0
BXIL-3	101.0	26.4	10.0
Triax-comp-1	69.7	5.0	5.0
Triax-comp-2	82.2	10.0	10.0
Triax-comp-3	103.1	15.0	15.0
Triax-comp-4	100.8	20.0	20.0
Triax-comp-5	114.8	25.0	25.0
Triax-comp-6	133.2	30.0	30.0
Triax-ext-1	50.0	50.0	0.7
Triax-ext-2	58.0	58.0	2.6
Triax-ext-3	60.0	60.0	1.7
Triax-ext-4	62.0	62.0	2.1

The compression and extension data were fitted with lines that intersect the *p*-axis at the same point V_o, which is required for any failure surface. The corresponding lines of best fit with a common vertex were determined by finding the maximum value of the sum of the correlation coefficients ($R_c^2 + R_e^2$), under the condition that the absolute value of the difference $\left| R_c^2 - R_e^2 \right|$ is a minimum (Meyer and Labuz 2013). The data and the best fit lines with the constraint of the same V_o are shown in Figure A10a ($R_c^2 = R_e^2 = 0.926$).

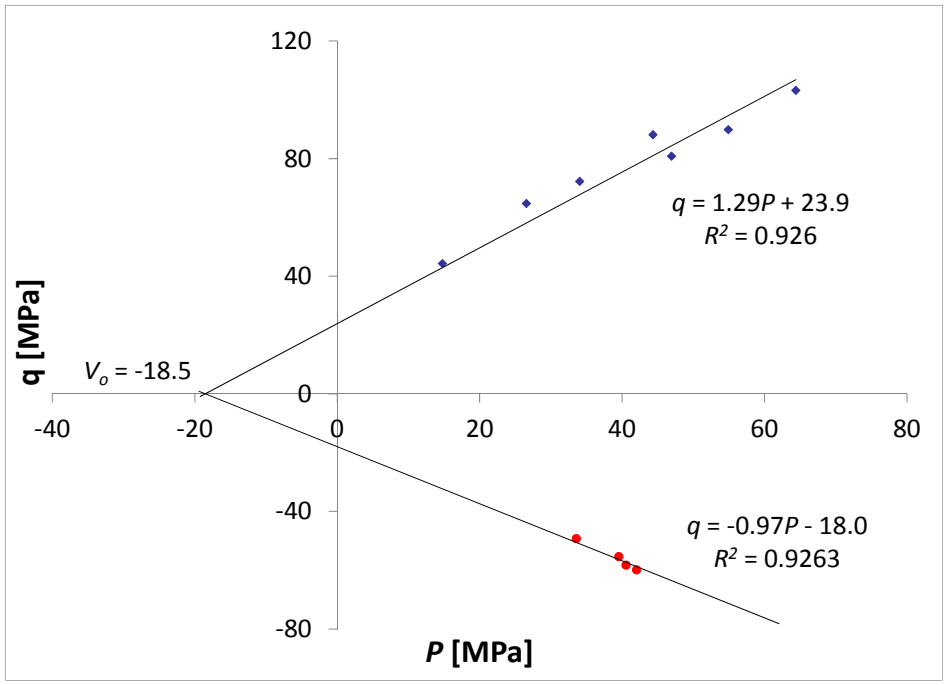

(a)

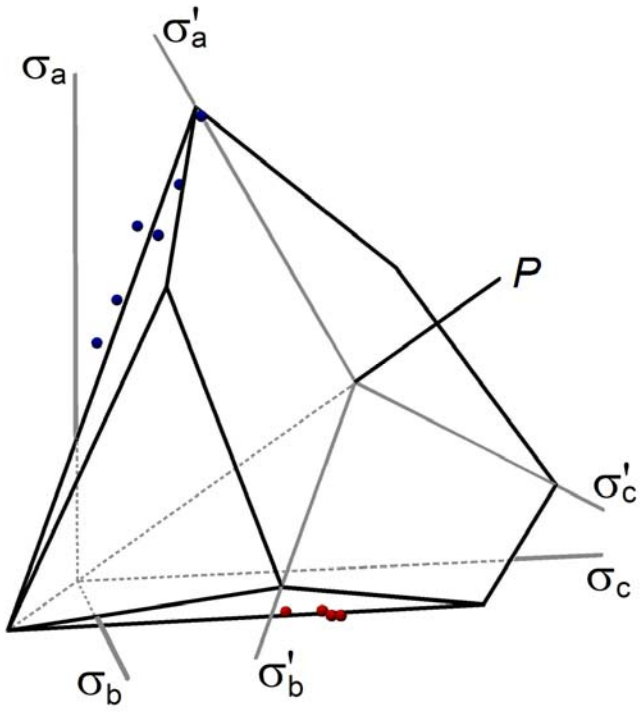

(b)

Figure A10: Results of triaxial compression (blue dots) and extension (red dots) tests (a) in the P - q plane and (b) in the principal stress space.

Using equations (A27) and (A28), a difference in friction angles in compression and extension is observed: $\phi_c = 32.1°$ and $\phi_e = 35.4°$, which is a sufficient but not necessary condition for a material exhibiting an intermediate stress effect. For isotropic rock, knowledge of the two internal friction angles ϕ_c and ϕ_e, and one strength parameter such as the vertex V_o, is sufficient to define a six-sided failure surface in the principal stress space σ_a, σ_b, σ_c, with no order implied (Figure A9b); the data from the conventional triaxial tests are shown. The hexagonal pyramid results for the six combinations of the ordering of the principal stresses.

The data from the plane strain experiments can be presented in principal stress space (Figure A10a) and on a plane perpendicular to the P-axis ($\sigma_a = \sigma_b = \sigma_c$) called the π-plane and described by $P = constant$; the intersection of the failure surface and the π-plane is a hexagon that displays a three-fold symmetry (Figure A10b). Note that for conventional triaxial tests $\sigma_a' = q$, where σ_a', σ_b', and σ_c' are the projections of σ_a, σ_b, and σ_c on the π-plane. The results of the three plane strain compression tests (BXIL-1, BXIL-2, and BXIL-3) and the π-planes at failure are presented in Figures A10a and A10b. The specimen tested at $\sigma_3 = 10$ MPa failed at a higher major principal stress σ_1 than predicted by the PMC criterion, but the data points for the specimens at 0 and 5 MPa cell pressure (BXIL-1 and BXIL-2) are consistent with the six-sided failure surface obtained from the conventional triaxial tests.

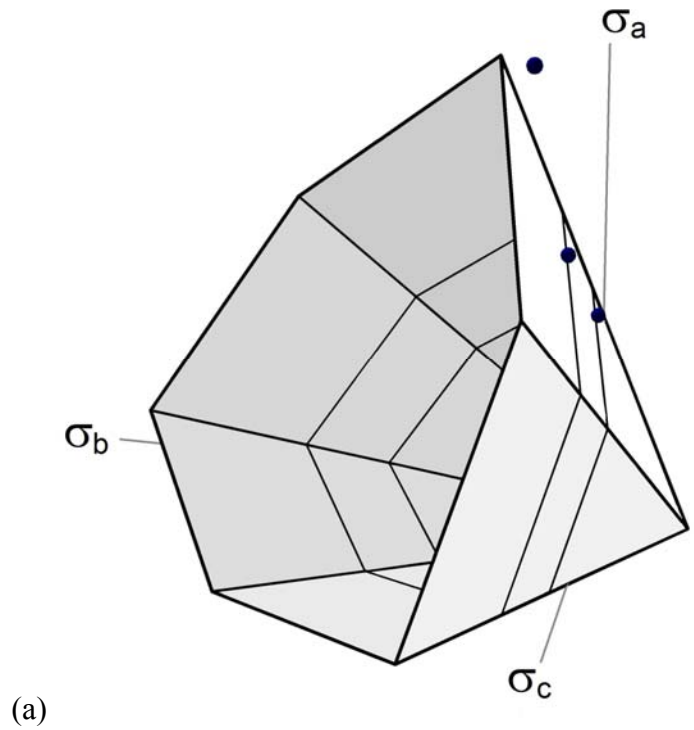

(a)

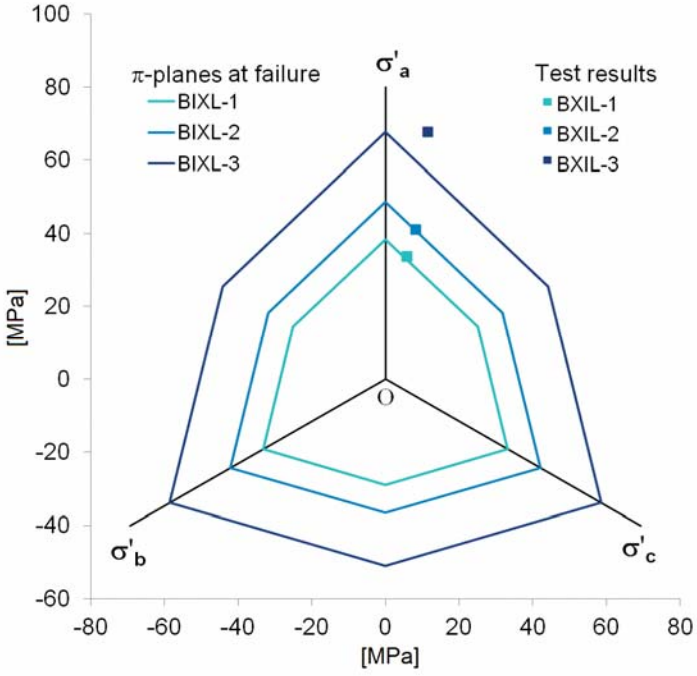

(b)

Figure A11: Plane strain test (BXIL-1, BXIL-2, and BXIL-3) results with (a) the failure surface and (b) corresponding π-planes.

Conclusions

Passive restraint provides a simple method to achieve plane strain and to generate an intermediate principal stress different from the major and minor principal stresses. In addition, the in-plane strains can be accurately measured, allowing for the evaluation of elastic and inelastic parameters of a rock.

To demonstrate the utility of passive restraint, Indiana limestone was tested using standard axisymmetric loading and plane strain compression. The material parameters, both deformation- and stress-based, compared well. Young's modulus E and Poisson's ratio ν measured in plane strain were in the range of those obtained from uniaxial compression. From the plane strain test, plastic volume and shear strains showed that, for the specimen tested at σ_3 = 10 MPa, the compactive behavior of rock at the onset of plastic deformation was followed by a dilatant response, with the dilatancy angle increasing with plastic shear strain and being equal to 11° at failure, much less than the compression friction angle of 32°. Comparison of the principal stresses at failure with the Paul-Mohr-Coulomb failure surface confirmed the effect of the intermediate principal stress on strength. The friction angle measured in conventional triaxial extension tests was larger than the one measured from compression tests, a sufficient but not necessary condition of the intermediate stress effect, and the strength data from the plane strain tests were consistent.

B. AE and failure planes

Acoustic emission locations were determined for specimens tested in plane strain compression under dry, quasi-unjacketed, drained, and undrained conditions. For accurate determination of AE locations, P-wave velocity was measured at different effective stresses. For the tests described, c_p=2.4 km/s for a dry specimen at atmospheric pressure and c_p at 5 MPa confining pressure is 3.0 km/s (Figure B1), while c_p=3.3 km/s at 10 MPa mean stress and 5 MPa pore pressure for water-saturated specimen (Figure 4.12). Time of first arrival information is extracted from the P-waves using an algorithm described in Ince *et al.* (2009).

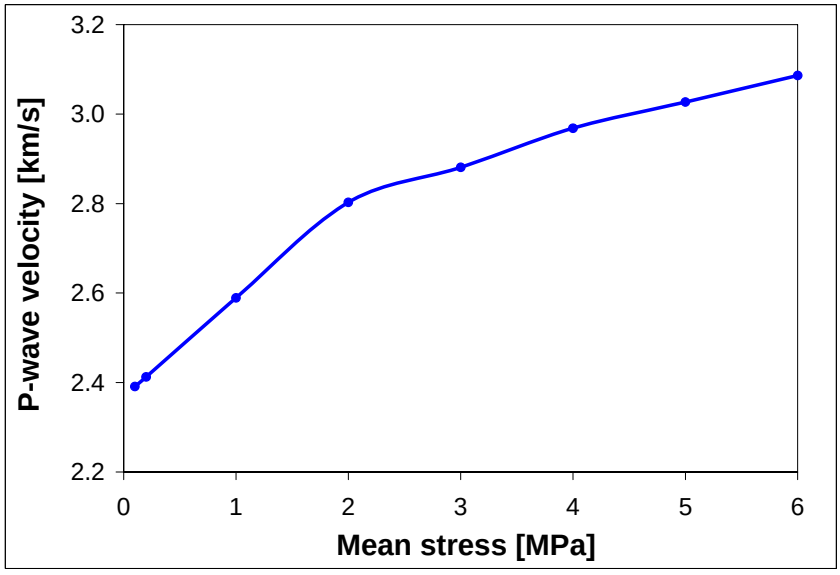

Figure B1: Change of the P-wave velocity with mean stress in dry sandstone specimen.

Dry test

Processing of the AE data recorded for the dry test provided 1834 locations with error less than 3 mm, out of 9254 total events. Before the peak load was reached, AE events were scattered in the specimen (Figure B2a). However, in the post-peak region, located events closely follow the failure mechanism (Figures B2b and B2c), which in this test was an inclined fracture (Figure B2d).

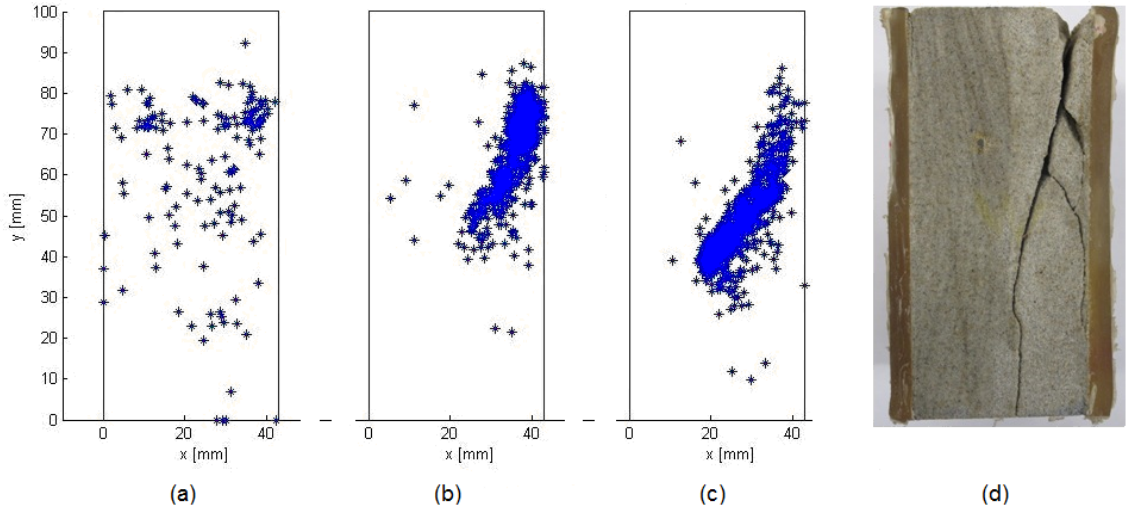

Figure B2: Dry test. Projection of AE events location (a) pre-peak, (b) peak - 90% post-peak, (c) 90% post-peak - residual; (d) photo of failed specimen.

"Unjacketed" test

The quasi-unjacketed test is characterized by the equal increments of confining and pore pressure. This condition is achieved by not totally covering the side faces of the specimen with polyurethane, such that confining fluid (hydraulic oil) can penetrate the specimen. Constant cell (confining) pressure during the test assures complete rock saturation.

Locations of AE for the quasi-unjacketed test (Figure B3a) also follow the failure mechanism (Figure B3b). The effective confinement for an unjacketed test is zero, so it is natural that the observed failure type is close to axial splitting.

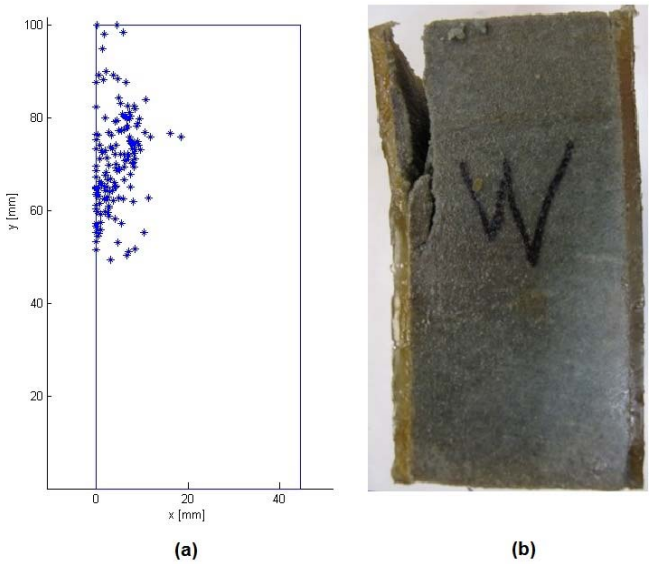

Figure B3: "Unjacketed" test. (a) Projection of AE events location, (b) photo of failed specimen.

Drained test

Lateral deformation of the specimen tested under the drained condition was controlled throughout the post-peak region. Two failure planes eventually developed (Figure B4).

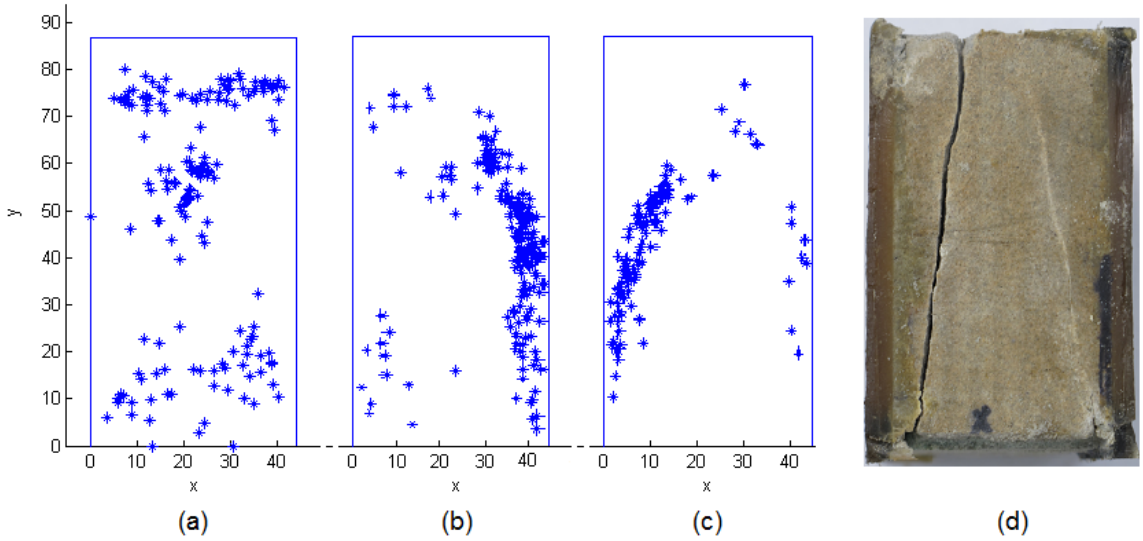

Figure B4: Drained test. Projection of AE events location (a) pre-peak, (b) formation of the first failure plane, (c) formation of the second failure plane; (d) photo of failed specimen.

Linear bearing (SLED) movement was monitored during the test. It can be seen in Figure B5, that when the peak load was reached the linear bearing started displacing in one direction, but at some point started moving in the opposite direction. Corresponding AE data (Figure B4) shows this change of the direction in SLED movement can be related to the formation of the second failure plane in the specimen.

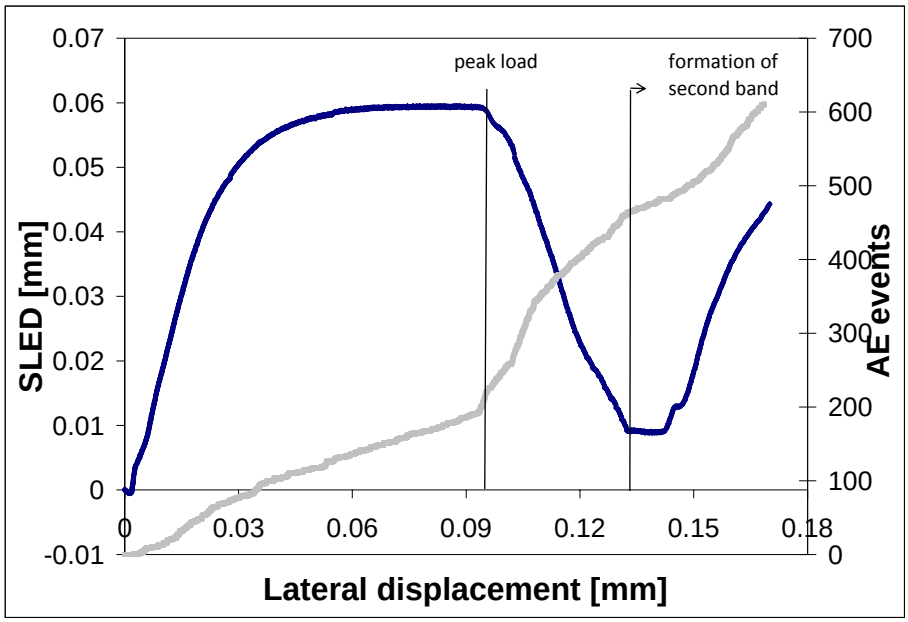

Figure B5: SLED displacement and AE events in drained plane strain compression test.

Undrained test

Similar to the drained test, two failure planes developed in the specimen tested under undrained conditions. Figures B6 and B7 show how the failure was localized in the rock with increasing load. Because of dilatant hardening (see section 4.5), it took much longer to reach the peak load for the undrained specimen compared to the drained one of the same size and tested with the same strain rate.

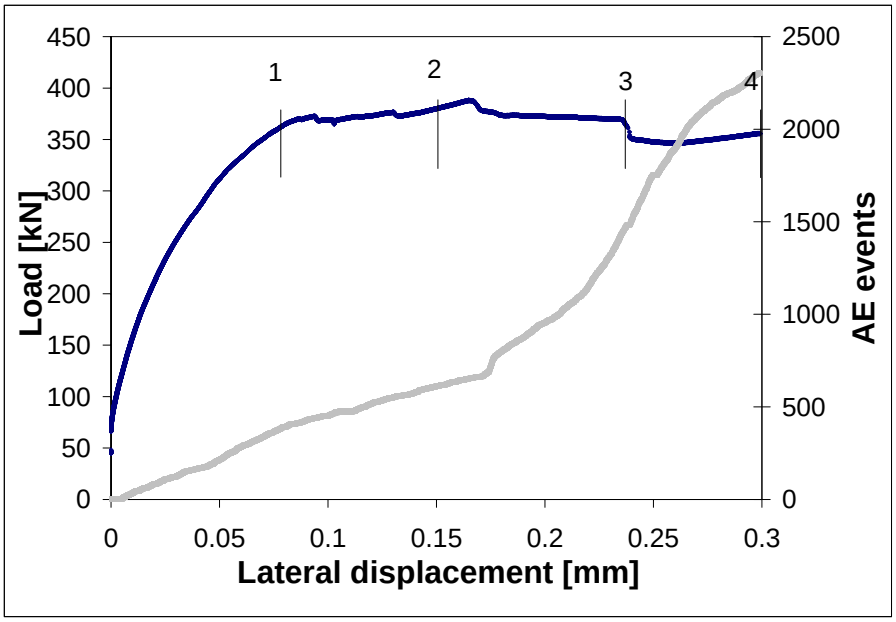

Figure B6: Load-displacement diagram and AE events in undrained plane strain compression experiment.

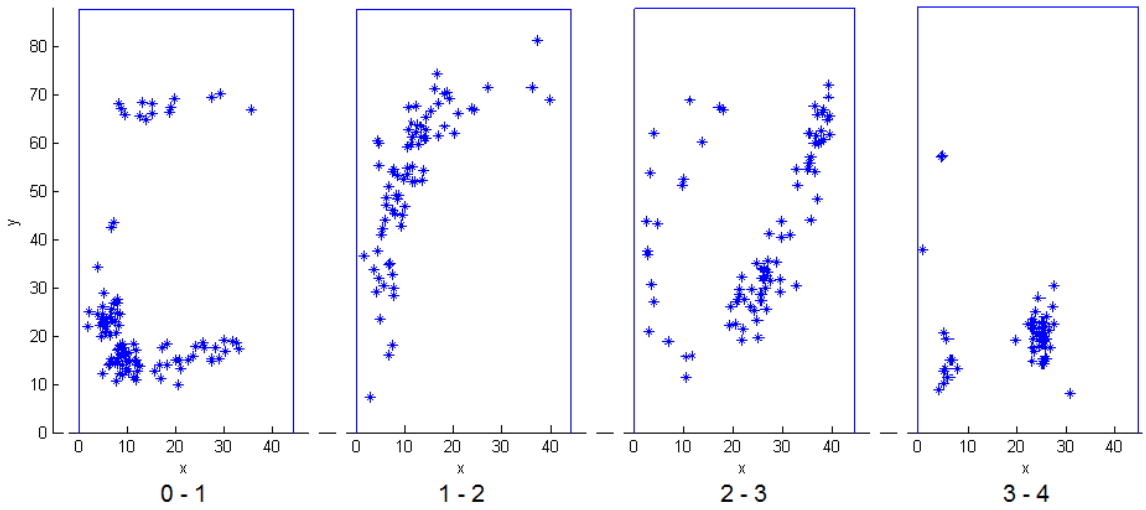

Figure B7: Undrained test. Projection of AE events location at different stages of loading designated in Figure B6.

Moreover, it can be clearly seen on a 3D-plot (Figure B8a) that two failure planes eventually developed in the rock, which was also confirmed by the visual inspection of the specimen after the test (Figure B8b).

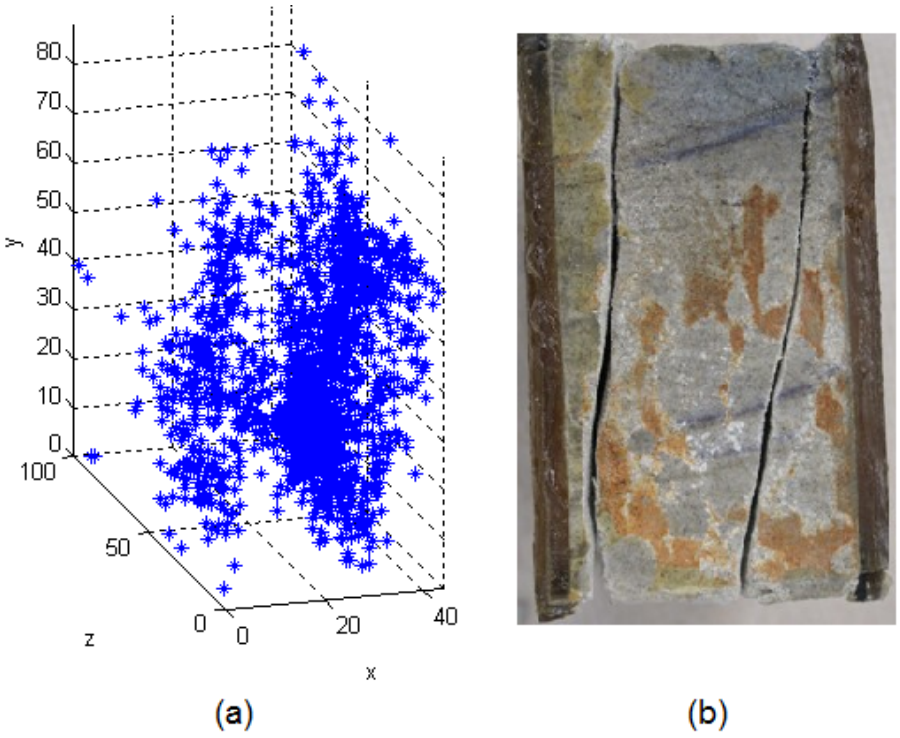

Figure B8: Undrained test: (a) 3D location of AE events; (b) photo of failed specimen.

Summarizing the experimental results, it can be stated that locations of acoustic emission (AE) events can be precisely determined before and after failure in dry and fluid-saturated rock specimens, which allows the monitoring of the localization of failure in rock specimens.